PROCESSING, STRUCTURE, AND PROPERTIES OF POLYACRYLONITRILE-NANOCELLULOSE COMPOSITE FILMS AND FIBERS

A Dissertation
Presented to
The Academic Faculty

by

Jeffrey Luo

In Partial Fulfillment
of the Requirements for the Degree
Doctor of Philosophy in the
School of Materials Science and Engineering

Georgia Institute of Technology
August 2018

PROCESSING, STRUCTURE, AND PROPERTIES OF POLYACRYLONITRILE FILMS AND FIBERS WITH HIGH NANOCELLULOSE LOADING

Approved By:

Dr. Satish Kumar, Advisor
School of Materials Science and Engineering
Georgia Institute of Technology

Dr. Kyriaki Kalaitzidou
The George W. Woodruff School of Mechanical Engineering
Georgia Institute of Technology

Dr. Robert J. Moon, Advisor
Forest Product Laboratory
USDA-Forest Service
School of Materials Science and Engineering
Georgia Institute of Technology

Dr. Meisha Shofner
School of Materials Science and Engineering
Georgia Institute of Technology

Dr. Yulin Deng
School of Chemical and Biomolecular Engineering
Georgia Institute of Technology

Date Approved: July 2, 2018

ACKNOWLEDGEMENTS

I would like to thank my advisors, Dr. Satish Kumar and Dr. Robert J. Moon for their guidance throughout my study. Without their guidance, knowledge, and suggestions the completion of this thesis would not be possible. I would also like to thank Dr. Yulin Deng, Dr. Kyriaki Kalaitzidou, and Dr. Meisha Shofner for taking their time to serve on my thesis committee and for their advice on research

I am thankful to Dr. Prabhakar Gulgunje, Dr. Kishor Gupta, Dr. Bradley Newcomb, Dr. Clive Liu, Dr. Amir Bakhtiary Davijani, Dr. Po-Hsiang Wang, and Dr. Huibin Chang for teaching me, their research methods, and also for their help with various experiments. I am grateful to Nikolay Semenikhin for helping me with functionalization studies. Pedro Jose Arias Monje and Mingxuan Lu are acknowledged for help with fiber spinning and characterization. I also acknowledge the help of the rest of the current group members for their help with various experiments and discussions.

Finally, I would like to thank my parents and brothers for their support and encouragement. I am also grateful to all my friends who were there throughout my studies.

TABLE OF CONTENTS

LIST OF TABLES

LIST OF FIGURES

LIST OF PUBLICATIONS BASED OFF THIS WORK

J. Luo, H. Chang, A.A. Bakhtiary Davijani, H.C. Liu, P.-H. Wang, R.J. Moon and S. Kumar, Influence of high loading of cellulose nanocrystals in polyacrylonitrile composite films. Cellulose, 2017. 24(4): p. 1745-1758. (Based off of Chapter 2)

J. Luo, N. Semenikhin, H. Chang, R.J. Moon, and S. Kumar, Post-sulfonation of cellulose nanofibrils with a one-step reaction to improve dispersibility. Carbohydrate Polymers. 2018. 18: p. 247-255. (Based off of Chapter 3)

J. Luo, H. Chang, P.-H. Wang, R.J. Moon and S. Kumar, Cellulose Nanocrystals Effect on the Stabilization of Polyacrylonitrile Composite Films. Carbon. 2018. 134: p. 92-102. (Based off of Chapter 4)

Summary

Cellulose is the most abundant biopolymer on earth with an estimated production of 1.5 x 10^{12} tons per year. With the high production, cellulose could be utilized to increase our sustainability and reduce our dependence on synthetic polymers made from oil. Recently nanocellulose in the form of cellulose nanocrystals (CNCs) and cellulose nanofibrils (CNFs) as potential fillers have been gaining significant interest. This is due to nanocellulose's high mechanical properties, high surface area, biodegradability, biorenewability, and low toxicity.

Polyacrylonitrile (PAN) is a synthetic polymer and has uses in clothing, home furnishings, and filtration membranes. PAN is also the predominant precursor for carbon materials such as carbon fiber.

In chapter 2, the effect of CNC loading on the mechanical, thermal, optical, and structural properties of PAN-CNC films was studied. Films were made successfully with up to 40 wt% CNC loading. These composite films demonstrated the same optical transparency, and an increase in mechanical properties when compared to neat PAN. The effect of CNC loading on rheology was also looked at, and it was found that the addition of CNCs increases the viscosity at low shear rates. It was also found that the viscosity of the PAN-CNC suspensions increased with time.

In chapter 3, the stabilization kinetics of the PAN-CNC films, and structural changes of the films were investigated. It was found that the addition of CNCs reduced the cyclization activation energy. It was also found that the reaction rate of cyclization and oxidation could increase with the addition of CNCs. The thermal stability of CNCs was

determined to be higher in the composite films than in neat form, which was examined by wide angle x-ray diffraction and Fourier transform infrared spectroscopy.

In chapter 4, a method to make sulfonated CNFs that has the same surface chemistry as CNCs made by sulfuric acid hydrolysis is developed. This sulfonation of CNFs improves the dispersibility of CNFs in solvent. The method developed in this study can produce sulfonated CNFs faster the other reported sulfonation method. This technique is also faster than the most common CNF functionalization, TEMPO oxidation. The chemical stability of TEMPO CNFs and sulfonated CNFs in water and dimethylformamide was also investigated.

In chapter 5, the characterization of PAN-CNF fibers and the effect of processing on the resulting mechanical properties was studied. Two different methods of functionalization were performed on the CNFs, TEMPO oxidation and amination, and the reinforcement effect of the different functionalizations were studied. The aminated CNFs provided more mechanical reinforcement than the TEMPO CNFs. This is attributed to the difference between surface chemistry, and the better interaction between the amine groups on the aminated CNFs and PAN than the carboxylic acid groups on the TEMPO CNFs.

In chapter 6, we provide the conclusions of this thesis work. Recommendations for future studies based off this thesis is also reported.

CHAPTER 1. INTRODUCTION

1.1 Materials

1.1.1 Polyacrylonitrile

Acrylonitrile was first synthesized in the 1893 by Charles Moureu and polyacrylonitrile was first polymerized by Charles Moureu a year later [1-3]. The chemical structure of polyacrylonitrile (PAN) can be seen in **Figure 1.1** [4]. After the discovery of PAN, it was not widely used, because it was difficult to process. The reason it was difficult to process was because the polymer degrades before it melts, and because there was no known solvent for PAN at the time [3]. PAN was first spun into a fiber in 1938 by Herbert Rein of I.G. Farbenindstrie using aqueous solutions of ammonium thiocyanate or zinc chloride to dissolve the PAN [3, 5]. PAN started to pick up interest in the 1940s when more solvents for PAN were discovered such as dimethylformamide (DMF). With the use of this new solvent DuPont developed a process for spinning PAN into acrylic fibers in the 1940s, and this PAN fiber was commercialized by DuPont in 1950 as "Orlon" [1, 6, 7].

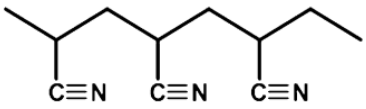

Figure 1.1. The chemical structure of PAN [4].

Polyacrylonitrile (PAN) has uses in the production of acrylic fibers (≥85% acrylonitrile monomers) for clothing, home furnishings, and filtration membranes [7, 8]. PAN is also the predominant precursor for industrially produced carbon fiber [4].

1.1.2 Cellulose

Cellulose is the world's most abundant biorenewable polymer with an annual estimated production of 1.5 x 10^{12} tonnes [9]. Currently there is large push for the world to become more environmentally friendly. This is due to the desire to reduce our dependence on fossil fuels and to lower our contribution to climate change. Due to the abundance of cellulose, and the recently developed techniques to process cellulose into nanofillers with high mechanical properties, high surface area, bio degradability, and low toxicity it can be an effective filler in polymer matrices and help reduce the amount of synthetic polymer used in various application.

Cellulose is a linear polymer with β 1-4 bonded glucose units (**Figure 1.2**), with a degree polymerization of up to 15,000 and as low as 300 depending on the source and whether it has undergone treatment [9-12]. Cellulose can be derived from a variety of sources, these being plants, tunicate, and bacteria [11, 13, 14].

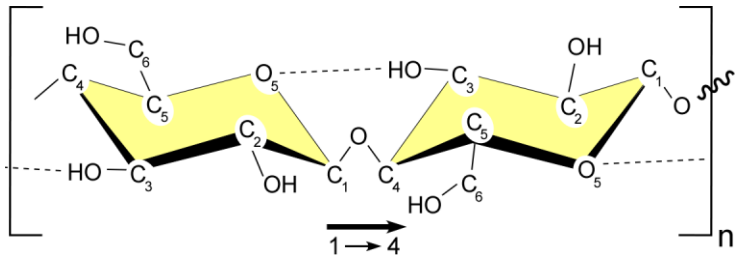

Figure 1.2. The chemical structure of a cellulose unit [11].

1.1.3 Cellulose Nanofibril

Cellulose can be mechanically broken down to cellulose nanofibrils (CNFs) which has diameter of around 4-200 nm and a length greater than 1 µm [15, 16]. A transmission

electron microscopy (TEM) image of CNFs can be seen in **Figure 1.3 (Left)**. CNFs have an elastic modulus of 80-100 GPa and a tensile strength of 1.6-3 GPa [11, 17-19].

Due to the structure of cellulose, the abundant amount of hydroxyl groups allows a significant amount of hydrogen bonding to occur between the cellulose. The high amount of surface area on the CNFs and the hydrogen bonding causes the CNFs to easily agglomerate, and once agglomerated separation is difficult [20-22].

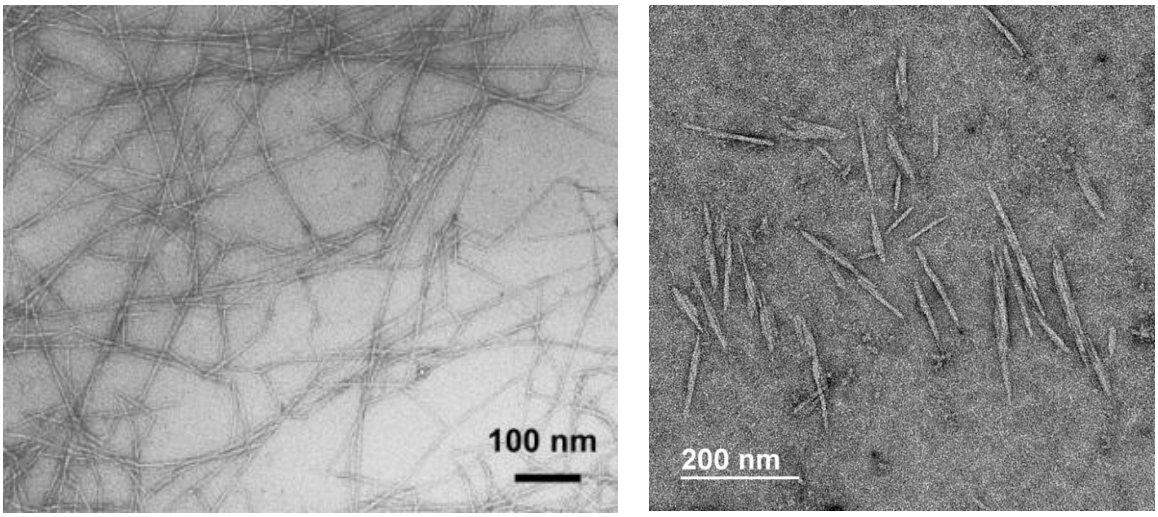

Figure 1.3. TEM image of CNF **(Left)** and CNC **(Right)**. [23]

Pure CNF film and fibers have been made, though the properties exhibited are lower than the properties of an individual CNF. CNF films have been made with an elastic modulus and tensile strength of 10-13.2 GPa and 110-214 MPa, respectively [24-26]. Drawing can be done to increase the mechanical properties of these films, and after drawing the elastic modulus increased from 10.3 GPa to 33.3 GPa (1.6 draw ratio) and the tensile strength increased from 185 MPa to 428 MPa (1.4 draw ratio) [26]. CNF fibers made with 2,2,6,6-tetramethyl-1-piperidinyloxy (TEMPO) CNFs through wet spinning have also been

made and these had an elastic modulus of 23 GPa and a tensile strength of 270-320 MPa [27, 28]. Drawing the TEMPO CNF fiber with a draw ratio of 1.28 increased the elastic modulus from 8.2 GPa to 33.7 GPa and increased the tensile strength from 118 MPa to 289 MPa [29]. While carboxymethylated CNF fibers made a flow focusing technique (similar technique to wet spinning) had mechanical properties with an elastic modulus of 52.8 GPa and a tensile strength of 830 MPa [30, 31]. With the flow focusing technique and with the addition of 10 wt% silk, CNF-silk fibers spun had a tensile strength of 978.8 MPa and an elastic modulus of 53.6 GPa[31]. Dry spun CNFs without any functionalization have also been produced which had with an elastic modulus of 12.6 GPa and a tensile strength of 222 MPa [32]. Currently spinning 100% CNF fibers has not been done with a technique that is industrially scalable. These fibers are typically spun into a coagulation bath with no take up winder, a strand of the CNF fiber is removed from the coagulation bath and dried with both end held down to keep the fiber straight and prevent shrinkage. The difficulty with continuous spinning of CNFs with take up is that a suspension of the cellulose is spun instead of a solution. The CNF suspension does not solidify when it enters a coagulation bath like a polymer solution. The CNF suspension remains a suspension until the liquid is removed by drying. If the CNF fiber is not dried before being taken up by the spool or quickly dried on the spool the filament will fuse together.

1.1.4 Cellulose Nanocrystal (CNC)

Cellulose nanocrystals (CNCs) can be made from cellulose by acid hydrolysis. The acid breaks down the amorphous regions in the cellulose, and what remains is highly crystalline CNC with a diameter of 3-20 nm and a length of 50-500 nm depending on the

source [11]. CNCs have an elastic modulus of 110-220 GPa and a tensile strength of 7.5-7.7 GPa [11, 17-19]. Pure CNC films have been made with an elastic modulus of 10-30 GPa and a tensile strength of 50-70 MPa, which is significantly lower than the theoretical properties of CNCs [33].

Due to the rod like shape of the CNCs, when suspensions of CNCs are sheared, they display a shear thinning behavior due to the alignment of the CNCs. Also due to rod like shape of the particle, it can form a percolation network at low volume concentration compared to fillers with a circular shape. The volume fraction needed to form a percolation network is 1% to 6% depending on the aspect ratio of the CNCs [34]. There was a study which showed that a CNC suspension at high concentrations (10 wt%) in water display an increase in viscosity over time at low shear rates, while the viscosity stayed constant with time at high shear rate [35]. This study showed that a CNC percolation network can form over time at low shear rate, but at high shear rates the shear forces prevents a CNC network from forming [35].

Due to the rigid rodlike shape of the CNCs and their surface chemistry they can form chiral nematic liquid crystals [36]. Such liquid crystals display unique optical properties under cross polarizers (**Figure 1.4**).

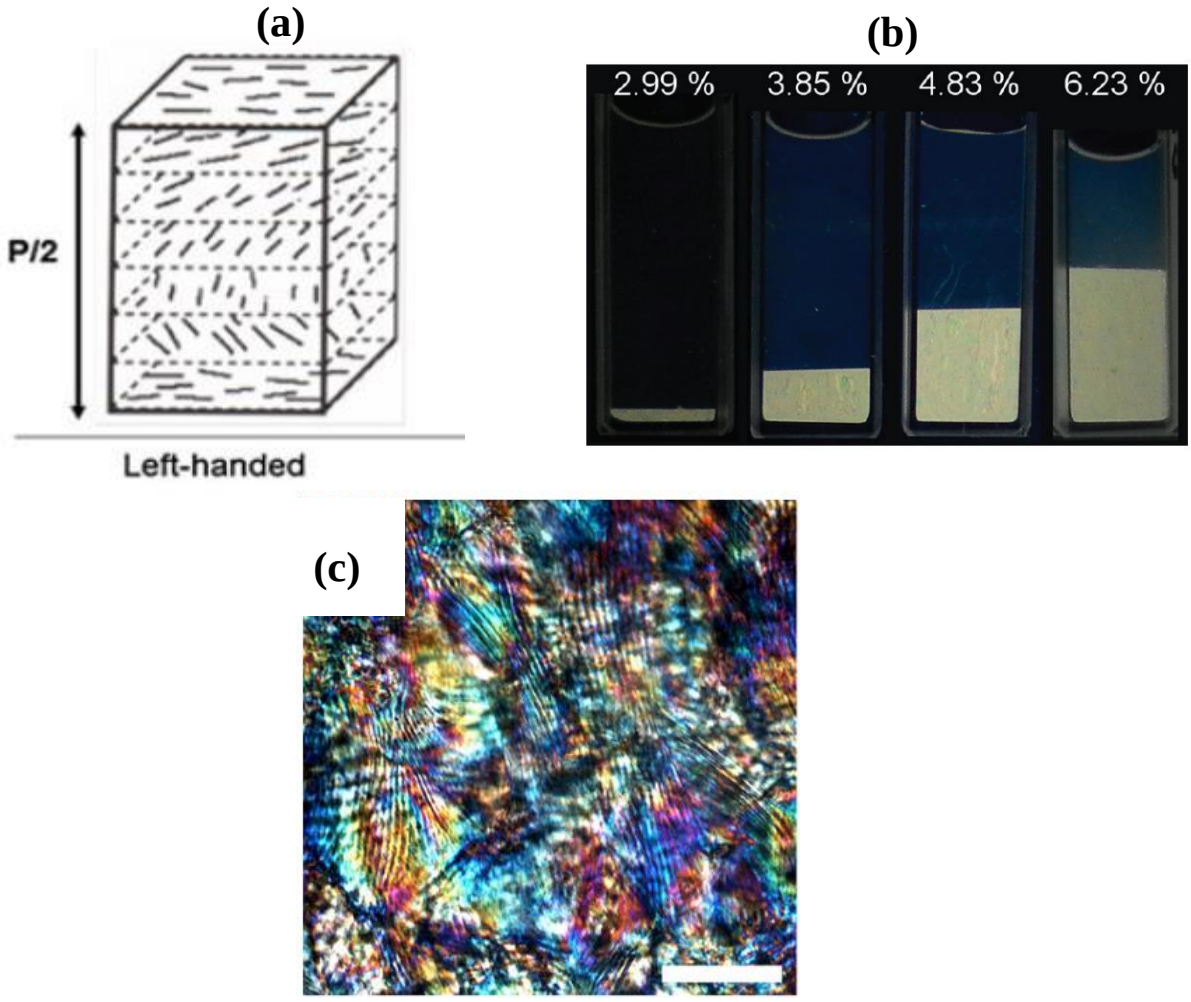

Figure 1.4. (a) Displaying a schematic of a chiral nematic formation. **(b)** CNC suspension seen through cross polarizers with varying amount of CNC displaying chiral nematic formation. **(c)** CNC film seen through a cross polarizer showing various colors (scale bar is 40 µm) [36, 37].

1.2 PAN Nanocomposites

Many different types of fillers have been added to PAN to try to improve the properties of PAN or to give PAN additional functionalities. Such fillers includes carbon nanotubes [38-40], cellulose nanocrystals [41], graphene oxide [42], iron oxide [43], FeCl [44], and hexagonal boron nitride (BN) [45]. It was found that the addition of single wall

nanotubes could increase the elastic modulus up to 300%, tensile strength up to 80%, storage modulus up to 200%, and increase the Tg by over 35 °C [38, 39]. The addition of CNCs could increase the elastic modulus up to 35%, tensile strength up to 17%, the storage modulus by 50%, and increase the Tg by 10 °C [41]. The addition of iron oxide was found that it could increase the tensile strength by 14% [43]. Different fillers can also give additional functionalities such as the addition of iron oxide also imparted superparamagnetic properties to the PAN fiber [43], the addition of graphene oxide allowed the fabrication of a composite with good desalination properties [42]. Incorporation of $FeCl_2$ into PAN allowed the composite to remove chromium from aqueous solutions [44], and the addition of MWNT increased the electrical conductivity of PAN fibers [40]. The addition of hexagonal BN has shown to increase the limiting oxygen index of PAN from 18% to 27% [45].

1.3 CNC-Polymer Nanocomposites Films

Many studies have already been done on CNC composite films with many different types of polymer matrices including polymethyl methacrylate (PMMA) [46], polyvinyl alcohol (PVA) [47-50], polylactic acid (PLA) [51, 52], polyvinylidene fluoride (PVDF) [53], polyvinyl chloride (PVC) [54], polypropylene (PP) [55], poly(3-hydroxybutyrate-co-3-hydroxyvalerate) (PHBV) [56-58], acrylonitrile butadiene styrene (ABS) [59], polyurethane [42, 60], epoxy [61, 62], starch [63], and chitosan [64]. The incorporation of CNCs into the polymer matrix can increase the elastic modulus, tensile strength, storage modulus, glass transition temperature (Tg), and thermal stability. In previous studies on films the incorporation of CNC increased the elastic modulus 23-50 % in PVA [47-49], 42

% in PLA[52], 115-250 % in PHBV [56, 57], 35 % in ABS [59], 69-144 % in polyurethane [42, 60], 64 % in epoxy [62], 34 % in starch [63], 87 % in chitosan [64], and an increase was also seen in PVC [54]. The tensile strength increased 25-32 % in PVA [47, 50], 61 % in PLA[52], 35 % in PVDF [53], 42 % in PP [55], 85-149 % in PHBV [56, 57], 16 % in ABS [59], 28 % in polyurethane [42], 50-77 % in epoxy [61, 62], 56 % in starch [63], and an increase in PVC [54] was also seen. The values of the elastic modulus and tensile strength of the neat polymer matrices and the CNC composites can be found in **Table 1.1**. Storage modulus increased 20 % in PLA [51], 20 % increase in PHBV [57], 49 % increase in epoxy [61], and increases were also seen in PVA [47], PP [55], and polyurethane [42]. The Tg increased 5 °C in PHBV [57], and 2 °C in polyurethane [42]. Thermal stability also increased in PMMA [46], PHBV [56], and polyurethane [42].

1.4 CNF-Polymer Nanocomposite Fibers

CNF polymer fiber composites have been less studied than CNC polymer fiber composites due to the difficulties of working with CNFs. Due to the longer aspect ratios of CNFs compared to CNCs, CNFs has a much larger effect on rheology than CNCs [65]. Also the longer aspect ratio results in increased difficulty of preventing aggregation of the filler resulting in a stress concentrator in the composite [66].

Table 1.1 The effect of CNC on the elastic modulus and tensile strength of various polymer films reported in the literature.

Matrix	Neat Matrix Elastic Modulus (GPa)	Neat Matrix Tensile Strength (MPa)	CNC Loading (wt%) for Highest Elastic Modulus	Composite Elastic Modulus (GPa)	CNC Loading (wt%) for Highest Tensile Strength	Composite Tensile Strength (MPa)	Reference
PVA	1.8[a]	102[a]	12	2.7[a]	12	128[a]	[47]
PVA	1.3	N/A	10	1.9	N/A	N/A	[48]
PVA	1.3[a]	N/A	5	1.6[a]	N/A	N/A	[49]
PVA	N/A	57.02	N/A	N/A	5	75.20	[50]
PLA	0.91[a]	44.4	10	1.2895	6	71.6	[52]
PVDF	N/A	4.62	N/A	N/A	0.1	6.23	[53]
PP	N/A	19	N/A	N/A	6	27	[55]
PHBV	0.055[a]	12.5[a]	10	0.195[a]	10	31[a]	[56]
PHBV	0.82	14.1	5	1.76	5	26.1	[57]
ABS	3.3[a]	32[a]	0.7	4.45[a]	0.7	37[a]	[59]
Polyeurathane	0.045	54	5	0.076	2	69	[42]
Polyeurathane	0.04116	N/A	5	0.10028	N/A	N/A	[60]
Epoxy	N/A	27.1	N/A	N/A	10	48	[61]
Epoxy	2.2	40	15	3.6	15	60	[62]
Starch	0.3273	10	4.8	0.4396	4.8	15.6	[63]
Chitosan	1.59	79	5	2.971	5	99	[64]

[a] The exact values were not given in the paper, and these numbers are approximated from the graphs

Currently the highest loading of CNFs for a continuously spun and post drawn CNF polymer fiber composite is 1 wt% (dry-jet wet spinning), while for CNC polymer fiber composites there has been studies with loadings being as high as 60 wt% [67, 68]. We are defining continuously spun as a fiber that is spun and collected during the polymer suspension extrusion process. A 2 wt% CNF loaded PVA was attempted to be spun but the authors stated the solution has become a gel and could not be spun [67]. The fibers produced in that study had very good properties and 1 wt% CNF loading did not inhibit the fiber drawability and mechanical properties. The neat PVA had a maximum tensile strength of ~1.6 GPa and an elastic modulus of 48 GPa, while the 1 wt% CNF fiber had a maximum tensile strength of ~1.6 GPa and an elastic modulus of 57 GPa [68].

CNF-polymer fibers with CNF loadings greater than 1 wt% has been continuously spun, but continuous post drawing has not been done on these fibers. Post drawing of fiber is important, because this drawing aligns the polymer and nanofillers in the fiber direction, and this significantly increases the mechanical properties. Fiber that has been continuously spun but not continuously post drawn all used an electrospinning method. These fibers include PVA with up to 6.6 wt% CNF [69], PAN with up to 10 wt% CNF [70], polyethylene oxide (PEO) with up to 10 wt% CNF [71], and PVA/waterborne polyurethane (WPU) with up to 5 wt% CNF [72]. The PVA-CNF fiber elastic modulus increased from 45 MPa to 108 MPa and the tensile strength increased from 2 MPa to 4.8 MPa with the addition of 6.6 wt% CNF loading [69]. In the PEO-CNF fibers the best properties were exhibited at 4 wt% CNF loading the elastic modulus increased from 20 MPa to 51 MPa, and the tensile strength increased from 1.6 MPa to 2.2 MPa [71]. In the PVA-WPU-CNF

fiber the tensile strength was found to increase from ~14 MPa to ~20 MPa at 5 wt% CNF loading [72]. Higher loadings of CNF in polymer fibers have been achieved with the electrospinning method compared to other spinning methods. When electrospinning is done mats of fibers are typically made, and because a mat can't be drawn as much as a fiber spun with a process that uses a winder the properties of electrospun fibers after drawing is usually lower.

1.5 Functionalization

Functionalization of a material is the modifications of the material's surface chemistry to give it new surface properties. This modification can impart a variety of properties that the neat material does not exhibit, and the degree of functionalization can control how strong these properties are exhibited. Some reasons functionalization are done is to tune dispersibility, to control the interaction with a different material, and to tailor the interphase to improve mechanical properties [73, 74].

1.5.1 Cellulose Nanocrystal Functionalization

CNCs that are made through sulfuric acid hydrolysis are automatically functionalized with a sulfate group due to the processing method and commonly CNCs are used in this state. This sulfate functionalization allows CNCs to be better dispersed in certain solvents. CNCs can also be made through acid hydrolysis with different types of acid such as hydrochloric acid that will result in CNCs with no change in surface chemistry from starting cellulose material [75]. Many different types of functionalizations on CNCs have been studied. These functionalization are done to have the CNCs disperse better, to act as a catalyst, or for a number of other reasons [76]. A common functionalization done

to increase dispersibility is TEMPO oxidation. One of the reason this functionalization is preferred over the sulfate group functionalization is because the sulfate group is not thermally stable and cleaves off in solution. The sulfate group also decreases the thermal stability of the CNC [75, 77]. The TEMPO functionalization converts the cellulose C6 into a sodium carboxylate group and does not significantly affect the crystallinity. A simplified model of the reaction scheme can be seen in **Figure 1.5.** A more in depth proposed mechanism of what occurs between the TEMPO and the cellulose can be seen in **Figure 1.6** [76]. The sodium carboxylate groups can be reconverted back to a carboxylic acid groups by treating it in an acid. These H^+ or Na^+ will dissociate in water, leaving a negative charge on the cellulose. These negative charges will repel each other, giving a more stable and dispersible suspension of the cellulose [78].

1.5.2 Cellulose Nanofibril Functionalization

CNFs, similar to CNCs, have been functionalized for many different applications. The most common functionalization used to increase the dispersibility is the TEMPO oxidation reaction mentioned above [78]. Dispersion of TEMPO mediated oxidized CNFs can be seen in **Figure 1.7**. There are other methods for functionalization and functionalizations using periodate oxidation on CNFs (**Figure 1.8**) to form dialdehyde cellulose as a starting material has been gaining popularity. The dialdehyde cellulose does not increase dispersibility but many different types of functionalization can be done on the highly reactive C=O bonds to increase dispersibility, or for different applications [79]. Some functionalizations that can be done on CNFs after the periodate oxidation include chloride oxidation, sulfonation, and reductive amination. [79-81].

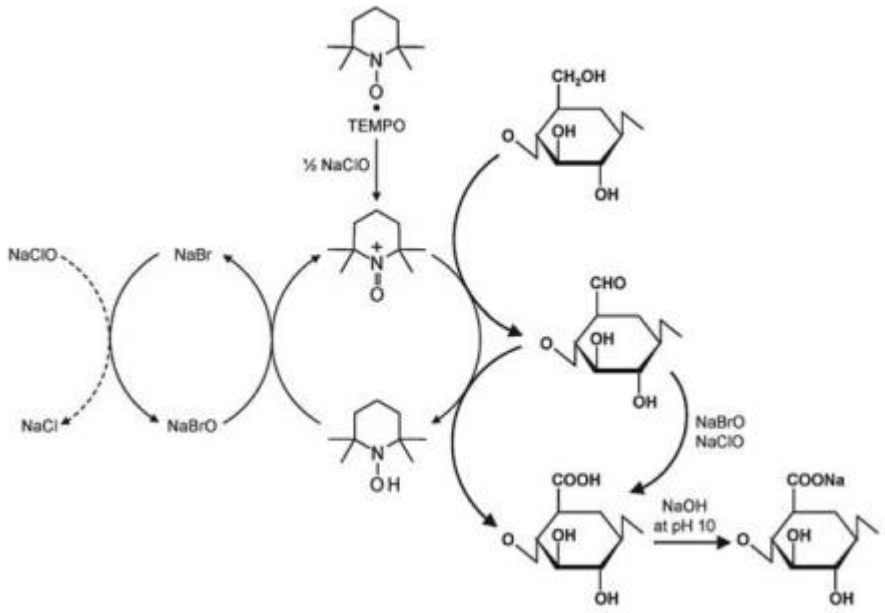

Figure 1.5. TEMPO mediated oxidation scheme of cellulose [78].

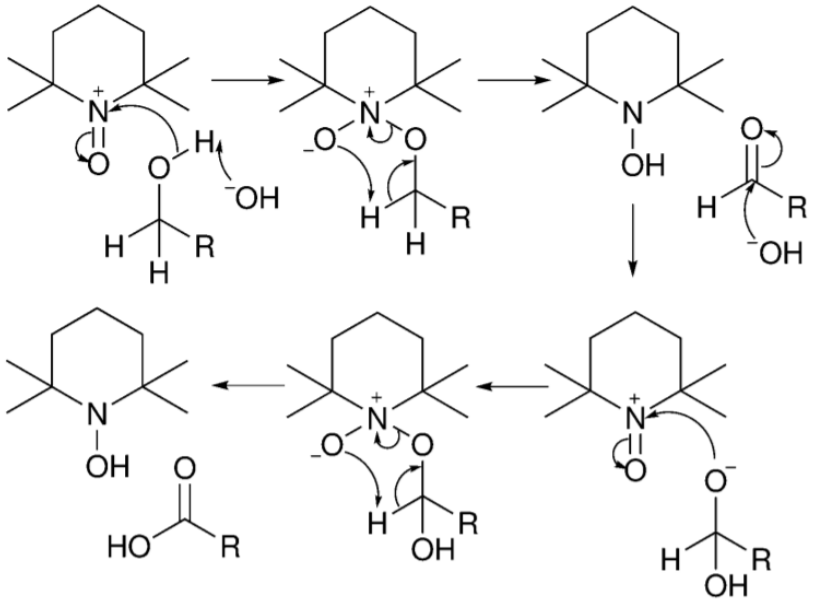

Figure 1.6. Proposed interaction between the TEMPO and the hydroxyls on the cellulose [76].

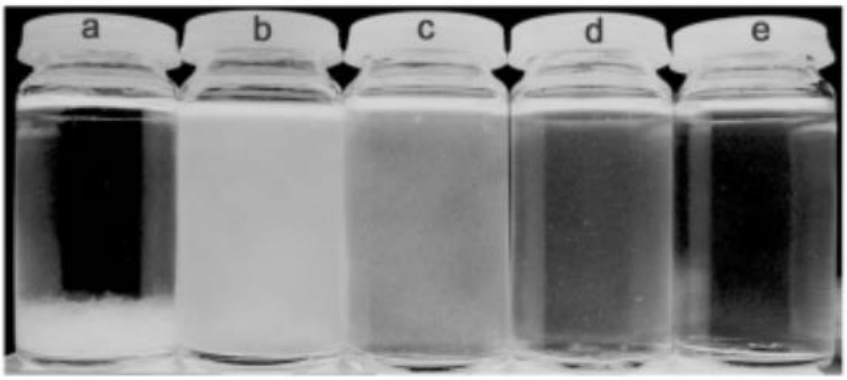

Figure 1.7. Dispersion of 0.1 wt% wood pulp treated with varying amounts of NaClO (mmol/gram of cellulose) during TEMPO mediated oxidation (increasing NaClO indicates more functionalization) **(a)** 0 , **(b)** 1.3, **(c)** 2.5, and **(d)** 3.8 mmol of NaClO/gram of cellulose. **(e)** supernatant of suspension "**c**" after centrifuging for 30 mins at 12000g [82].

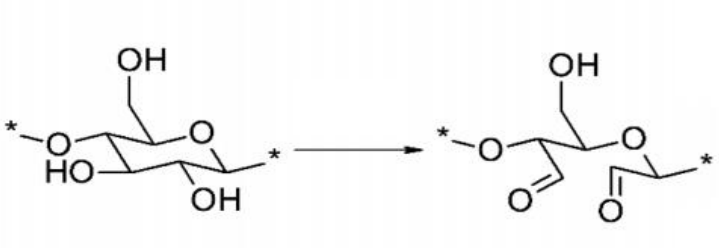

Figure 1.8. Cellulose structure and the periodate oxidated cellulose structure [81].

1.6 Fiber Spinning

There are many ways to spin fiber these techniques include melt spinning, electrospinning, wet spinning, dry spinning, dry jet wet spinning, gel spinning, and others. In melt spinning the polymer is melted and extruded through a die and picked up on a spool. Electrospinning involves applying a charge to the polymer solution and an opposite charge on the collector. For wet spinning the spinneret is in the coagulation bath and the polymer solution is extruded through the spinneret and pick up by a spool. For dry spinning the polymer solution is extruded through a spinneret into a gaseous medium such as air or

nitrogen and does not come in contact with a nonsolvent. For dry jet wet spinning the polymer solution is extruded through a spinneret into gaseous medium before going into a coagulation bath (**Figure 1.9**). Gel spinning is similar to dry jet wet spinning but involve a high molecular weight polymer, low solid content polymer solution, and typically a cold coagulation bath. The gel spinning process has a lower amount of entanglements in the fibers compared to the dry jet wet spinning process resulting in fibers with higher properties. Depending on the polymer and spinning conditions the spool of fiber might be put in a nonsolvent for a duration of time before being drawn. These factors in gel spinning allows low polymer entanglement, behaving like a gel instead of a true solid, and allows the fibers to be highly drawn leading to high mechanical properties. A diagram for gel spinning can be seen in **Figure 1.10** [83].

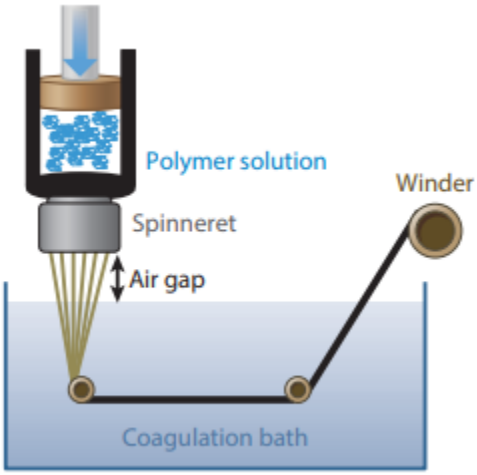

Figure 1.9. Schematic for the dry jet wet spinning process [83].

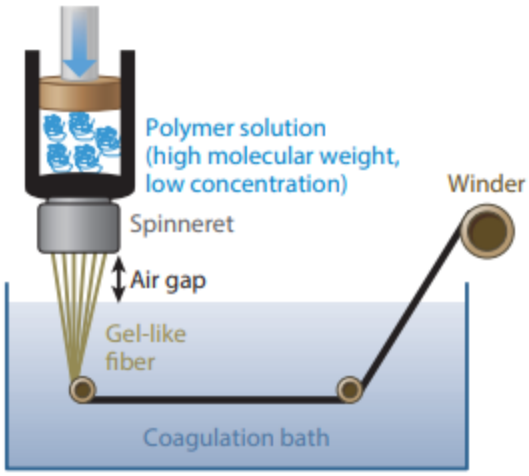

Figure 1.10. Schematic for the gel spinning process [83].

1.7 Stabilization

1.7.1 Stabilization of Polyacrylonitrile

To make PAN into a carbon material it must first undergo stabilization, which is a heat treatment process that is typically done in air at 200-300 °C [6, 57]. The stabilization process contains dehydrogenation, cyclization, oxidation, and crosslinking reactions a scheme for the stabilization of PAN is shown in **Figure 1.11**[84]. Cyclization and dehydrogenation can occur in inert atmosphere, while the oxidation requires the presence of oxygen. Crosslinking can occur to a small degree in an inert atmosphere during stabilization by intermolecular cyclization, but crosslinking is much more prominent in an oxygen atmosphere after the oxidation reaction. This allows separating the cyclization reaction from the oxidation reaction by first running the sample in an inert atmosphere, such as nitrogen, then followed by air, which can be seen in **Figure 1.12** [85, 86]. The

stabilization process changes the PAN from a linear polymer into a ladder structure, which increases the thermal stability to survive carbonization.

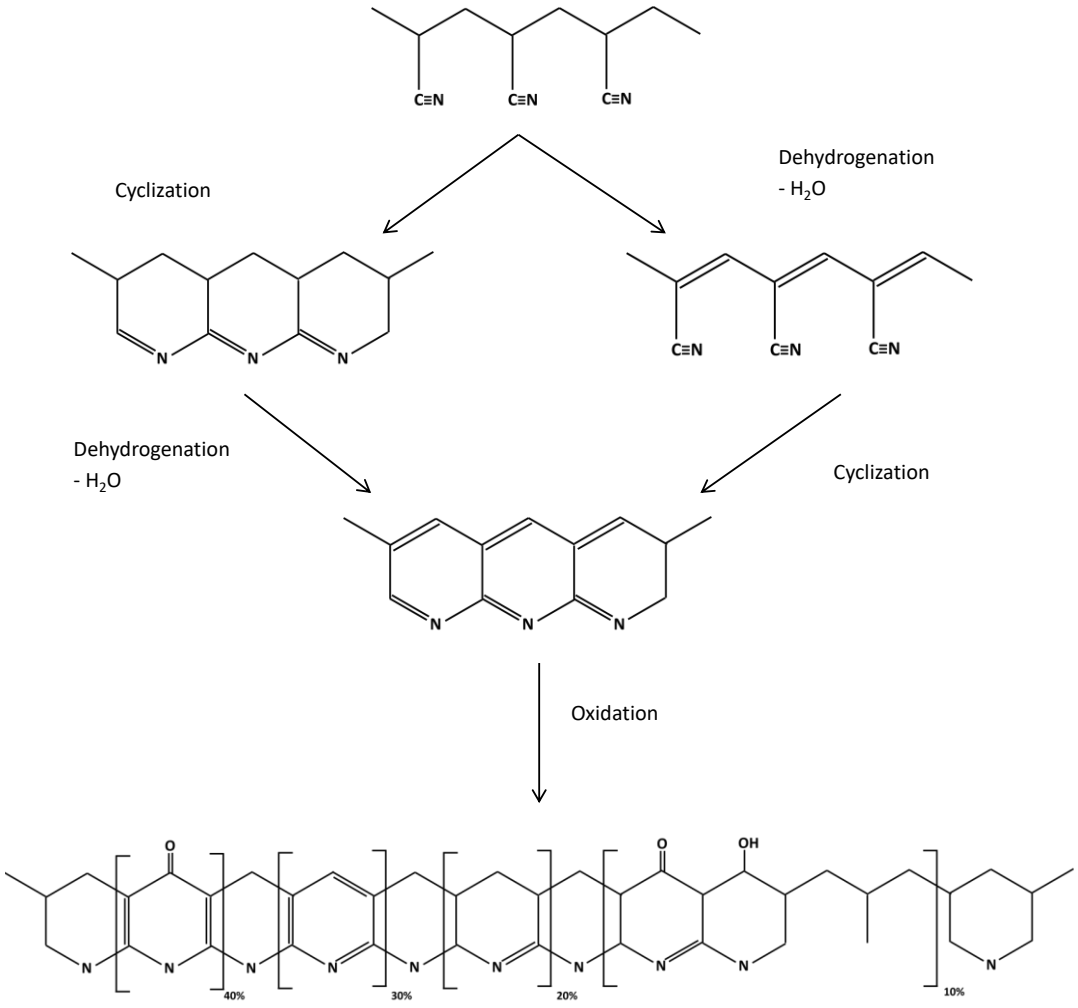

Figure 1.11. Proposed chemical pathway for PAN stabilization [4, 83].

There have been many studies on the stabilization of PAN and the earliest study dates back 1950 [84-94]. Though stabilization was studied in 1950, PAN fiber was first stabilized and carbonized in the early 1961 by Shindo at the Government industrial

Research Institute in Japan [6]. For the production of carbon fiber, homopolymer PAN is not used due to the narrow temperature range of the exothermic reaction during the stabilization process. This reaction is very rapid and releases large amounts of heat, which can locally damage the fiber and result in lowering the mechanical properties of the resulting carbon fiber due to imperfections in the fibers where it was damaged. To counter this problem acrylonitrile is usually copolymerized with another monomer, two examples are methacrylic acid (MAA) and itaconic acid (IA). These copolymers broaden the temperature range over which the exothermic reaction occurs, extending the time period over which the heat of reaction is released, which subsequently minimizes damage to the fiber [6].

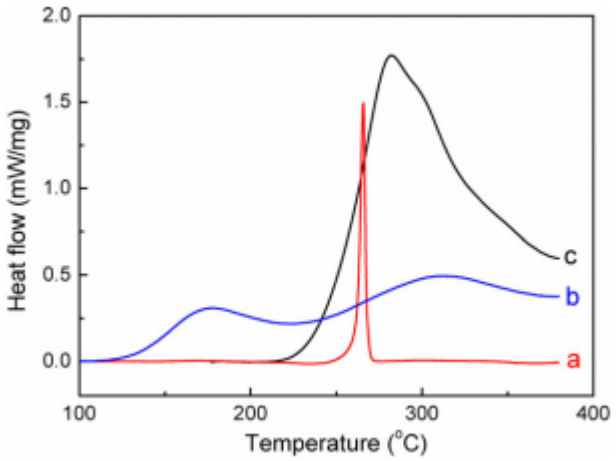

Figure 1.12. DSC curves of a PAN fiber under different atmospheres displaying separation of stabilization reactions under different environments: **(a)** Nitrogen, **(b)** sample "**a**" rerun in air, and **(c)** air [85].

1.7.2 Stabilization of Cellulose

Cellulose was the first materials to be used to make carbon fiber. Thomas Edison in the 1880s was one of the first people to use carbon fiber; it was produced from bamboo splints and cotton and used as the filament in his light bulbs. To convert cellulose into a carbon material, the cellulose similarly to PAN, it must undergo stabilization. The proposed reaction for the stabilization of cellulose by Tang and Bacon (**Figure 1.13**) contains dehydration (150-240 °C), thermal cleavage of the bridge oxygen and the pyranose ring also referred to as depolymerization (240-400 °C) [95-99].

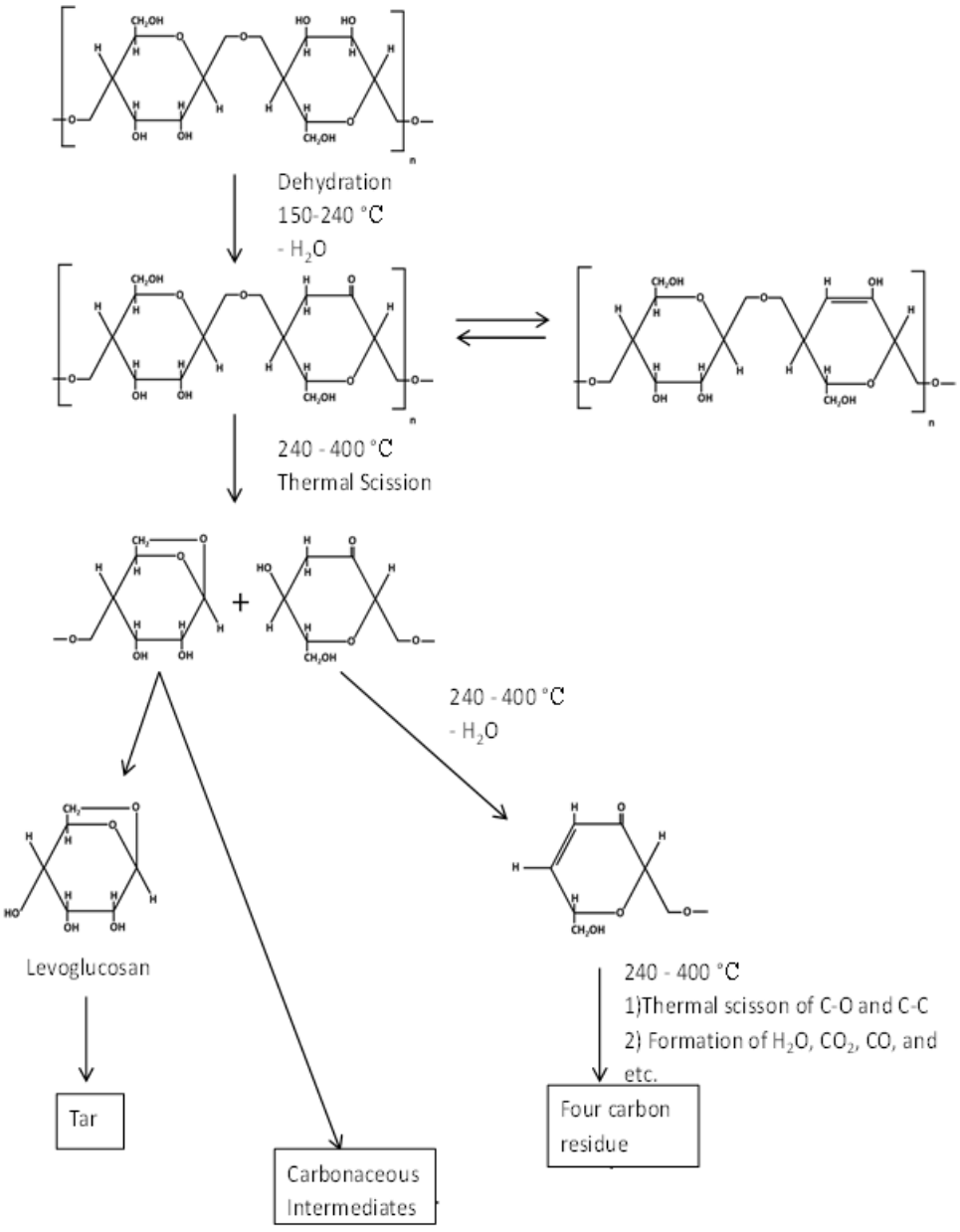

Figure 1.13. Schematic for the stabilization of cellulose [95].

1.8 Thesis Objectives

The objective of this thesis is to study nanocellulose as a filler in polyacrylonitrile. The reason nanocellulose is looked at is because it is a renewable biomaterial and has potential to reduce our dependence on synthetic polymer produce by oil, which is a contributor to climate change. The effect of nanocellulose addition on the properties of polyacrylonitrile composite films and fibers will be studied. Surface chemistry has a large effect on the dispersibility of nanocellulose and the interaction between polymer, because of this different functionalization were applied to CNFs. These different functionalizations were studied for their dispersibility in solvent and reinforcement capabilities in PAN. The stabilization kinetics of PAN and CNC composite films were also studied to determine if the addition of CNCs could increase the stabilization kinetics of PAN.

The following studies have been done and will be discussed in this thesis.

1. The effects of high loadings of CNCs on the thermal, mechanical, structural, and optical properties of PAN films. The rheological effect the CNC addition has on PAN suspensions were also looked. Loadings of up to 40 wt% CNC with respect to polymer were investigated.
2. The stabilization kinetics differences between PAN and PAN/CNC films were studied. The structural development changes between PAN and PAN/CNC films with heat treatment are also looked at.
3. A method to sulfonate CNF that mimics the same surface chemistry of CNC produce through sulfuric acid hydrolysis was investigated. This method retains the

CNF morphology and it can be done faster than the TEMPO oxidation method and other reported CNF sulfonation methods.

4. Reinforcement effects of CNF with different functionalizations on PAN fibers were studied. These two functionalizations were TEMPO oxidation and an amination. This amination functionalization has not been done on CNFs before. PAN fibers with CNF loadings as high as 10 wt% were made with continuous spinning and continuous post drawing. The previous highest reported polymer fiber made with continuous spinning and continuous post drawing had a loading of 1 wt% CNFs.

CHAPTER 2. INFLUENCE OF HIGH LOADING OF CELLULOSE NANOCRYSTALS IN POLYACRYLONITRILE COMPOSITE FILMS

2.1 Introduction

CNCs have high mechanical properties and have been studied by others for uses in polymers as a mechanical reinforcement filler. Typically, when polymer-CNC films are made using CNCs as a filler for mechanical reinforcement the loadings are relatively low and rarely go above 20 wt%. This is because at higher loadings, CNC aggregation occurs and behaves as stress concentrators leading to a decrease in mechanical properties [52, 100]. This decrease in mechanical properties due to aggregation can occur at low as 1 wt% CNC loading depending on the CNCs and processing conditions used to make the composite [53]. In this chapter PAN-co-MAA/CNC films were produced with loadings up to 40 wt% CNC through the solution casting method to study more in depth the effects of high CNC loadings in a polymer matrix. The structural, optical, mechanical, and thermal properties of the resulting films were investigated. The rheology of the PAN-co-MAA solution and the composite suspensions used to make the films were also investigated.

2.1.1 Materials

Polyacrylonitrile-co-methacrylic acid (PAN-co-MAA; 4 wt% of MAA content, viscosity average molecular weight: 2.47×10^5 g/mol) was obtained from Exlan Co., Japan, and will be referred to as PAN-co-MAA powder. Freeze dried CNC (lot# 2012-FPL-CNC-48/051) were obtained from the University of Maine, US, and will be referred to as freeze dried CNC. The dimensions of these CNC were previously measured to be approximately

6.3 nm in diameter and 153 nm in length [20]. Dimethylformamide (DMF) was obtained from Sigma-Aldrich co. and was distilled before use.

2.1.2 Solution/Suspension Preparation

The PAN-co-MAA solution and PAN-co-MAA/CNC suspensions were targeted to have a solid content of 3.7 wt% in DMF. Six different solution/suspensions were made with 0, 5, 10, 20, 30, and 40 wt% CNCs with respect to the weight of the polymer; these samples will be referred to as neat PAN-co-MAA, CNC-5, CNC-10, CNC-20, CNC-30, and CNC-40, respectively. To make one of the suspensions the desired amount of freeze dried CNCs (depending on the final CNCs content) were dispersed in 100 ml of DMF by a bath sonicator (Branson 3510R-MT, 100 W, 42 kHz) for 24 hours. The CNC/DMF suspension was then combined with PAN-co-MAA powder in a glass reactor and mechanically mixed at 200 rpm at 70 °C for 3 to 4 hours. The same procedure was followed to make the neat PAN-co-MAA solution except the first step of dispersing the freeze dried CNCs in DMF was not done. The air bubbles were removed from the solution/suspension in a vacuum oven at 70 °C for 5 minutes. Due to the solution/suspension preparation process the final solid content ended up higher than 3.7 wt% and the measured solid content of each solution/suspension is given in **Table 2.1**.

A 100 wt% CNC suspension was also made by dispersing the freeze dried CNCs in deionized (DI) water to make a 1 wt% solid content suspension, and will be referred to as neat CNC. (See Appendix A for discussion on solution/suspensions made but not discussed in this chapter due to processing difficulties)

Table 2.1. Solid content of the solution and suspensions used to make the films, and the volume percent CNCs in these suspensions.

	neat PAN-co-MAA	CNC-5	CNC-10	CNC-20	CNC-30	CNC-40
Solid Content[a] (wt%)	4.0	3.8	4.0	3.9	4.1	4.1
Volume percent CNC in Suspension	0	0.1	0.2	0.5	0.7	1.0

[a] Solid content (polymer and CNC) of the solution and suspensions used to make the films and rheology study, solid content was measured with thermal gravimetric analysis under nitrogen atmosphere at 180 °C

2.1.3 Film Preparation

Neat CNC films were made by solution casting into a polystyrene petri dish and dried in an oven at 70 °C for 2 days. This film was used only in thermogravimetric analysis, differential scanning calorimetry, and wide angle x-ray diffraction. The neat PAN-co-MAA and PAN-co-MAA/CNC films were made by solution casting (4 hours after the solution/suspension has been made) into a glass mold, and dried in an oven at 70 °C for at least 4 hours. The neat PAN-co-MAA and PAN-co-MAA/CNC films were removed from the oven, cooled down to room temperature, then submerged in deionized (DI) water for 30 minutes, and removed from the glass mold. This film was then placed between two glass plates and a normal stress of around 80 Pa was applied to the film. This assembly was placed in a drying oven at 70 °C for 12 hours to remove residual stress that would otherwise cause the film to curl.

To make tensile and DMA specimens the films were rehydrated by submerging in DI water until they could be cut without cracking (~1 hour). These films were then cut into

rectangular strips using a cutting apparatus incorporating a razor blade. These film strips were then placed between the two glass plates and a normal stress of around 80 Pa was applied to the strips. This assembly was placed in a drying oven at 70 °C for 12 hours. The strips were then taped onto paper tabs and further dried under vacuum at 40 °C for 24 hours. The samples were stored in a desiccator until testing to help minimize moisture uptake to help mitigate moisture induced effects on the mechanical properties of the films. The thickness of these samples can be found in **Table 2.2**. (See Appendix A for discussion on film processing trial and error)

2.1.4 Characterization

Rheological measurements were performed on an ARES rheometer (Rheometric Scientific, Co.). The testing was done at room temperature, with 50 mm parallel plates, and a gap size of 1 mm. To prevent evaporation of solvent and absorption of water during testing, a layer of silicon oil was applied to the exposed sample surface around the sides of the parallel plates. The linear viscoelastic region (LVR) was determined for each sample by running a strain sweep test at an oscillatory frequency, ω, of 5, 10, and 100 rad/s. A frequency sweep was done from 5 to 100 rad/s in the LVR for each sample, and then the same sample between the plates was immediately ran again for a second run with the same parameters. By comparing the first and second runs of the frequency sweep it is possible to assess if solvent evaporation, water adsorption, or if a breakdown of a percolation network took place during the test. The bulk solution/suspension samples were kept in vials, sealed with Teflon tape and stored in a dark cabinet at room temperature to help prevent evaporation of solvent, and to prevent degradation of the polymer due to light for

the rheology aging study, since PAN is known to degrade when exposed to ultraviolet radiation [101]. For the rheology aging study each sample was tested at 4 hrs, 4 days, 14 days, 30 days, and 90 days after the solution/suspension has been made. The aged solution/suspensions solid content was checked with a TGA and it was determined that there was no change in the solid content over the 90 day period.

Fourier transform infrared spectroscopy (FTIR) was done on a Magna 560 FTIR (Nicolet Instruments) to study the interactions between the PAN-co-MAA and CNC. The tests were done on neat PAN-co-MAA and composite films, but the pure CNC spectra was done with the freeze dried CNC powder and KBr due to the difficulties of making a thin enough film. The scan range was 400 cm^{-1} to 4000 cm^{-1} with resolution of 0.5 cm^{-1}. Wide-angle X-ray diffraction (WAXD) was done with Rigaku MicroMax-002 (CuK_{α}, λ=0.1542 nm) and a Rigaku R-axis IV++ detector. MDI Jade 9 software was used to analyze the WAXD pattern.

Table 2.2. Thermal and mechanical properties of the films. Also the film dimensions and the volume percent CNC in the films.

	neat PAN-co-MAA	CNC-5	CNC-10	CNC-20	CNC-30	CNC-40
Vol % CNC in films	0	3.8	7.6	15.7	24.2	33.2
Film Thickness[a] (μm)	93 ± 5	104± 4	117 ± 9	105 ± 1	115 ± 5	104 ± 3
Elastic Modulus (GPa)	2.2 ± 0.1	2.4 ± 0.1	2.4 ± 0.1	3.0 ± 0.1	3.2 ± 0.1	3.7 ± 0.1
Tensile Strength (MPa)	75 ± 3	84 ± 3	91 ± 4	97 ± 9	116 ± 6	132 ± 9
Strain at Break (%)	27.3 ± 16.4	9.9 ± 3.1	5.3 ± 0.6	4.0 ± 0.8	4.3 ± 0.3	4.2 ± 0.4
Storage Modulus at 35 °C (GPa)	3.9	4.4	5.3	7.3	9.0	10.5
Tg[b] (°C)	92	96	97	106	118	N/A

[a] Film thickness of the samples used for tensile test and dynamical mechanical analysis

Ultraviolet-Visible (UV-Vis) spectroscopy was done to determine the transparency of the films; measurements were done on a Lambda 35 (PerkinElmer Co.). The scan was done over a range of 200 to 800 nm with a scan speed of 480 nm/min with a resolution of 1 nm. To assess the degree of micron sized CNC agglomerations in the films, polarized light microscopy (Leica DM2500 P, Leica Microsystems) was used to determine if there were regions of birefringence, which can be caused by agglomeration of CNC [61]. Films were observed in transmission mode under cross polarizers with an objective of 4x. To further characterize dispersion the fracture surface of the films after tensile testing were sputtered with gold and observed by scanning electron microscope (Zeiss Ultra60 FE-SEM).

Thermal stability and degradation were investigated with thermogravimetric analysis (TGA) with TA instruments Q500. Samples were dried under vacuum at 70 °C for 24 hours and stored in a desiccator until they were tested. These samples were tested within 5 minutes from being removed from the desiccator. Samples were tested under both air and nitrogen atmosphere with the sample size ranging from 5-6 mg. The samples were heated from 50 to 795 °C at a heating rate of 10 °C/min. Differential scanning calorimetry (DSC) was ran on TA instrument Q100. Sample sizes of ~3 mg were used in standard aluminum pans, and heated from 50 to 300 °C at 10 °C/min in air.

Dynamic mechanical analysis (DMA) and tensile testing were completed using a RSA III solids analyzer (Rheometric Scientific Co.). The samples tested were rectangular strips having a gauge length of 12.7 mm, width of ≈2.2-2.5 mm, and an average thickness of ~100 μm (see **Table 2.2**). The width of each specimen was measured in nine different

areas with an optical microscope (Leica DM2500 P, Leica Microsystems) and ImageJ, while the thickness was measured with a digital micrometer (Mitutoyo 331-361 Type B) in three different areas. To maintain consistency if the variation of width and thickness were greater than 100 µm and 10 µm, respectively, the samples were not used. Dynamic mechanical tests were conducted at a frequency of 1 Hz, 0.1 % dynamic strain, over a temperature range of 35 to 170 °C with a heating rate of 1 °C/min. Tensile tests were completed at room temperature at a strain rate of 5 %/min. Tensile testing continued until there were at least five samples that did not break at the grip for each different composition. For the specimens that broke at the grip, the results were not used due to the possibility that the fracture occurred because of stress concentration caused by the grips.

2.2 Results and Discussion

2.2.1 Rheology of PAN-co-MAA/CNC suspensions

The effect of frequency (up to 100 rad/s), CNC loading (up to 1 vol%), and aging time (4 hrs, 4 days, 14, days, 30 days, and 90 days) on the complex viscosity of PAN-co-MAA/CNC suspensions were measured (frequency sweep plots for all samples are shown in Appendix A **Figure A.1**). The frequency sweep plots of the solution/suspensions used to cast the films (4 hrs age time) is shown in **Figure 2.1(Left)**. The first and second runs for all the samples tested at each age were similar, indicating that there was little to no solvent evaporation or water absorption during the test. This also indicates that the structure within the suspension is consistent between the runs. The comparison between the first and second runs can be seen in **Figure A.2**. The neat PAN-co-MAA solution had a Newtonian behavior up to 100 rad/s, while the incorporation of CNCs lead to suspensions having a

shear thinning behavior. The mechanism causing the shear thinning behavior is likely due to the alignment of the rod-like CNCs during shear, which has been observed in other CNC systems [51, 60] and other high aspect ratio particle systems, such as carbon nanotubes and titanate nanotubes [102, 103]. Overall, there is a general trend of increasing viscosity with increasing CNC loading over all frequencies and for all aging times (**Figure A.1**). For the aging times of 4 to 90 days this trend was observed, however at the 4 hour aging time the CNC-20 and CNC-40 had viscosities a bit lower than expected. The increase in viscosity with increasing CNC loading is expected at low shear rates because the CNC behaves like a filler in the suspension.

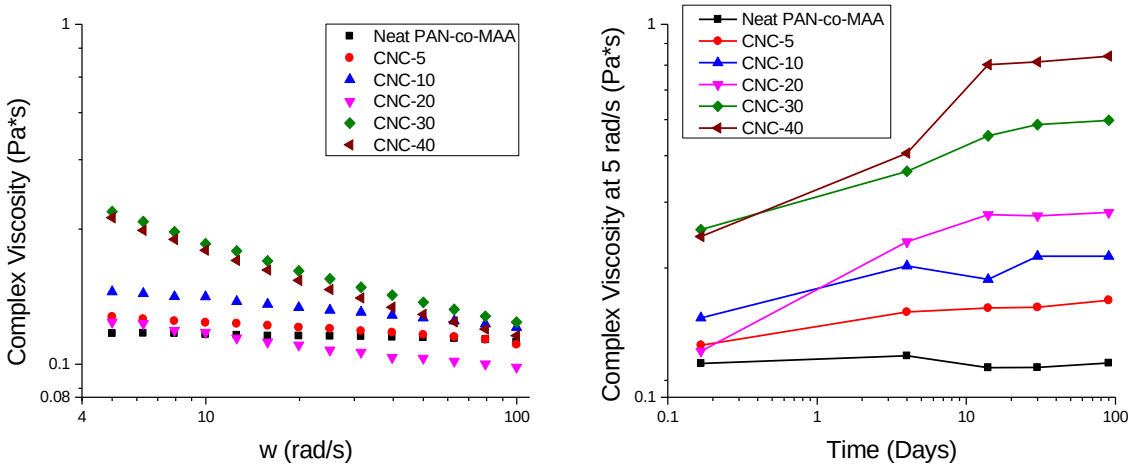

Figure 2.1. Complex viscosities of solution/suspensions **(Left)** 4 hours after being made (frequency sweeps from 5 to 100 rad/s), and **(Right)** over a 3 months period at 5 rad/s. Solid contents of these solution/suspensions can be found in **Table 2.1**.

The effect of aging time (up to 90 days) and CNC loading (up to 1 vol%) on complex viscosity (at 5 rad/s) is shown in **Figure 2.1(Right)**. All of the PAN-co-MAA/CNC suspensions were observed to have increasing viscosity with increasing aging time, in contrast, the viscosity of the neat PAN-co-MAA solution was minimally affected

or had a slight decrease in viscosity. There was larger increase in viscosity over time with higher CNC loading, but the extent of change effectively stopped after 2 weeks for all samples. The increase in viscosity of the suspension with aging time is considered to result from polymer-filler interaction, as opposed to the formation of a percolated CNC network. Polymer adsorption onto fillers have been previously reported to increase the viscosity of a system with time [104, 105]. This scenario may be possible with PAN-co-MAA adsorbing onto the CNC over time, though we do not provide any direct evidence for this in this study. In contrast, the study by Derakhshandeh et al [35] showed that CNC network formation in a neat CNC suspension (10 wt% solid) can increase viscosity of the system with time. In our system the increase in viscosity with time is not believed to result from the formation of a CNC network structure for several reasons. First, testing was done in the linear viscoelastic region, determined in lead up experiments, so the structure within the suspension is recovering during the testing. Secondly, the suspensions are shear thinning indicating alignment of CNC in the shear direction. Also the viscosity curves of the first and second run of the same sample are very similar, this indicates no change in structure within the suspension that was not recovered between the first and second run. If the increased viscosity was due to CNC-CNC percolation the first and second runs should be different as there would be insufficient time for the percolation network to reform, since the second run was ran immediately after the first run while the increase in viscosity was developed over a longer period of time (hours to months). Finally, the vol% of CNCs used in the current study was at or below 1 vol%, which is below the percolation threshold of ~2.9 vol% for the aspect ratio of the CNCs used in our system [34] (see percolation

threshold calculations in supporting documentation). The tensile properties of films made from an aged suspension was looked at, and it was found that there might be some changes that occur due to aging. Though a more in-depth study needs to be done. Discussion and process for making these films from an aged suspension can be found in Appendix A.

2.2.2 Chemical Interaction and Structure

FTIR results for the film are given in **Figure 2.2**. The characteristic peaks for PAN is the peak at 2243-2240 cm^{-1} belonging to the CN (nitrile), and the peak at 1733-1723 cm^{-1} belongs to the carbonyl group in the methacrylic acid (MAA). The peaks at 2940-2930, 2850, 1450 , 1360 , and 1050 cm^{-1} belong to aliphatic CH, CH_2, and CH_3 in the PAN or MAA [106]. For the CNCs the characteristics peaks at 3490-3175 and 1649-1634 cm^{-1} belongs to OH (hydroxyl), 2900 and 1382 -1375 cm^{-1} belongs to CH, and the peaks at 1430-1420 and 1317 cm^{-1} belong to CH_2 [107]. There is no observable interaction from the FTIR between the CNCs and the PAN as determined from the lack of shift of the CN peak, and no observable new peaks developing. There was an observed shift of the peak related to the carbonyl group of MAA, the peaks shifted from 1724 cm^{-1} in neat PAN-co-MAA to 1734 cm^{-1} in the CNC-10 film and stayed around 1734 cm^{-1} at higher CNC loadings (**Figure 2.2 Right**). This indicates that there is interaction between the CNC and the MAA copolymerized with the PAN. There have been previous studies that showed interaction between carbonyl and hydroxyl groups [56, 57, 108].

The incorporation of CNCs into the PAN-co-MAA matrix did not have significant influence on the percent crystallinity of the PAN-co-MAA as estimated by WAXD. The procedure and results can be found in Appendix A (**Figure A.8-A.10**).

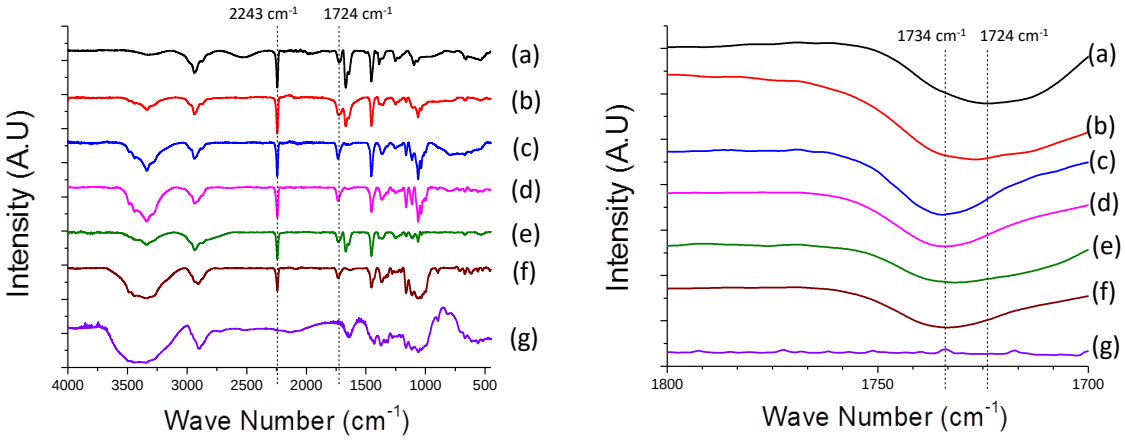

Figure 2.2. FTIR spectra of films (Left) FTIR full spectrum, (Right) FTIR spectrum from 1800 to 1700 cm^{-1} to display carbonyl peak shift with the addition of CNCs. **(a)** neat PAN-co-MAA, **(b)** CNC-5, **(c)** CNC-10, **(d)** CNC-20, **(e)** CNC-30, **(f)** CNC-40, **(g)** freeze dried CNC.

2.2.3 Optical Properties

The addition of up to 40 wt% CNCs loading did not have a detrimental effect on the optical transparency and color, which can be seen in **Figure 2.3**. The films look homogenous at the macro scale. To estimate the degree of CNC agglomeration at a finer length scale (e.g. micron-sized agglomerates), polarized light microscopy was used. Differences in birefringence between the polymer matrix and agglomerated CNC domains have been used to qualitatively assess the extent of CNC agglomeration within composites [61]. In our system, there is little observable birefringence within the majority of the neat PAN-co-MAA and PAN-co-MAA/CNC films (**Figure A.3**), suggesting a limited amount of micron sized CNC agglomeration. Incidentally, there were isolated

regions of increased birefringence (**Figure A.4**), these areas were considered worst-case-scenarios, and were not representative of the whole film. With this in mind, and considering the study by Girouard et al [61] that showed extensive birefringence at 5 wt% CNC loading, which is considerably lower than the loadings used in the current study (up to 40 wt%), it can be considered that the PAN-co-MAA/CNC composite films had a low degree of micron sized CNC agglomeration. In support of this, fracture surfaces of PAN-co-MAA/CNC composite films do not show fracture features that would be indicative of micron sized agglomerates (**Figure 2.4**).

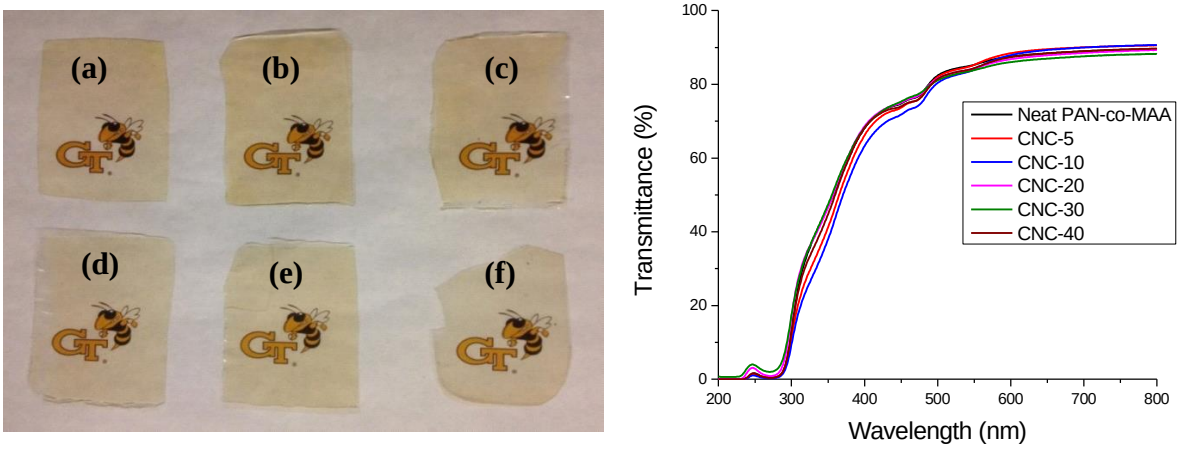

Figure 2.3. (Left) Optical images of films displaying transparency **(a)** neat PAN-co-MAA, **(b)** CNC-5, **(c)** CNC-10, **(d)** CNC-20, **(e)** CNC-30, **(f)** CNC-40. **(Right)** UV-Vis spectra showing small differences in transmittance of the films (all thicknesses comparable).

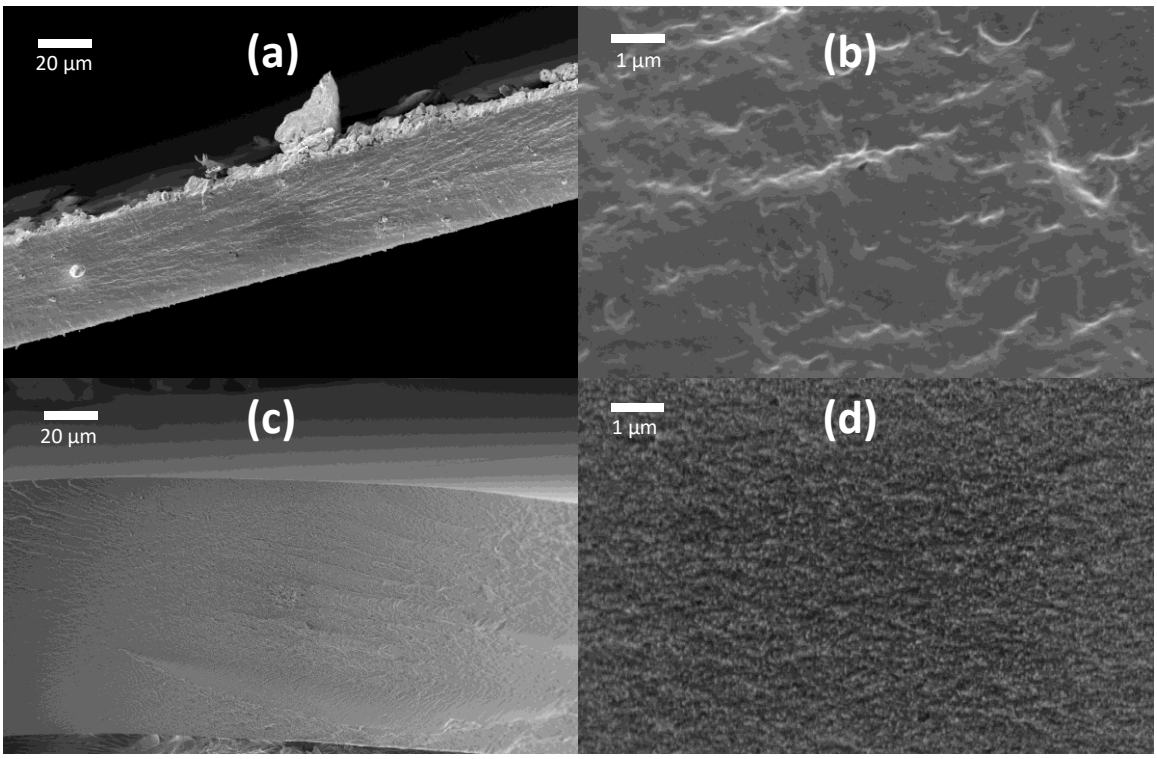

Figure 2.4. SEM images of the fracture surfaces of films after tensile testing **(a)** neat PAN-co-MAA **(b)** neat PAN-co-MAA **(c)** CNC-40, and **(d)** CNC-40. No apparent aggregations are seen in the CNC-40 film. The neat PAN-co-MAA is significantly thinner in these images because of the large amount plastic deformation during tensile testing, compared to the CNC-40 film.

2.2.4 Thermal Properties

Thermal stability studies on the films with similar thickness were conducted using TGA in both air and nitrogen, and the results of these tests are shown in **Figure 2.5**. The nanocomposites had better thermal stability (e.g. lower weight loss) up to ≈350 to 375 °C depending on the CNC loading compared to the neat PAN-co-MAA film in both air and nitrogen. This is surprising because the neat CNC film has much lower thermal stability compared to the neat PAN-co-MAA film at these temperatures. This unusual behavior of

CNC-polymer composites having better thermal stability than both the neat polymer and the neat CNCs have been reported before [42, 56].

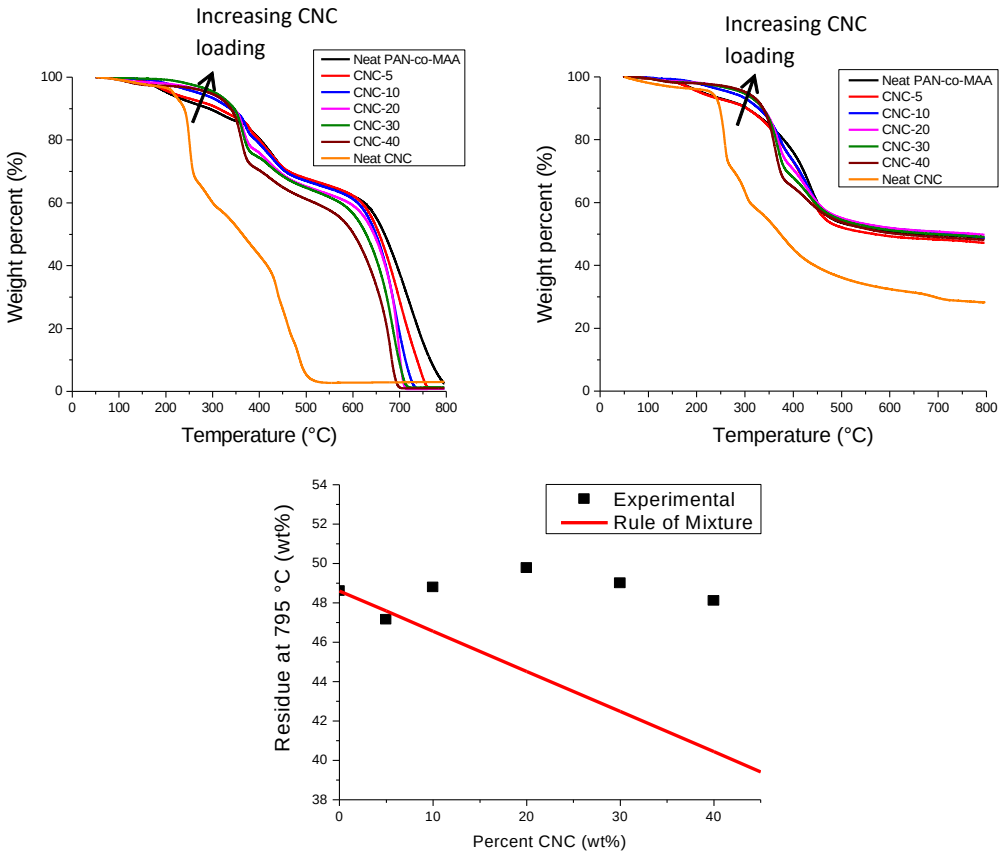

Figure 2.5. TGA results of the films at a heating rate of 10 °C/min **(Top Left)** in air 50-795 °C, **(Top Right)** in N_2 50-795 °C, **(Bottom)** experimental and rule of mixture residue (wt%) of the films from the rule of mixtures at 795 °C in N_2.

An unexpected result is the residue yield after heating up the films up to 795 °C in nitrogen atmosphere. The neat PAN-co-MAA and all the nanocomposite films had a residue yield around 50 wt%, while the neat CNC film had a residue yield of around 30 wt% as seen in **Figure 2.5**. This means that the degradation of the composites does not follow the rule of mixtures, and indicates chemical interaction between the CNCs and

PAN-co-MAA as the composite undergoes heating. A graph of the experimental and rule of mixture residue yield can be seen in **Figure 2.5 (Bottom)**. The experimental and rule of mixture degradation graph of CNC-40 in both air and nitrogen can be seen in **Figure A.5**.

The tan δ peak is the Tg of the system (**Figure 2.6**), and it was seen that it increased with increasing CNC content. The Tg for the neat PAN-co-MAA was 92 °C and increased to 118 °C for CNC-30. Tg for CNC-40 could not be determined due to no observable peak. The Tg was also determined by DSC and a similar trend of increasing Tg with increasing CNC loading was seen and can be seen in **Table A.1** and **Figure A.7.** The tan δ peak height also decreased from 0.27 for neat PAN-co-MAA to 0.11 for the CNC-30. A lower tan δ indicates lower chain mobility, this is likely due to the long rigid rod-like CNCs physically constraining polymer movement.

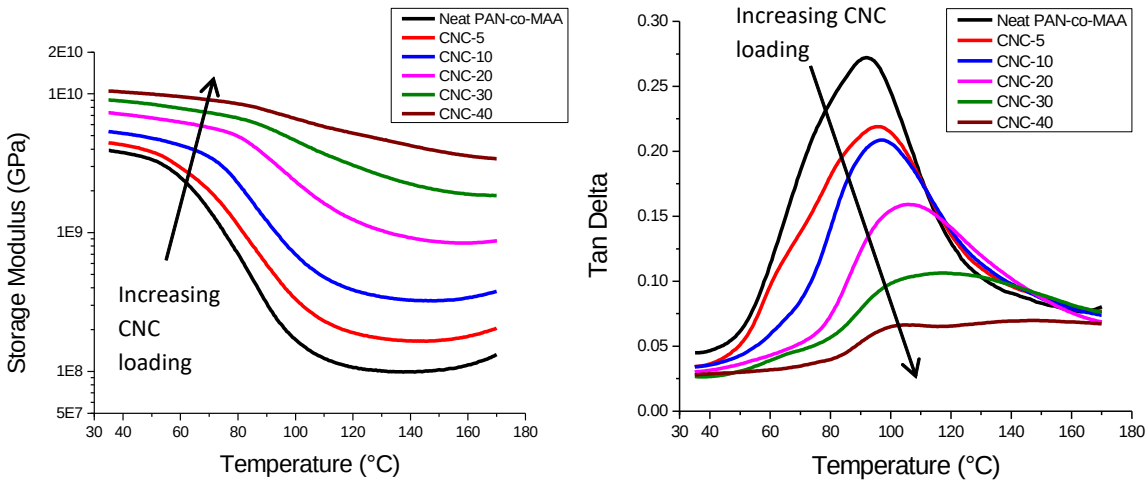

Figure 2.6. Dynamical mechanical analysis results of films at a frequency of 1 Hz (Left) Storage Modulus, (Right) Tan Delta.

2.2.5 Mechanical Properties

The storage modulus of the films measured at a frequency of 1 Hz are given in **Figure 2.6** and **Table 2.2**. There was a trend of increasing storage modulus with increasing CNC loading. At 35 °C the storage modulus for the neat PAN-co-MAA and CNC-40 film was 3.9 and 10.5 GPa, respectively. With higher CNC loadings the reduction in the storage modulus with increasing temperature was decreased. This is likely due to the filler and polymer interaction, and also possibly a CNC percolation network within the films. The CNC percolation network is less sensitive to temperature compared to the PAN-co-MAA matrix. At 20 wt% and higher CNC loadings there is a large increase in the storage modulus at the plateau temperature indicating that a CNC percolation network has possibly formed. The storage modulus was also seen to increase in some of the films after the plateau temperature, this is due to the PAN-co-MAA undergoing cyclization. The onset of this increase in storage modulus increased with increasing CNC loading, likewise the cyclization onset temperature also increased with increasing CNC loading (**Table A.1 and Figure A.7**).

The tensile testing results are given in **Table 2.2**. There was a trend of increasing elastic modulus and tensile strength with increasing CNC loading. There was also a trend of decreasing strain at break with increasing CNC loading up to 20 wt% CNCs, but above 20 wt% CNC loading there was not much change. The comparable strain at break at 20 wt% CNC and above is considered to result from a similar failure mechanism associated with the breaking of a percolated CNC network structure. In partial support for this, the storage modulus data at 20 wt% CNC and above indicated that a percolation network had

formed. Comparing the neat PAN-co-MAA to the CNC-40 film, the elastic modulus increased from 2.2 to 3.7 GPa, the tensile strength increased from 75 to 132 MPa, while the strain a break decreased from 27.3 to 4.2 %, respectively. These changes in properties due to the addition of CNCs may be a result from several mechanisms, such as increased crystallinity of PAN-co-MAA, PAN-co-MAA/CNC interfacial interactions, CNCs acting as a reinforcement phase, and/or the formation of a CNC percolation network. WAXD results indicate that the increase in mechanical properties was not due to higher crystallinity of the PAN-co-MAA (see description in **Appendix A**).

The role of the PAN-co-MAA/CNC interface on properties was considered by assessing the interfacial shear strength, which would give an indication of the load transfer between the matrix phase and the CNC reinforcement phase. The equation for the critical interfacial shear strength needed between the CNC and the matrix for the tensile strength of the CNC to be fully utilized can be found in **Equation 2.1**. Where τ_c, σ_f, D, and L are the critical shear strength of the interface, tensile strength of reinforcement (CNC), diameter of reinforcement, and length of reinforcement, respectively [109]. Using a CNC length of 153 nm, diameter of 6.3 nm, and a tensile strength of 7.5 GPa [11] the critical shear strength of the interface would need to be 154 MPa to fully utilize the tensile strength of the CNCs. The interfacial shear strength between various polymers and various types of reinforcements typically does not exceed 80 MPa [110-114] .

$$\tau_c = \frac{\sigma_f D}{2L} \qquad \textbf{(2.1)}$$

To estimate the critical reinforcement length needed to fully utilize the tensile strength of the CNC reinforcement for our system, the Thomason modified [115] Kelly and Tyson [116] equation for randomly oriented short fiber composites was used. Assuming all the CNCs are the same length and diameter, and individually dispersed, the modified equation for tensile strength of the composite, σ_c, is given in **Equation 2.2**. Where η_0, ϕ_1, σ_f, σ_m, L and L_c are the orientation factor of reinforcement, volume fraction of reinforcement, tensile strength of reinforcement, tensile strength of matrix, length of reinforcement, and critical reinforcement length, respectively. For a 2-D randomly oriented composite the η_0 can be assumed to be 3/8 [115, 117]. The elastic modulus of the matrix used was the elastic modulus of the neat PAN-co-MAA film which was 2.2 GPa. Solving the equation with the experimental data gave a critical reinforcement length of 876 nm (**Figure A.6**), and plugging this value back into **Equation 2.1** gave an interfacial shear strength of 27 MPa. This should only be considered as an estimate as the actual interfacial shear strength might either be lower due to the possible formation of a CNC percolation network within the films or could be higher if the CNCs are not individually dispersed in the matrix. Combining these results with the measured average CNC length used in the current study, 153 nm, it suggests that it is not possible to fully utilize the tensile strength of the CNCs in the PAN-co-MAA composites.

$$\sigma_c = \eta_0 \frac{\phi_1 \sigma_f L}{2L_c} + (1 - \phi_1)\sigma_m \qquad \textbf{(2.2)}$$

To estimate the effectiveness of CNCs in stiffening the PAN-co-MAA film the Cox-Krenchel model **(Equation 2.3**) for short fiber composites was used. The Cox-Krenchel model assumes the reinforcement and matrix respond elastically, no axial loading on the reinforcement ends, and that there is a perfect matrix/reinforcement interface [118]. The terms η_0, η_L, E_c, E_f, E_m, and ϕ_1 represent orientation factor of reinforcement, reinforcement stress transfer efficiency, elastic modulus of the composite, effective elastic modulus of reinforcement, elastic modulus of matrix, and volume fraction of reinforcement, respectively. The η_L (reinforcement stress transfer efficiency) can be calculated with **Equation 2.4** with the variable β being equal to **Equation 2.5**. The terms ν_m, L, D, and P_f represents Poisson ratio of the matrix, length of reinforcement, diameter of reinforcement, and packing factor of the reinforcement [119, 120]. The length and diameter of the reinforcement used was 153 nm and 6.3 nm, respectively. The square packing factor, π/4, is often used for CNC composites, and was used for our calculations [121-123]. The Poisson ratio of the PAN matrix used was 0.07 [124].

$$E_c = \eta_0 \eta_L \phi_1 E_f + (1 - \phi_1) E_m \quad \textbf{(2.3)}$$

$$\eta_L = 1 - \frac{\tanh(\frac{\beta L}{2})}{\frac{\beta L}{2}} \quad \textbf{(2.4)}$$

$$\beta = \frac{2}{D} \sqrt{\frac{E_m}{(1+\nu_m) E_f \ln(\sqrt{\frac{P_f}{\phi_1}})}} \quad \textbf{(2.5)}$$

Using **Equations 2.3-2.5** and the methods of least squares, solving for E_f the effective elastic modulus of the CNC was calculated. Fitting the data gave an effective CNC elastic modulus of 19 GPa (**Figure 2.7**). This is much lower than the experimental

and theoretical elastic modulus of CNCs, which is 110-220 GPa, suggesting that the CNCs are underutilized in stiffening PAN-co-MAA. Considered here are two plausible mechanisms for why the CNC effective modulus was lower than the experimental and theoretical CNC modulus, i) CNC agglomeration within the matrix, and ii) less than 100% efficient stress transfer across the CNC matrix interface. CNC agglomeration is not desirable as it effectively results in a larger sized reinforcement particle, which significantly lowers CNC/matrix surface area, and has diminished mechanical properties as compared to individual CNCs. Using the Cox-Krenchel equations, larger sized CNC agglomerate should lead to lower reinforcement efficiency. The low extent of CNC agglomeration in the PAN-co-MAA/CNC films qualitatively assessed from optical and polarized microscopy, suggests this may not be the dominate mechanism. In contrast, the PAN-co-MAA/CNC interface is most likely non-ideal so that the 100% efficient stress transfer assumed in the Cox-Krenchel model would be unrealistic, suggesting this may be a more dominate mechanism. In partial support for this, the calculated interfacial shear strength of 27 MPa (from **Equation 2.1**) is low, and FTIR results showed there was no observable interaction between the CNC and the PAN, while there was interaction between the CNC and MAA, but the MAA only compromises of 4 % of the polymer.

Comparing the results of the current study to the study by Chang et al. [41] which studied the role of CNC addition to PAN-co-MAA/CNC fibers. The addition of 10 wt% CNC loading was shown to increase the elastic modulus of the neat fibers from 14.5 to 19.6 GPa, and the tensile strength from 624 to 709 MPa. These properties are considerably higher than the neat and composite films produced in the current study (see **Table 2.1**).

While the same polymer and CNCs were used, the differences in properties are considered to be associated with increases in CNC alignment, PAN-co-MAA polymer alignment, and in PAN-co-MAA crystallinity within the fiber as compared to the films, each of which have been shown to increase composite stiffness in the direction of alignment [26, 33, 125, 126]. The larger increase in properties with the addition of CNCs is likely due to the increase of PAN-co-MAA crystallinity with increasing CNC loading, and the highly aligned CNCs, Herman's orientation factor of 0.9. While in contrast for the films discussed in this chapter the PAN-co-MAA and CNC had a 2-D random orientation, with no change in crystallinity with the addition of CNC.

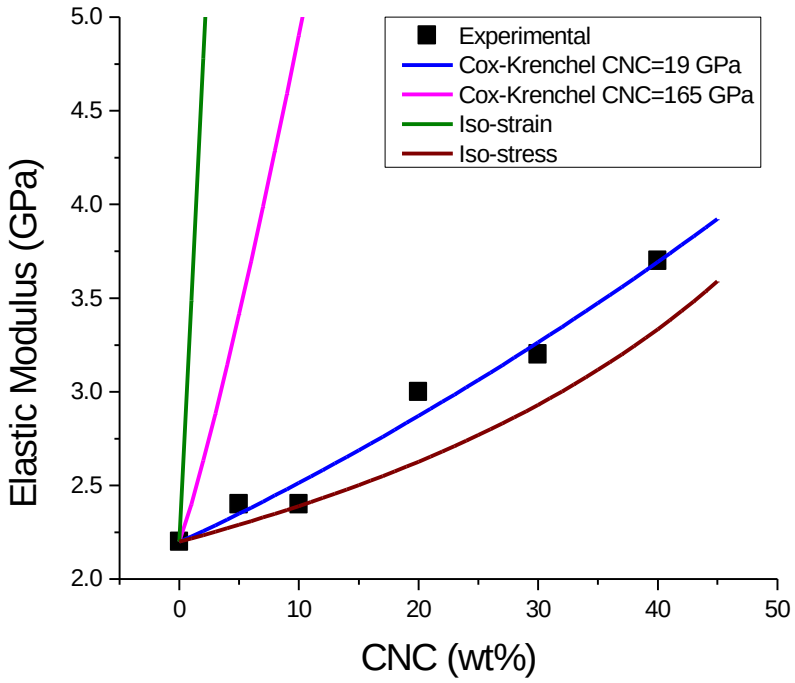

Figure 2.7. Experimental elastic modulus and the Cox-Krenchel Model predictions for varying CNC elastic moduli. Also the predicted isostrain and isostress curves, with a CNC elastic modulus of 165 GPa.

2.3 Conclusion

The addition of CNCs to PAN-co-MAA was shown to alter the suspension rheology, and the thermal-mechanical properties of the corresponding composites. A solution of PAN-co-MAA and suspensions of PAN-co-MAA/CNCs were made with a solid content of ≈4 wt%, with CNC loadings as high as 40 wt% of the solid content. The addition of CNCs leads to suspensions with higher viscosities at low shear rates, and a shear thinning behavior was observed in the composite suspensions, while a relatively Newtonian behavior was noted for the neat PAN-co-MAA solution. Additionally, an aging effect was observed for all the PAN-co-MAA/CNC suspensions with the viscosities increasing over time, and is believed to result from time dependent polymer adsorption onto the CNCs. Neat PAN-co-MAA and PAN-co-MAA/CNC films with up to 40 wt% CNC loadings were produced by solution casting. These composite films maintained a similar level of transparency as the neat PAN-co-MAA film. The Tg increased from 92 °C for the neat polymer to 118 °C at 30 wt% CNC loading. Thermal stability of PAN-co-MAA/CNC composite films were greater than both the neat PAN-co-MAA and neat CNC for temperatures under 350 °C in both air and nitrogen. Additionally, the residue yield of the composites were higher than predicted from rule-of-mixtures. These thermal results indicate chemical interaction between the PAN-co-MAA and CNCs when heated. FTIR results show an interaction between the CNCs and the carbonyl group of the MAA copolymerized with the PAN. The addition of CNCs did not change the degree of PAN-co-MAA crystallinity. There was a trend of increasing elastic modulus and increasing tensile strength with increasing CNC loading. Comparing the neat PAN-co-MAA to the 40

wt% CNC loaded film, the elastic modulus increased from 2.2 to 3.7 GPa, the tensile strength increased from 75 to 132 MPa, while the strain a break decreased from 27.3 to 4.2 %. The storage modulus of PAN-co-MAA increased from 3.9 to 10.5 GPa at 40 wt% CNC loading at 35 °C. The interfacial shear strength between the PAN-co-MAA and CNC was estimated to be 27 MPa, which is lower than the critical interfacial strength needed to fully utilize the tensile strength of the CNC.

CHAPTER 3. CELLULOSE NANOCRYSTALS EFFECT ON THE STABALIZATION OF POLYACRYLONITRILE COMPOSITE FILMS

3.1 Introduction

Polyacrylonitrile (PAN) is the main precursor for carbon fiber, and stabilization is a processing step that is required during the production of carbon materials. Similarly cellulose is also used to produce carbon material and a stabilization process is also needed to be done as a processing step. This stabilization is typically done in heated furnaces, and this is a very energy intensive process. Adding in fillers that could reduce the energy needed for stabilization can have a significant effect on reducing the cost of producing carbon materials. The addition of CNC on PAN film stabilization kinetics will be investigated. The structural development of the PAN-CNC film during the heat treatment process will also be studied.

3.2 Experimental

3.2.1 Materials

The materials that were used are described in **Section 2.2.1** in addition to those materials ACS grade methanol was obtained from VWR and used as is.

3.2.2 Film and Fiber Preparation

Film preparation was described in **Section 2.1.3** except the solvent used to disperse the CNCs used to make the neat CNC film was DMF in this chapter. The neat PAN-co-MAA fiber was also made by a previously described process [41]. First 15 grams of PAN-co-MAA was dissolved in 100 mL of DMF at 80 °C and stirred at 200 rpm for 3 to 4 hours.

The fiber was spun with a spinning unit with a 200 μm diameter spinneret (Hills Inc.). The solution was gel spun by spinning into -50 °C methanol with an air gap of ~5 cm, and the as spun draw ratio (ADR) was 3x. Afterwards the fiber was the kept at -50 °C in methanol for 1 day. The fiber was subsequently cold drawn at room temperature followed by hot drawing in a glycerol bath (165 °C). The total draw ratio (TDR) of the fiber was 15x with a diameter of ~15 μm.

3.2.3 Characterization

DSC was ran on TA instrument Q100. Sample sizes of 2 to 3 mg were used in standard aluminum pans. Samples were heated from 50 to 400 °C at a heating rate of 5, 10, 15, and 20 °C/min in nitrogen and then rerun in air. Samples were also ran directly in air at a heating rate of 10 °C/min. Weight change with temperature change was investigated using TGA with an TA instruments Q500. Samples were heated from 50 to 400 °C at a heating rate of 5 °C/min in nitrogen then rerun in air. Fourier transform infrared spectroscopy (FTIR) was performed on a Spectrum One spectrometer (PerkinElmer Inc). The tests were done by grinding films with KBr and pressing a pellet. The scan range was 700 to 4000 cm^{-1} with resolution of 4 cm^{-1}. Wide-angle x-ray diffraction (WAXD) experiments were completed on a Rigaku MicroMax-002 (CuK_{α}, λ=0.1542 nm) equipped with a Rigaku R-axis IV++ detector. MDI Jade 9 software was used to analyze the WAXD pattern. FTIR and WAXD were performed on neat PAN-co-MAA, neat CNC, and CNC-40 before heating and after heating the samples to different temperature under different environments. Unless specifically mentioned all experiments were done on cast films with

~100 μm thickness. (See Appendix B for a more in depth discussion on the DSC testing procedure and why it was ran this way)

3.3 Results and Discussion

3.3.1 Effect of Sample Geometry on Stabilization

To determine if geometry had an effect on the stabilization reaction, neat PAN-co-MAA fibers (15 μm diameter) and films (13 μm or ~100 μm thick) were tested in DSC. Initial heating runs in nitrogen showed that the magnitude of the cyclization peak between the fiber and films were similar (**Figure 3.1a**). In contrast, when the samples were rerun in air after nitrogen, there was a significant difference on the magnitude of the exothermic reaction that was based on sample geometry (**Figure 3.1b**). The fibers had an exothermic reaction about 4 times the magnitude of the 93 μm thick films and 2 times the magnitude of the 13 μm thick films. This effect of sample geometry on the reaction is believed to result from the rate of oxygen diffusion through the sample, which is dependent on the surface to volume ratio (SA:V). The PAN-co-MAA fibers have about 12 times the SA:V of the 93 μm film, and about 1.7 times the SA:V of the 13 μm film based on the geometry (see supporting information for calculations). The low magnitude of the exothermic reactions for the ~100 μm thick films made it difficult to determine the peak temperature of crosslinking, which can typically be determined on fibers [85, 87]. Note that the ~100 μm thick films were used for the rest of the study, and thus the crosslinking temperatures were not determined. The effect of sample geometry can also be seen in the TGA curves (**Figure 3.2**). It was previously reported that weight gain can be observed in neat PAN fiber due to oxidation if the sample was first ran in nitrogen followed by air [85]. In the current

study, this was also observed, where for the PAN-co-MAA fiber TGA run in air after nitrogen there was an increase in weight of the neat PAN-co-MAA. The effect of sample geometry on weight gain was present, in which the fiber reached a max of 105% weight percent, the 13 µm thick film reached a max of 101% weight percent, while the 93 µm thick film did not experience an increase in weight throughout the run. Even though the 93 µm thick film showed no apparent weight gain, oxidation to some degree likely occurred, though at a lower extent compared to the samples with higher specific surface area, and it is considered here that the mass gained by oxygen pick-up was offset by mass loss due to other reactions.

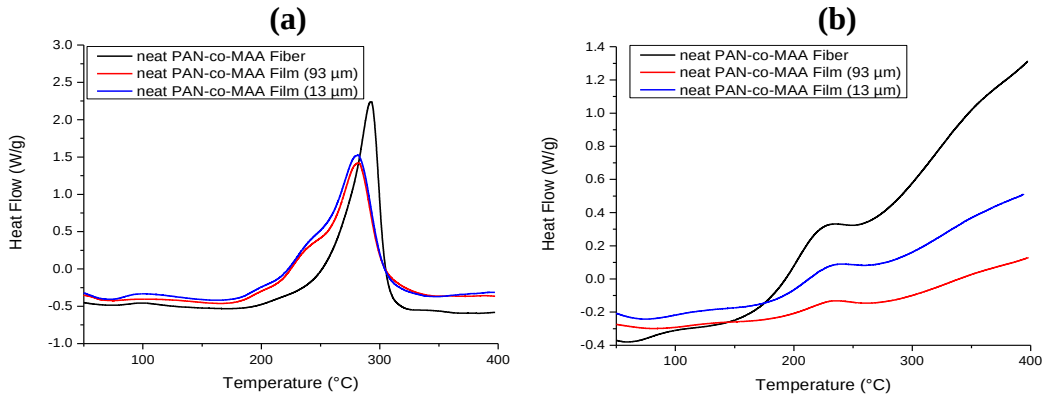

Figure 3.1. DSC curves comparing neat PAN-co-MAA fiber vs film at a heating rate of 10 °C/min. **(a)** in nitrogen **(b)** in air after being run in nitrogen.

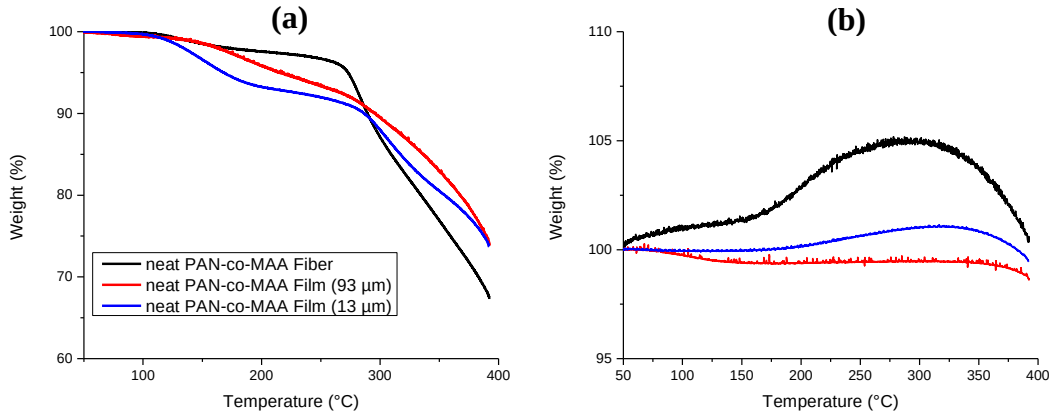

Figure 3.2. TGA curves at a heating rate of 5 °C/min to show differences showing differences between film and fibers, and influence of thickness on films. **(a)** in nitrogen **(b)** in air after run in nitrogen.

3.3.2 Effect of CNC Addition on Oxygen Permeability

It has been hypothesized that the low permeability of oxygen for PAN ($3*10^{-4}$ to $6*10^{-3}$ barrer) is a contributing factor to the skin-core morphology that exists in stabilized and carbonized fiber [127-130]. If the oxygen permeability of CNCs or the CNC/PAN interface is higher than PAN, then the addition of CNCs could help provide a fast pathway for oxygen to travel within PAN, particularly if there is a percolated CNC network. This would lead to a more homogenous stabilization of the PAN, and could help prevent the skin-core morphology from forming, and possibly reduce the stabilization time. The range of reported permeability of CNC films is between $6.3*10^{-4}$ to 140.7 barrer [131, 132]. Partial support for CNCs having higher oxygen permeability than PAN-co-MAA was found in the TGA runs, where weight gain was observed in air rerun for the CNC film, but not the PAN-co-MAA and CNC-40 films (**Figure 3.3**). The diffusion of oxygen through the PAN-co-MAA on the surface in the CNC-40 sample is likely limiting the oxygen to

the sample, which is why we do not see weight gain. Though we do not see weight gain, a more homogenous stabilization should still occur in the composite samples because of the CNC network for oxygen diffusion into the film.

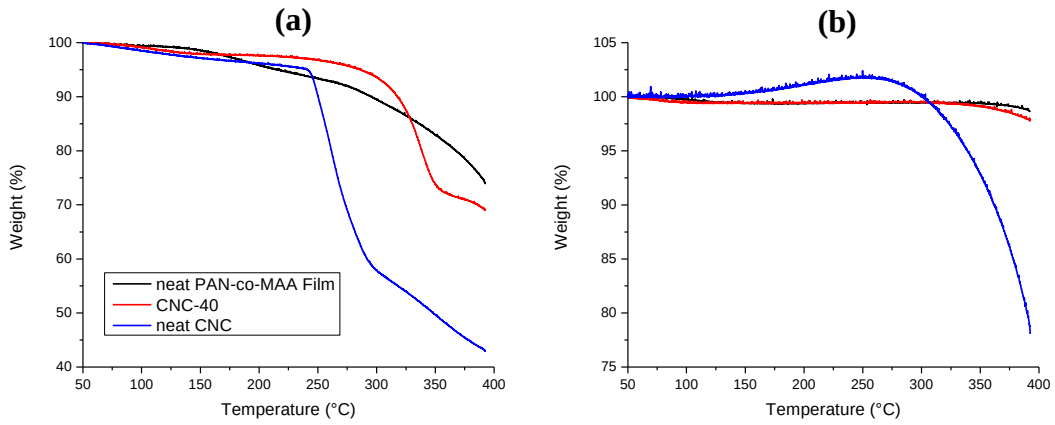

Figure 3.3. TGA curves of films at a heating rate of 5 °C/min to show differences neat PAN-co-MAA, neat CNC, and CNC-40. **(a)** in nitrogen **(b)** in air after run in nitrogen.

3.3.3 Effect of CNC Addition on PAN cyclization

The results of the DSC measurement in nitrogen for neat PAN-co-MAA, neat CNC, and PAN-co-MAA/CNC composite films are summarized in **Table 3.1**, while **Figure 3.4** shows DSC plots of the sample ran in different environments at a heating rate of 10 °C/min. As reported in the literature at this heating rate the cyclization reaction of PAN has an exothermic peak around ~ 275 °C, which is similar to what was measured for the PAN-co-MAA used in this study for the various heating rates. In contrast, CNCs have an endothermic peak at ~275°C that is related to dehydration and thermal scission of the of bridge oxygen [96, 133]. For cellulose, it has been reported that smaller particles and more compressed samples (e.g., more contact between cellulose) leads to lower thermal stability, [134, 135]. In the current study, neat CNC materials tested in DSC (heating rate of 10

°C/min) had a different curve shape, enthalpy of the endothermic reaction, and over 35 °C difference for the onset of dehydration, depending on how the CNC was prepared (e.g., solvent used to cast film, if the film was ground to a powder, or as received freeze dried CNC powder) (**Figure B.1** and **Table B.1**). The CNC samples with higher surface area (e.g., ground films and freeze dried CNC powders) had higher thermal stability and enthalpy of reaction. Freeze dried CNCs were the most thermally stable, but freeze dried CNCs are still heavily aggregated at the micron scale as seen in previous studies [41, 134]. For the PAN-co-MAA/CNC composite films, the dispersion of CNCs was fairly good in that very little micron sized agglomerations were observed in **Chapter 2**, which should result in higher thermal stability of the CNCs. For consistency in measurement, the rest of the paper only as casted CNC film (from the CNC-DMF suspension) samples were tested.

In general, the cyclization peak temperatures increased with increasing CNC loading at all heating rates (**Table 3.1**). However, for the CNC-5 and CNC-10 films there was either no change or a decrease in peak temperature compared to the neat PAN-co-MAA at heating rates of 15 °C/min and lower. It has been previously reported by Liu et al. [85] that the addition of 1 wt% CNT into PAN also exhibited an increase in cyclization peak temperature. Additionally, Mathur et al. [136] reported that the DSC run of PAN fibers in air exhibited a higher onset and peak temperature for cyclization than when the sample was run in nitrogen. The presence of oxygen in CNC may be a contributing factor to the increased higher onset and peak temperature for cyclization. The shape of the cyclization curves were very similar between neat PAN-co-MAA and the PAN-co-MAA/CNC composites with minimal changes with increasing CNC loading. The lack of

change in curve shape indicates that the dehydration reaction of the CNC may not have occurred during PAN cyclization, which is supported by FTIR and WAXD.

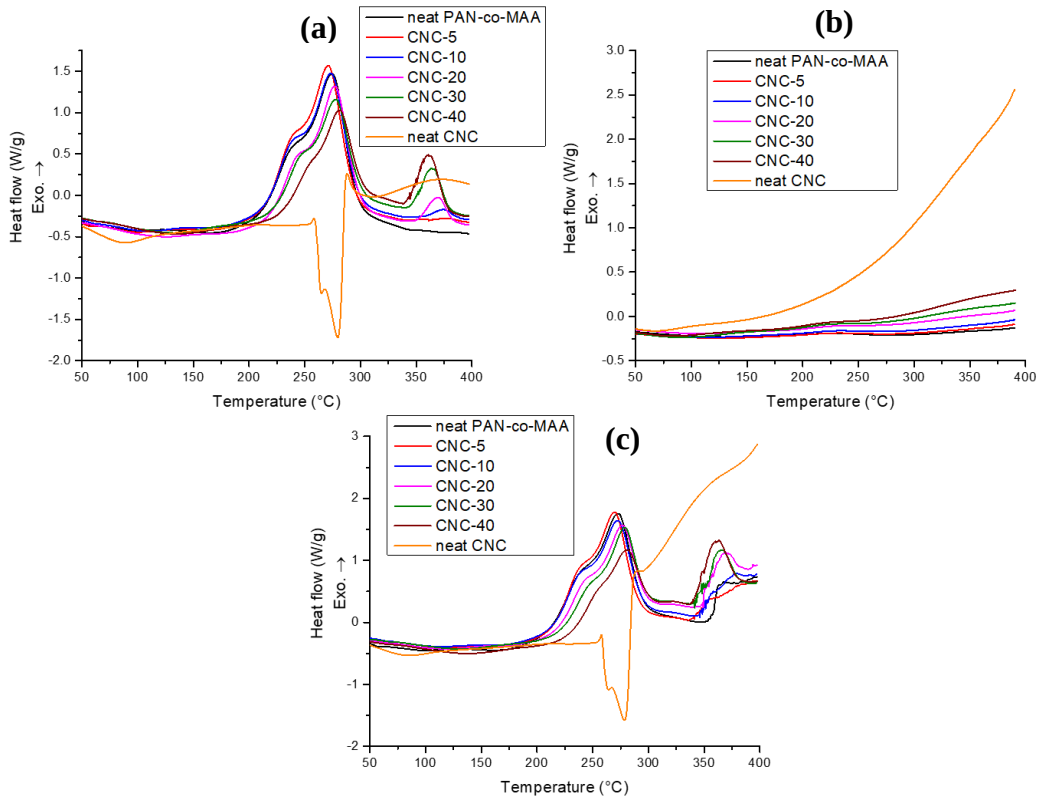

Figure 3.4. DSC runs of the film samples at a heating rate of 10 °C /min in **(a)** nitrogen, **(b)** rerun in air after nitrogen, and **(c)** directly in air.

3.3.4 Increased Thermal Stability of Cellulose Nanocrystal in Polyacrylonitrile

Both FTIR and WAXD results indicate that chemical and structural breakdown of the CNC was shifted to higher temperatures for the PAN-co-MAA/CNC composites as compared to neat CNC. For neat CNC films the FTIR spectra (**Figure 3.5b**) show that after heating the CNC film to 310 °C, peaks associated with cellulose at 341 (COC in pyranose ring), 1113 (ring stretch), 1061 (CO or COH on ring or bridge oxygen stretch), and 1033

cm^{-1} (CO) started to lose their sharpness and started to merge [137, 138]. Likewise, WAXD patterns (**Figure 3.6**) show the disappearance of the peaks associated with cellulose II (2θ=20.4°) and cellulose I (2θ= 22.6°), indicating structural breakdown of the cellulose [107, 134, 139, 140]. In contrast, for the CNC-40 composite heated to 310 °C, the FTIR spectra maintain distinct peaks at 1161, 1113, 1061, and 1033 cm^{-1}, and the WAXD retain the peaks associated with cellulose I and II, supporting the conclusion that dehydration and depolymerization of CNC had not occurred. It is considered here that having a fine CNC dispersion within PAN-co-MAA, which was previously seen in **Chapter 2** could be one mechanism in retarding the dehydration and depolymerization reactions of the CNCs.

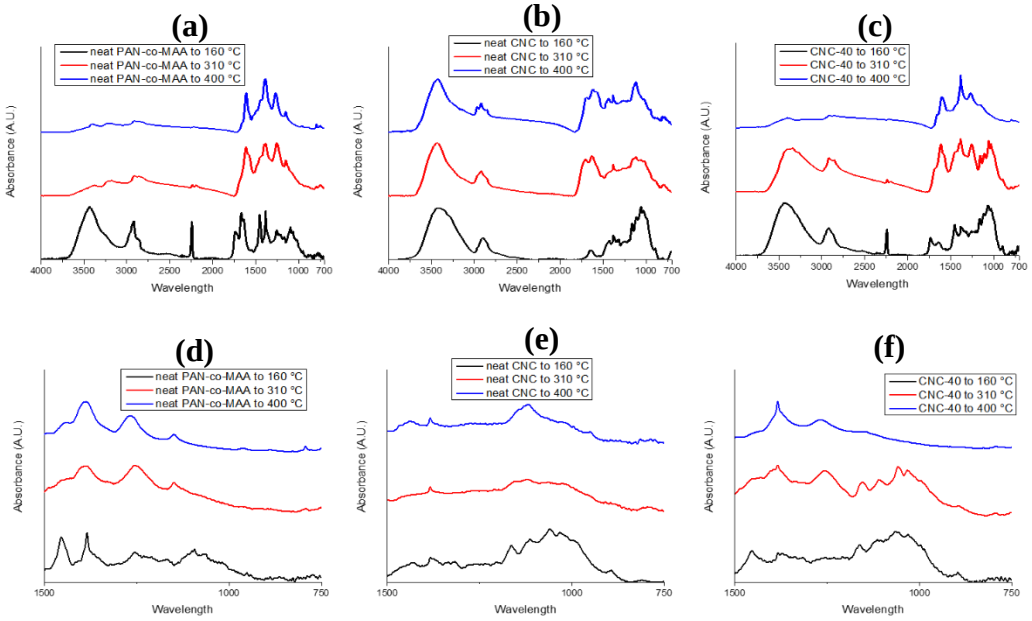

Figure 3.5. FTIR plots of **(a)** neat PAN-co-MAA, **(b)** neat CNC, and **(c)** CNC-40 from 4000 to 650 cm^{-1}, and **(d)** neat PAN-co-MAA, **(e)** neat CNC, and **(f)** CNC-40 from 1500 to 750 cm^{-1} after being heated at 10 °C/min in nitrogen.

Table 3.1. Summary of the onset and peak temperatures in the film DSC runs in nitrogen.

Sample	neat PAN-co-MAA	CNC-5	CNC-10	CNC-20	CNC-30	CNC-40	neat CNC
Onset of cyclization temperature @ 5 °C/min (°C)	196	199	200	204	207	218	N/A
Onset of cyclization temperature @ 10 °C/min (°C)	208	212	211	217	221	228	N/A
Onset of cyclization temperature @ 15 °C/min (°C)	213	218	219	224	229	237	N/A
Onset of cyclization temperature @ 20 °C/min (°C)	222	224	224	229	235	242	N/A
Cyclization peak temperature @ 5°C/min (°C)	265	262	262	267	268	270	N/A
Cyclization peak temperature @ 10°C/min (°C)	275	271	274	278	278	282	N/A
Cyclization peak temperature @ 15°C/min (°C)	280	279	280	284	285	288	N/A
Cyclization peak temperature @ 20°C/min (°C)	284	284	285	289	290	293	N/A
2nd exothermic peak temperature @ 5°C/min (°C)	N/A	N/A	N/A	356	352	349	361
2nd exothermic peak temperature @ 10°C/min (°C)	N/A	N/A	N/A	370	364	361	372
2nd exothermic peak temperature @ 15°C/min (°C)	N/A	N/A	N/A	378	373	370	380
2nd exothermic peak temperature @ 20°C/min (°C)	N/A	N/A	N/A	386	380	375	387

3.3.5 Effect of CNC Additions on Cyclization Activation Energy and Reaction Rates

The average enthalpy of reaction during cyclization over the four heating rates can be found in **Table 3.2**. The composite samples' enthalpy of cyclization is similar to the weight fraction of PAN-co-MAA it is composed of, though the values calculated by PAN-co-MAA weight fraction are still slightly higher than the experimental values. This discrepancy between the calculated and experimental value is likely due to heat released during cyclization is being absorbed by the CNC in the composite. Using the cyclization peak temperature at different heating rates, the activation energy of cyclization (**Figure 3.7a** and **Table 3.3**) can be calculated with Kissinger's equation (**Equation 3.1**) [141] where E_a, R, ϕ, and T_p are activation energy (kJ/mol), universal gas constant (8.314 J/(mol*K)), heating rate (K/min), and reaction peak temperature (K), respectively. It was found that the activation energy decreased in all composite samples to a consistent value of ~147 kJ/mol (~16 % decrease) compared to the neat PAN-co-MAA sample value of 175 kJ/mol. Using the activation energy the reaction rate constant (k) can be calculated with **Equation 3.2**, while the pre-exponential factor, A , can be determined from **Equation 3.3**, where T is the temperature (K) at which the reaction rate is being solved [87, 142]. The temperature has large effect on the reaction rate constant, so the reaction rate constant was solved for a heating rate of 10 °C/min at 200, 250, and 300 °C. These temperatures were chosen because PAN is often stabilized between 200-300 °C [4, 99, 143].

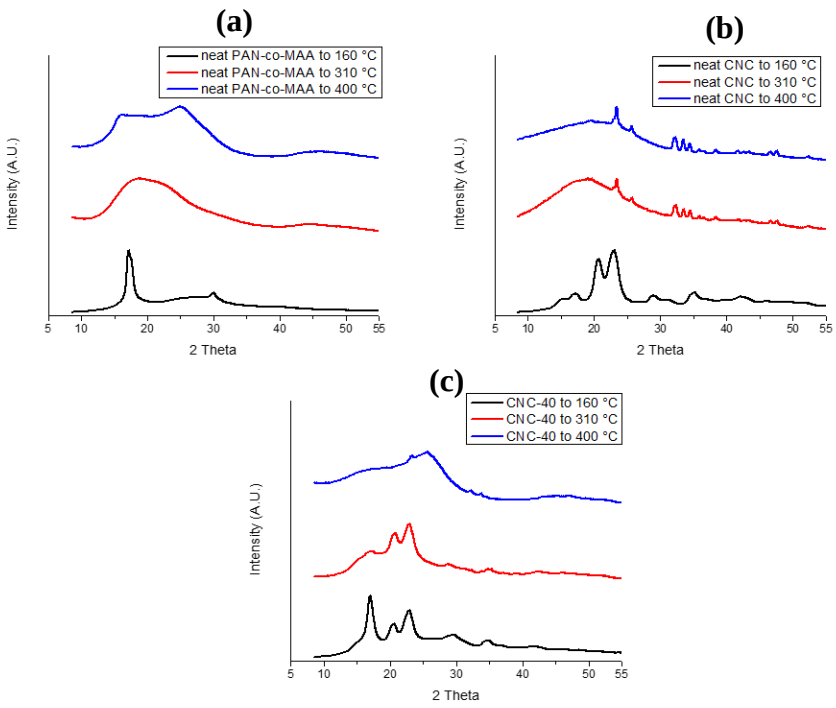

Figure 3.6. WAXD plots of **(a)** neat PAN-co-MAA, **(b)** neat CNC, and **(c)** CNC-40 after being heated at 10 °C/min in nitrogen.

$$-\frac{E_a}{R} = \frac{d(\ln \frac{\phi}{T_p^2})}{d(\frac{1}{T_p})} \quad \textbf{(3.1)}$$

$$k = Ae^{-E_a/RT} \quad \textbf{(3.2)}$$

$$A = \frac{\phi E_a e^{E_a/RT_p}}{RT_p^2} \quad \textbf{(3.3)}$$

Table 3.2. Experimentally measured and the rule of mixtures estimate of enthalpy of cyclization, which shows similar values indicating CNC is not reacting at this temperature.

Sample	neat PAN-co-MAA	CNC-5	CNC-10	CNC-20	CNC-30	CNC-40
Experimental average enthalpy of cyclization (J/g)[a]	648	607	569	494	412	344
Theoretical enthalpy of cyclization as function of PAN-co-MAA weight percent (J/g)	648	615	583	518	453	389

[a] Average of the runs ran at a heating rate of 5, 10, 15, and 20 °C/min.

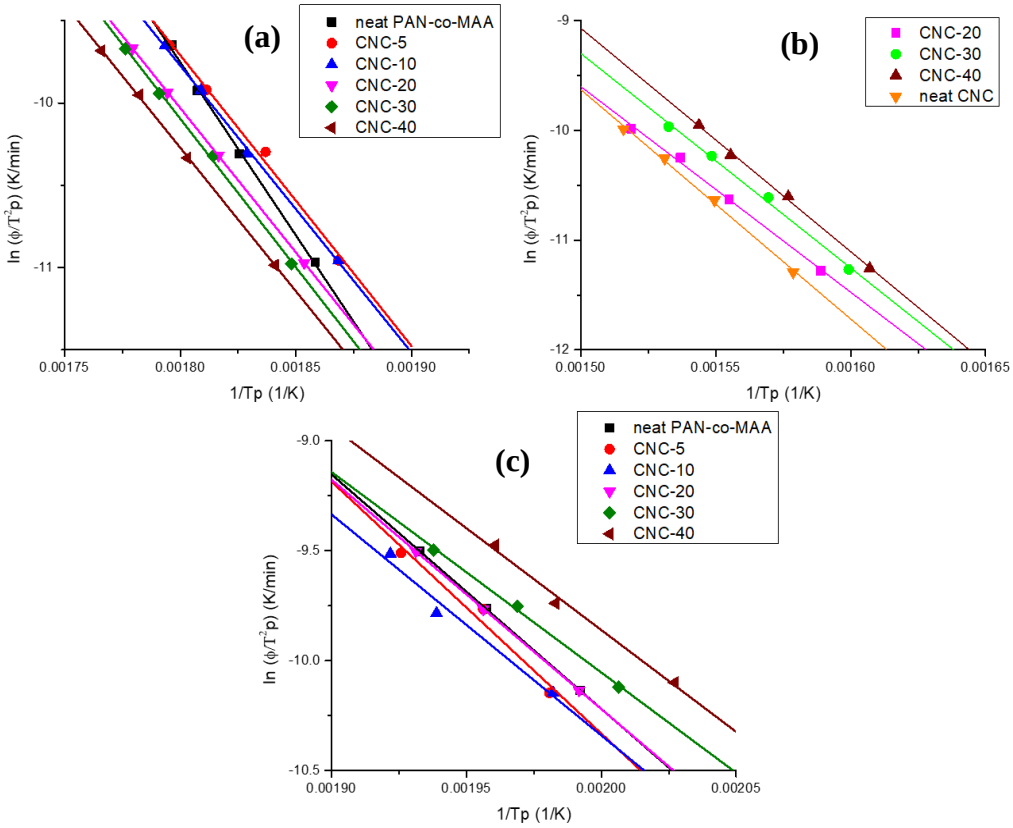

Figure 3.7. Graphs used to calculate the activation energy of the **(a)** cyclization of film samples in nitrogen atmosphere, **(b)** 2nd exothermic reaction in the film samples in nitrogen atmosphere, and **(c)** oxidation of film samples re-run in air after being run initially in nitrogen.

As summarized in **Table 3.3**, the cyclization reaction rate constant for both the neat PAN-co-MAA and the composites increases with increasing T. For the composites samples, increasing CNC loading results in a lower reaction rate constant, the extent of which was dependent on T. Interestingly, the effect of CNC addition on the cyclization reaction rate constant with respect to the neat PAN-co-MAA was dependent on T. For example, at 200 °C all composite samples had a higher reaction rate constant than neat PAN-co-MAA, while at 300 °C the opposite was true with neat PAN-co-MAA having the highest reaction rate constant.

3.3.6 Development of a 2nd Exothermic Peak in Composite Samples

A 2nd exothermic peak in DSC developed in the PAN-co-MAA/CNC composite samples above 300 °C in nitrogen (**Figure 3.4**), which did not occur in the neat PAN-co-MAA samples. The activation energy of this 2nd exothermic peak (**Figure 3.7b** and **Table 3.3**) was calculated for CNC-20 and higher CNC loaded samples. At the lower CNC loadings the curves were not perfectly smooth making it difficult to determine the peak temperature. There was a trend of increasing activation energy with increasing CNC loading, with the neat CNC sample having the highest activation energy of 174 kJ/mol.

Table 3.3. Activation energy, pre-exponential factor (A), and reaction rate constant (k) for cyclization, 2nd exothermic peak, and oxidation, calculated from DSC measurements at different heating rates using Kissinger's method. The results of the cyclization and 2nd exothermic peak were from experiments conducted in nitrogen, while the oxidation results were done in air after first running the sample in nitrogen

Sample	neat PAN-co-MAA	CNC-5	CNC-10	CNC-20	CNC-30	CNC-40	neat CNC
Activation Energy of Cyclization (kJ/mol)	175	147	145	146	150	145	N/A
A for cyclization (s^{-1})	3.3×10^{16}	7.4×10^{13}	4.0×10^{13}	4.0×10^{13}	1.0×10^{14}	2.5×10^{13}	N/A
k of cyclization @ 200 °C (s^{-1})	0.0016	0.0044	0.0040	0.0031	0.0026	0.0025	N/A
k of cyclization @ 250 °C (s^{-1})	0.11	0.17	0.14	0.11	0.10	0.09	N/A
k of cyclization @ 300 °C (s^{-1})	3.8	3.0	2.5	2.0	2.1	1.6	N/A
Activation Energy of 2nd exothermic peak (kJ/mol)	N/A	N/A	N/A	156	162	169	174
Activation Energy of Oxidation (kJ/mol)	89	95	84	87	76	77	N/A
A for oxidation (s^{-1})	7.0×10^{8}	3.2×10^{9}	1.8×10^{8}	4.4×10^{8}	3.3×10^{7}	5.4×10^{7}	N/A
k of oxidation @ 200 °C (s^{-1})	0.12	0.10	0.11	0.12	0.14	0.17	N/A
k of oxidation @ 250 °C (s^{-1})	0.99	0.99	0.80	0.95	0.87	1.10	N/A
k of oxidation @ 300 °C (s^{-1})	5.87	6.67	4.27	5.42	3.98	5.18	N/A

The formation of this 2nd exothermic peak is considered to result from; i) CNC reactions interactions, ii) PAN-co-MAA/CNC interactions, or iii) a combination of these two reactions occurring simultaneously. This exothermic reaction in neat CNCs is associated with a mixture of dehydration, decarbonylation, decarboxylation, and the formation of levoglucosan, which forms gaseous products like CO, CO_2, CH_4, and H_2O [96, 144]. For the composite samples the exothermic peak was sharper than in the neat CNC sample, and shifts to lower temperatures with increasing CNC loading, where at 40 wt% CNC loading the shift was ~10 °C lower than for the neat CNCs. Since there were no dehydration or depolymerization reactions observed at lower temperatures, it is possible that there is either a change in the reaction kinetics of cellulose or a different set of reactions are occurring in the cellulose.

The 2nd exothermic peak could also be due to reactions between PAN-co-MAA and CNC, four proposed reactions are given in **Figure 3.8**. The proposed reactions are based on the degradation pathway of cellulose and the oxidation pathways of PAN, because according to our experiments cellulose has not undergone depolymerization and PAN has not undergone oxidation before this exothermic peak. In support of reactions between PAN-co-MAA and CNC, the TGA data (**Figure 3.3** and **Table 3.4**) shows that the experimental yield of CNC-40 is higher than the rule of mixture yield of the PAN-co-MAA and CNCs after heating to 400 °C. One of the ways CNCs could interact with PAN-co-MAA is by supplying oxygen needed for reactions. As a result of depolymerization of CNCs, oxygen could be made available that would promote a reaction with PAN-co-MAA. In partial support for this, DSC results of the neat PAN-co-MAA ran directly in air (**Figure**

3.4) show an exothermic reaction that occurs after cyclization while in nitrogen this does not occur.

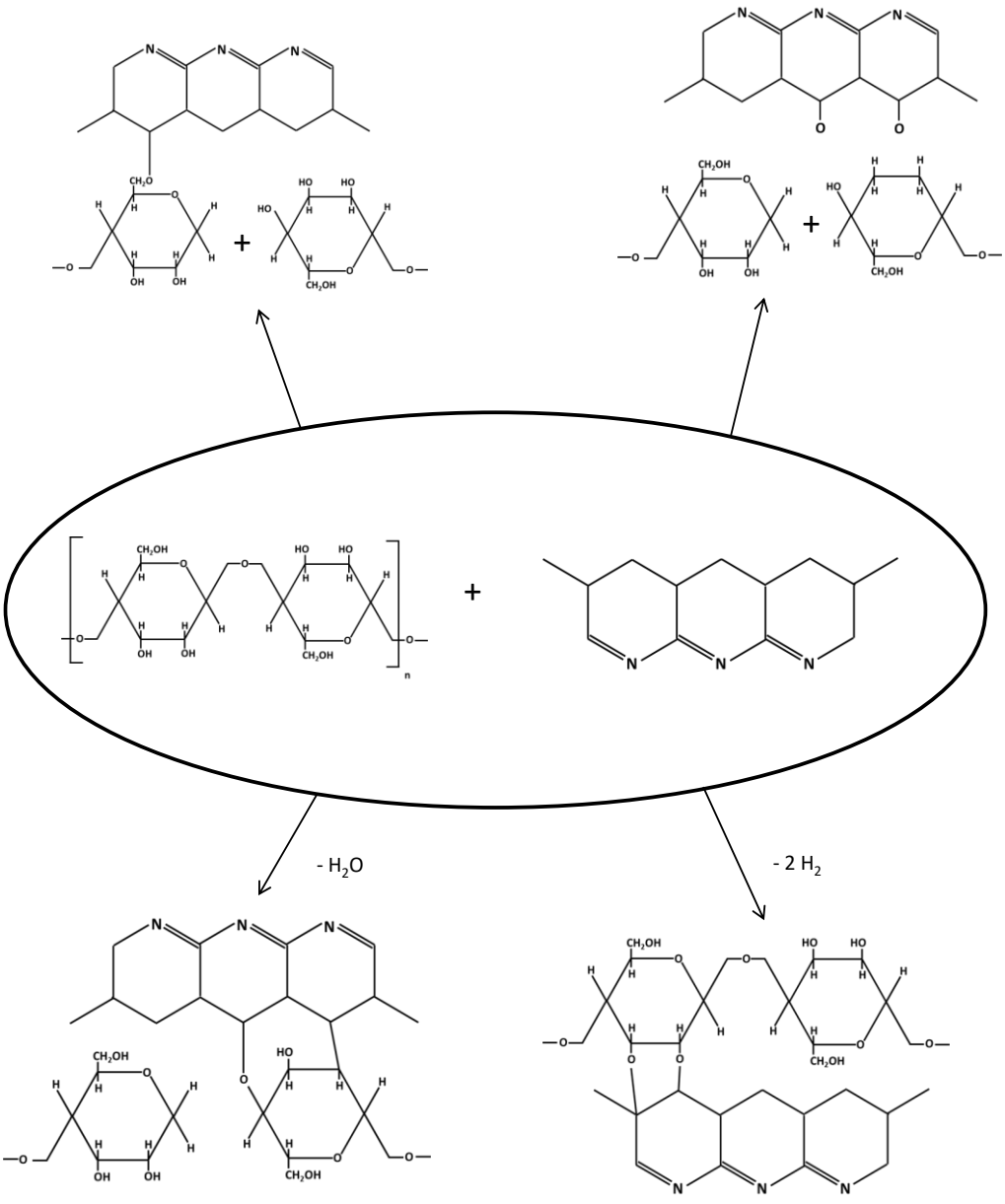

Figure 3.8. Proposed possible chemical reactions between PAN and cellulose during stabilization.

Table 3.4. Yield of the films after running the samples in the TGA at 5 °C/min to 400 °C.

Sample	neat PAN-co-MAA	CNC-40	neat CNC
Experimental yield after run in Nitrogen (wt%)	74	69	43
Experimental yield after rerun in Air (wt%)	99	98	78
Rule of Mixture yield after run in Nitrogen (wt%)	N/A	62	N/A
Rule of Mixture yield after rerun in Air (wt%)	N/A	91	N/A

3.3.7 Effect of CNC Additions on Oxidation Activation Energy and Reaction Rates

DSC of films ran in nitrogen and then re-ran in air (**Figure 3.4**) show a larger exothermic reaction for neat CNC films than for neat PAN-co-MAA films. The CNCs reaction with oxygen could be more exothermic than PAN or it is possible that the pure CNC films used in the study had a higher surface area due to surface roughness and/or porosity. It has previously been reported that casted CNC films are typically not fully dense [33]. This leads to an increase in the oxygen diffusion rate thus leading to the much higher exothermic reaction. Similarly to when PAN fibers are rerun in air the exothermic reaction was much higher than the PAN films, presumably due to the large surface area to volume ratio in the fibers leading to higher oxygen diffusion rates (**Figure 3.3**). The DSC curves of the composite films do not follow the rule of mixture, being much less exothermic than expected. This could be a result of the composite films having much less porosity than the pure CNC films, or that PAN-co-MAA having lower oxygen permeability than CNC, making the oxygen diffusing through the PAN-co-MAA the limiting factor for the CNC reaction. The FTIR and WAXD of the samples can be found in **Figure B.2** and **B.3**.

The activation energy of oxidation (**Figure 3.7c** and **Table 3.3**) was calculated with Kissinger's equation (**Equation 3.1**), using the oxidation peak temperature at different heating rates (**Table 3.5**). At low CNC loadings (5 and 10 wt%) the oxidation peak temperature increases compared to neat PAN-co-MAA, while at higher CNC loadings the peak temperature decreases. It is considered here that oxygen in the CNC facilitates the oxidation of PAN, which is more energetically inclined during the first nitrogen run. The decrease in peak temperature at higher CNC loadings is considered to result from a larger presence of oxygen and potentially faster diffusion path along a percolated CNC network within the PAN-co-MAA. Interestingly, Liu et al. [85] reported that at low CNT loadings (1 wt%) the oxidation peak temperature also increased.

As summarized in **Table 3.3**, there was a small effect of CNC additions to PAN-co-MAA on the activation energy of oxidation and on the oxidation reaction rate constants. With increased CNC loadings within the composite samples, there was a weak trend of decreasing activation energy, but the oxidation reaction rate constant showed no consistent trends (at all temperatures). With increasing T, the oxidation reaction rate constant for both the neat PAN-co-MAA and the composites decreases. At certain CNC loadings and temperatures, the oxidation reaction rate constant was higher than neat PAN-co-MAA. It was found that at 200 °C samples CNC-20, CNC-30, and CNC-40 had higher (or the same) reaction rate constant for both cyclization and oxidation than neat PAN-co-MAA. This indicates conditions in which the addition of CNCs into PAN-co-MAA can reduce the energy needed for stabilization.

Table 3.5. Peak temperature of the oxidation reaction measured via DSC of films run in nitrogen and then re-run in air.

Sample	neat PAN-co-MAA	CNC-5	CNC-10	CNC-20	CNC-30	CNC-40
Oxidation peak temperature @ 10 °C/min (°C)	229	232	232	229	225	220
Oxidation peak temperature @ 15 °C/min (°C)	238	238	243	238	235	231
Oxidation peak temperature @ 20 °C/min (°C)	244	246	247	245	243	237

3.4 Conclusions

With the addition of CNCs to PAN-co-MAA there was a 16% reduction in the activation energy of the PAN cyclization reaction, the extent of which did not change with CNC loading. This indicates that CNCs are potentially acting as a catalyst for the cyclization PAN. In contrast, the activation energy of oxidation was minimally affected by CNC addition. At certain CNC loadings and temperatures, the reaction rate constant for both cyclization and oxidation were higher for PAN-co-MAA/CNC composites than for neat PAN-co-MAA, indicating that the addition of CNCs into PAN-co-MAA can reduce the energy needed for stabilization. The PAN-co-MAA onset of cyclization temperature increased with CNC loading. The peak temperature of cyclization, as compared to the neat PAN-co-MAA, was shifted to lower temperatures at low CNC loadings and at low heating rates, while at higher CNC loadings and at higher heating rates it was shifted to higher temperatures. Additionally, CNCs within the PAN-co-MAA/CNC composite were more stable than the neat CNC films. DSC showed that the PAN-co-MAA/CNC composites did

not exhibit the dehydration reaction seen in neat CNC films that occurs at ~275 °C, while FTIR and WAXD showed that the chemical and structural changes of CNCs occurred at higher temperatures. Lastly, the oxidation reaction of PAN-co-MAA was influenced by the surface area to volume ratio of the sample that was tested, while the cyclization reaction was unaffected.

CHAPTER 4. POST-SULFONATION OF CELLULOSE NANOFIBRILS WITH A ONE-STEP REACTION TO IMPROVE DISPERSIBILITY

4.1 Introduction

Dispersibility of nanofillers is very important factor to achieve high properties in nanocomposites. To achieve good dispersibility in the polymer, good dispersibility in the polymer suspension is required, and this in turn requires good dispersibility of the nanofillers in solvent. The surface interaction between the polymer and nanofiller is also very important determining factor of how well the nanofiller reinforces the polymer. In this chapter we developed a sulfonation process for CNFs that mimics the same surface chemistry as CNCs produce by sulfuric acid hydrolysis. This process is faster than other reported sulfonated methods for CNF and the TEMPO oxidation method. We also investigate the change in surface chemistry when the CNF is dispersed in water and DMF to study how the CNF surface chemistry changes during the polymer CNF suspension making process.

4.2 Experimental

4.2.1 Materials

Freeze dried CNF (Lot #U38) produced by mechanical treatment at the Process Development Center, University of Maine, were used in this study. Anhydrous DMF, TEMPO free radical (98%), sodium hypochlorite (NaClO) (14.5% available chlorine in water), sodium hydroxide (NaOH), and hydrochloric acid (HCl) (36 wt%) was obtained from Alfa Aesar. Chlorosulfonic acid (CSA), sodium chloride (NaCl) (99.5%), and DMF

(distilled before use) was obtained from Sigma-Aldrich Corporation. Sodium bromide (NaBr) was obtained from Fisher Scientific. Potassium bromide (KBr) was obtained from Specac Ltd. Dialysis Tubing 14,000 MW cutoff was obtained from Ward's Science.

4.2.2 Sulfonation of Cellulose Nanofibrils

Three different sulfonations were completed with varying moles of CSA to anhydroglucose units (AGU) ratios of 0.5:1, 1.5:1, and 2.5:1, these samples will be referred to as SCNF1, SCNF2, and SCNF3, respectively. For the sulfonation reaction, nitrogen was constantly flowed through the system to prevent water from the air to get into the system. All the glassware was dried in an oven at 110°C overnight to remove all adsorbed water before use. In a three neck flask, 4 g of freeze dried CNFs was added to 400 mL of DMF and left for 30 minutes to let the CNF absorb the DMF. This mixture was then homogenized with an IKA T18 basic Ultra-Turrax for 5 minutes (at a setting of 3.5) followed by another 15 minute soak and 5 minutes of homogenization (at a setting of 3.5). Due to the small amount of CSA being used to increase accuracy a large batch of DMF and CSA was prepared, in which 35 mL of DMF was chilled in an ice bath for 10 minutes before 7 mL of CSA was slowly added into the DMF while undergoing stirring. The desired amount of this CSA/DMF solution was slowly added (~1 minute) to the CNF/DMF mixture while undergoing stirring. For each different CSA to AGU ratio sulfonation experiment 1 batch was made and multiple samples were taken out after 5, 30, and 60 minutes after the CSA/DMF solution was added. For the naming scheme the samples will be referred to as SCNF1-5, SCNF1-30, and SCNF1-60 for the 0.5:1 CSA to AGU ratio samples that reacted for 5, 30, and 60 minutes, respectively, and with the SCNF2 and SCNF3 samples following

the same naming scheme. The reaction was stopped after taking out the sample by adding 1 ml of methanol for every 5 ml of sample taken out. Samples were washed multiple times by centrifugation (15000 x g) with deionized (DI) water until the pH of the supernatant was neutral (pH strips were used) followed by two additional washings. This process was also repeated with a 0:1 CSA to AGU ratio with a sample taken after 60 minutes of stirring to be used as the control sample and will be referred to as unfunctionalized CNF in the rest of the paper. (See Appendix C for discussion on how the procedure for sulfonation was decided and initial difficulties encountered in carrying out this process).

4.2.3 TEMPO Oxidation of Cellulose Nanofibrils

The post TEMPO oxidation on existing CNF was completed with a molar ratio of 2:1 NaClO:AGU. In a three neck flask, 4 g of freeze dried CNF was added to 400 mL of DI water and left for 30 minutes. This mixture was then homogenized with an IKA T18 basic Ultra-Turrax for 5 minutes followed by another 15 minutes soak and another 5 minutes of homogenization with the same settings mentioned above. Then 0.08 g of TEMPO free radical and 0.5 g NaBr was added to the suspension while undergoing stirring with a stir bar and was stirred for 1 hour to make sure the chemicals were dissolved. The pH of the suspension was adjusted to 10.5 by adding 0.5 M NaOH aqueous solution. The pH was monitored with a pH meter UltraBASIC (Denver Instruments). Then 25.7 g of NaClO aqueous solution (14.5 wt%) was added drop wise, after this addition, the pH was monitored and adjusted to stay between 10-10.5 by adding 0.5 M NaOH aqueous solution. Once the pH stabilizes the reaction is finished (~2 hours), and 23.5 g of NaCl was added to flocculate the CNFs. The suspension was then centrifuged (15000 x g) and washed with

1 M NaCl aqueous solution 4 times. The CNF was then protonated by stirring overnight in 1 L of 0.1 M HCl aqueous solution. Afterward the CNF was centrifuged and washed with DI water until the pH of the supernatant was neutral (pH strips were used), followed by two additional washings. CNFs were then put in dialysis bags and dialyzed in a large container with DI water. The water was changed every 2 hours for the first 3 exchanges followed by water exchanges two times a day for 3 days. After this process it was determined that the CNFs was not fully protonated and still contained COO^- groups attributed to the COONa. Consequently, 0.7 g of this CNF was further protonated in in 100 mL of 0.25 M HCl for 24 hours. Then the same cleaning process used before was followed without the dialysis step. Only this fully protonated CNFs will be used for characterization and discussed in this paper and will be referred to as TEMPO CNF.

4.2.4 Dispersion and Film Making Process

The unfunctionalized, sulfonated, and TEMPO CNFs were dispersed in DMF and water to make 0.1 wt% solids suspensions (30 g total weight). These were then homogenized with an IKA T18 basic Ultra-Turrax for 5 minutes (at a setting of 1) followed by another 5 minutes (at a setting of 2) before being sonicated in a bath sonicator (Branson 3510R-MT, 100 W, 42 kHz) for 3 days in a 50 mL polypropylene centrifuge tube. The samples' transparency was measured with ultraviolet-visible spectroscopy (UV-vis) to assess dispersion. The DMF/CNF and water/CNF dispersions were cast in a glass petri dish and put in an oven at 30 °C with airflow to make films. The films were used for wide angle x-ray diffraction (WAXD) and Fourier transform infrared spectroscopy (FTIR).

4.2.5 Characterization

A total of eleven different CNF samples were investigated and characterized in this study, as summarized in **Table 4.1** Scanning electron microcopy (SEM) was completed using a Zeiss Ultra60 FE-SEM, in which samples were dispersed at 0.02 wt% in DMF (approach similar to that outlined above) and then drop casted on a conductive substrate (samples we not coated prior to imaging). Elemental analysis was performed by Atlantic Microlab Inc. to measure the sulfur content. The CNFs were freeze dried followed by vacuum drying before testing. The testing was done using a Carlo Erba 1108 Elemental Analyzer. The samples were weighed, combusted, separated by gas chromatography, and then the sulfur amount was measured by thermal conductivity. The degree of substitution for the sulfonated samples were calculated based on the sulfur content and the equation used can be found in **Appendix C**. The degree of substitution for the TEMPO CNF was determined with conductometric titration and the procedure can be found in **Appendix C** [77].

WAXD was used to assess crystallinity index (CI) changes between the neat and functionalized CNFs. Measurements were completed on a Rigaku MicroMax-002 (CuK_{α}, λ=0.1542 nm) equipped with a Rigaku R-axis IV++ detector, and the data was analyzed with MDI Jade 9 software. The CI of the samples were determined by the peak height method (Segal method) [145, 146], and is calculated with **Equation 4.1**, with I_{002} being the peak height at 2θ=~23°, and I_{am} being the minimum value at 2θ= ~18.5°.

$$Crystallinity\ Index\ (\%) = \left(\frac{I_{002} - I_{am}}{I_{002}}\right) X\ 100 \qquad \textbf{(4.1)}$$

Table 4.1. Summary of characteristics of the unfunctionalized and functionalized CNFs.

Samples	Sulfur Content (wt%)	Degree of Substitution	mmol of sulfate groups/g of cellulose	CI (%)[a]	Zeta Potential (mV)	Transmittance at 600 nm (%)[b]	Transmittance at 600 nm (%)[c]
unfunctionalized CNF	0	0	0	75	-25 ± 2	2	31
TEMPO CNF	0	0.30	0	77	-49 ± 4	17	73
SCNF1-5	1.7	0.09	0.56	73	-39 ± 1	9	60
SCNF1-30	2.3	0.12	0.74	72	-43 ± 2	12	76
SCNF1-60	2.6	0.14	0.86	72	-43 ± 2	13	80
SCNF2-5	2.5	0.14	0.86	69	-45 ± 2	9	67
SCNF2-30	3.9	0.22	1.36	65	-47 ± 2	28	75
SCNF2-60	4.5	0.26	1.60	59	-43 ±2	29	82
SCNF3-5	3.7	0.21	1.30	70	-40 ± 2	12	69
SCNF3-30	4.3	0.24	1.48	57	-44 ± 1	34	78
SCNF3-60	5.0	0.29	1.79	53	-48 ± 1	36	82

[a] Crystallinity index
[b] CNF dispersed in DI water (0.1 wt%)
[c] CNF dispersed in DMF (0.1 wt%)

FTIR was completed on a Spectrum One (PerkinElmer, Inc.) to observe if there were any differences between the unfunctionalized, sulfonated, and TEMPO CNF. FTIR was done in transmission mode with pellets of KBr and the cast films. To make the pellets for FTIR, KBr and the cast films were ground into a powder and then pressed into a pellet using a KBr pellet die from International Crystal Laboratories. The scan range was 750 cm^{-1} to 2000 cm^{-1} with a resolution of 4 cm^{-1} with 128 scans. Zeta potential was completed on a ZEN 3690 (Malvern Instruments) with 0.005 wt% samples in 0.5 mM NaCl aqueous solutions. UV-Vis was used to determine the quality of dispersion of the CNF. The measurements were completed on a Lambda 35 (PerkinElmer Co.) with quartz cuvettes with a scan speed of 480 nm/min with a resolution of 1 nm over a range of 400 to 700 nm.

4.3 Results and Discussion

4.3.1 Change in morphology

The morphology of the unfunctionalized CNF, TEMPO CNF, and SCNF3-60 are shown in **Figure 4.1**, and SEM images of all samples can be found in **Appendix C** (**Figure C.1**). Unfunctionalized CNF have a fibril-like morphology with high aspect ratio, and form a dense network structure. The TEMPO CNF also has a fibril-like morphology with a lower aspect ratio, and was well dispersed on the imaging substrate. For the sulfonated CNF, all reaction times at all CSA to AGU reaction ratios show differences in the overall particle morphology (e.g. shorter, thinner diameter, less bundled) and network formation, but in general still retain a fibril-like morphology. In contrast, previous work on sulfonation of cellulosic material was usually done to make highly soluble cellulose sulfate that did not retain their morphology [147-149]. Though there have been some studies that show

sulfonated cellulosic materials retaining a fiber morphology, these cases used large starting diameter materials like cotton pulp with short reaction times, and the functionalized fibers typically have large diameters (>20 μm) [150]. In contrast, by using CNF as a starting material our sulfonated CNF had a less than 100 nm, and retained their fibril-like morphology with no observable agglomeration.

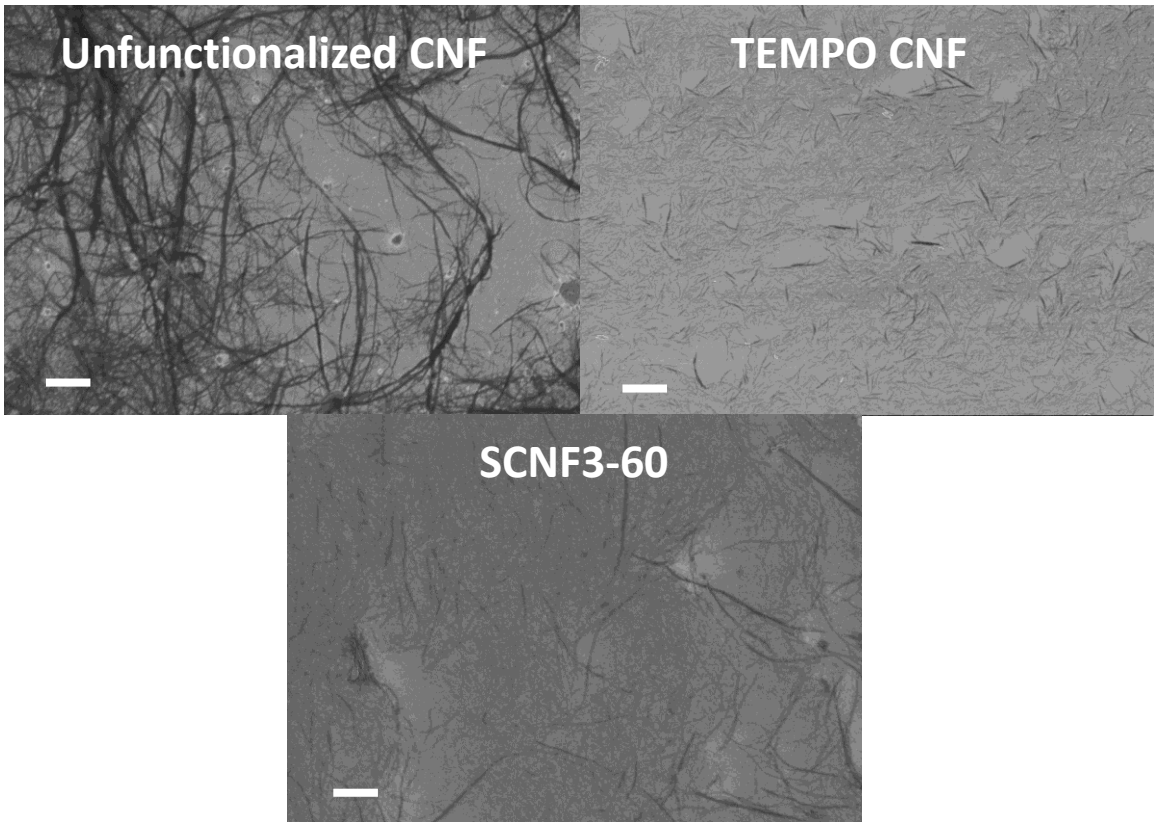

Figure 4.1. SEM images of the unfunctionalized CNF, TEMPO CNF, and SCNF3-60 showing that SCNF3-60 still retain fibril-like morphology. The TEMPO CNF exhibits a shorter length than the unfunctionalized CNF and SCNF3-60. Scale bar is 2 μm.

4.3.2 Elemental Analysis and FTIR

Elemental analysis confirmed there was no sulfur in the unfunctionalized CNF and TEMPO CNF, which was expected (**Table 4.1**). With increasing reaction time the sulfur

content increases in the sulfonated samples at the same CSA to AGU ratio. The higher the CSA to AGU ratio used resulted in a higher sulfur content for the same reaction time. The SCNF2-60 sample had 4.5 wt% sulfur and the SCNF3-60 had 5 wt%, suggesting a leveling off of functionalization while maintaining the CNF fibril-like morphology. The theoretical maximum amount of sulfur if all hydroxyls were functionalized would result in ~24 wt% sulfur. The sulfonation reaction was relatively initially quick; where for the three different CSA to AGU reactions over 50% of the sulfur content was on the CNF after 5 minutes of reaction time, as compared to after 60 minutes of reaction time.

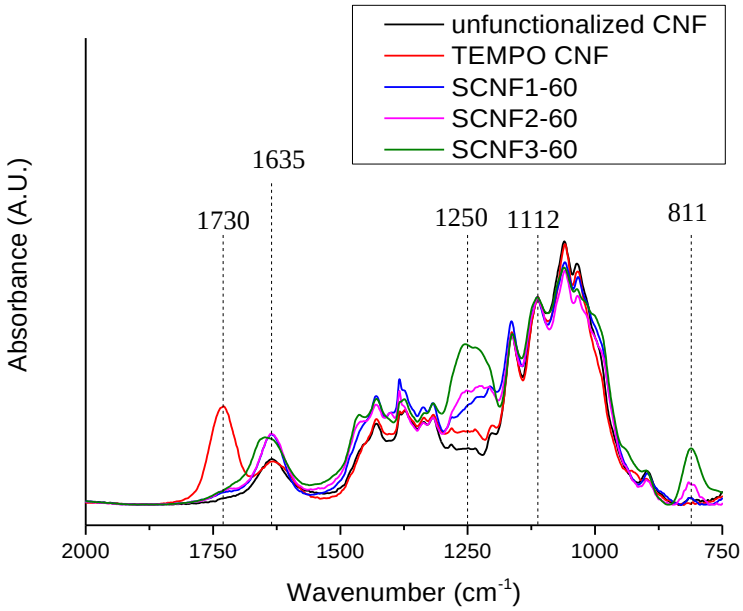

Figure 4.2. FTIR spectra of the CNF films (cast from CNF-water suspension) showing differences in peaks between unfunctionalized and functionalization CNF.

The FTIR spectra (**Figure 4.2** and **Figure C.2**) were normalized to the peak at 1112 cm^{-1} (stretching of the C-O-C and in-phase ring wagging), because the functionalization should have little effect on it [137]. The peak around 1635 cm^{-1} is typically associated with

bound water, while the SCNF3-60 displayed a bound water peak at 1647 cm^{-1}. The 1730 cm^{-1} peak is associated with the acid form of carboxyl groups (COOH) [82, 151]. The sulfonated CNF have 2 new peaks, a broad peak at 1250 cm^{-1} and a relatively narrow peak at 811 cm^{-1} associated with S=O and C-O-S bonds, respectively [152]. The presence of these peaks, which were not present in the unfunctionalized and TEMPO CNF, indicates that the CNFs were sulfonated. With increasing CSA to AGU ratios the 1250 and 811 cm^{-1} peaks had higher absorbance indicating the samples were more sulfonated, which is supported by the elemental analysis (**Table 4.1**). This result is expected and is consistent with literature [153, 154]. The exception was SCNF1-30, despite elemental analysis showing higher sulfur content than SCNF1-5, there was less absorbance than SCNF1-5, and the reason for this discrepancy is unclear.

4.3.3 Change in Crystallinity

The WAXD integrated radial patterns of unfunctionalized CNF, TEMPO CNF, and SCNF3-60 is given in **Figure 4.3**, showing this sulfonation method can affect the crystallinity of the resulting CNF (**Table 4.1**). In general, there was a lower CI with longer reaction times and with higher CSA to AGU ratio. For comparison, the decrease in CI was much lower with the sulfonation approach used in this study than the regioselective oxidative bisulfite method [80]. Liimatainen et al [80] reported a sulfonated CNF with 0.51 mmol of sulfonated groups/g cellulose resulted in a ~ 54% decrease in CI (i.e. from ~65% down to ~30%). By comparison, for the SCNF1-60 sample, having similar concentration of sulfonated groups (0.56 mmol/g cellulose), had only a ~3% decrease in CI (i.e. from 75% down to 73%). Even the most sulfonated sample in our study, SCNF3-60 (1.79

mmol/g cellulose), had only a ~29% decrease in CI (i.e. from 75% down to 53%). This shows the reaction method used in this study maintains the cellulose crystal structure much better than the regioselective oxidative bisulfite method. The retention of CI should result in higher mechanical properties of the functionalized CNF, which can be translated into higher properties of CNF films and composites.

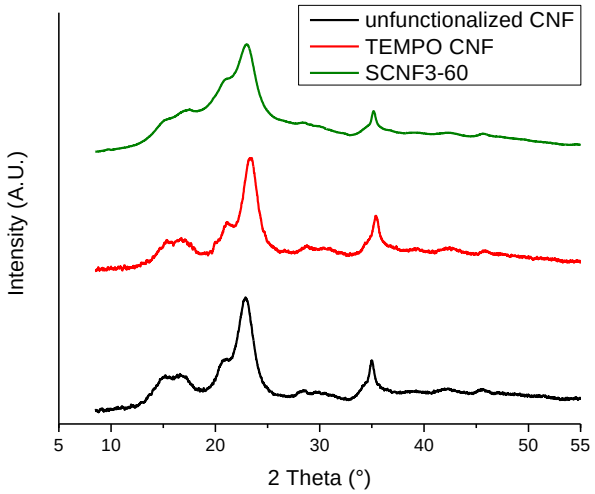

Figure 4.3. WAXD integral scan of the unfunctionalized, TEMPO CNF, and SCNF3-60.

4.3.4 Zeta Potential

Zeta potential is the measure of the difference between the electrostatic potential of two surfaces, and can be used to assess the stability of CNF suspensions [155, 156]. The zeta potential of each sample in 0.5 mM NaCl aqueous solution, was -25 mV, -49 mV and -39 to -48 mV for unfunctionalized, TEMPO, and sulfonated CNFs, respectively. This zeta potential measured for unfunctionalized CNF is consistent with what is reported in other studies for cellulose [157, 158]. For the sulfonated samples, in general, for the same CSA to AGU ratio longer reaction times typically lead to slightly higher zeta potentials. The highest zeta potential was -48 mV for SCNF3-60, which had the longest reaction time at

the highest CSA to AGU ratio. Interestingly, when extending sulfonation reaction times beyond the initial 5 minute reaction (i.e. SCNF1-5, SCNF2-5, and SCNF3-5), the change in zeta potential with increasing sulfur content was minimal, suggesting that the surface of the fibrils reacts quickly and reach a saturated state. Further sulfonation seems to only marginally increase the zeta potential. This may be due to additional sulfur groups being located below the fibril surface where they are shielded from solution and are not able to contribute to the surface charge. This is somewhat corroborated by the decrease in crystallinity with increasing sulfur content, suggesting that the cellulose chains become less ordered with increased sulfonation.

4.3.5 Dispersibility

UV-Vis spectra can be used to assess the dispersion quality of suspensions, because transmittance is related to the width of the nanofiber, which in turn can be related to aggregation of the CNF [78, 159, 160]. The UV-Vis data for unfunctionalized, TEMPO, and sulfonated CNFs dispersed at 0.1 wt% either in water or in DMF is given in **Figure 4.4** and **Figure C.3** and the transmittance values of all the samples at 600 nm are listed in **Table 4.1**. All sulfonated CNF dispersions have better transparency than the unfunctionalized CNF, and in many cases were even better than TEMPO CNF dispersion. In general, longer sulfonation times leads to higher transmittance, and there is a large increase in transparency for the sulfonated CNF between 5 and 30 minutes of reaction time, while there is little change in transparency between 30 and 60 minutes. Though the mechanism is for this behavior is unclear, it is plausible that the increase in transmittance from the unfunctionalized CNF to the 5 minute sulfonated CNFs (i.e. SCNF1-5, SCNF2-

5, and SCNF3-5) is a result of improved dispersion as seen from the increased surface charge. Whereas the increase in transmittance between 5, 30 and 60 minutes, is a consequence of a finer CNF morphology resulting from the sub-surface sulfonation of the CNF (see **Figure C.1**), allowing for increased CNF fibrillation during the homogenization steps when making the dispersion used for UV-vis testing.

Our sulfonated CNF displayed significantly better transmittance in solvent compared to unfunctionalized CNF with as low as 5 minutes of reaction time, while the previously reported sulfonation method (regioselective oxidative bisulfite) for CNF took over 3 days of reaction time [80, 81, 161]. Depending on the CSA to AGU content only 30 to 60 minutes of reaction time is needed to make a sulfonated CNF that has comparable to or better transmittance in solvent than TEMPO CNF, which is shorter than the preparation time for post TEMPO treatment of existing CNFs as what was done in this study.

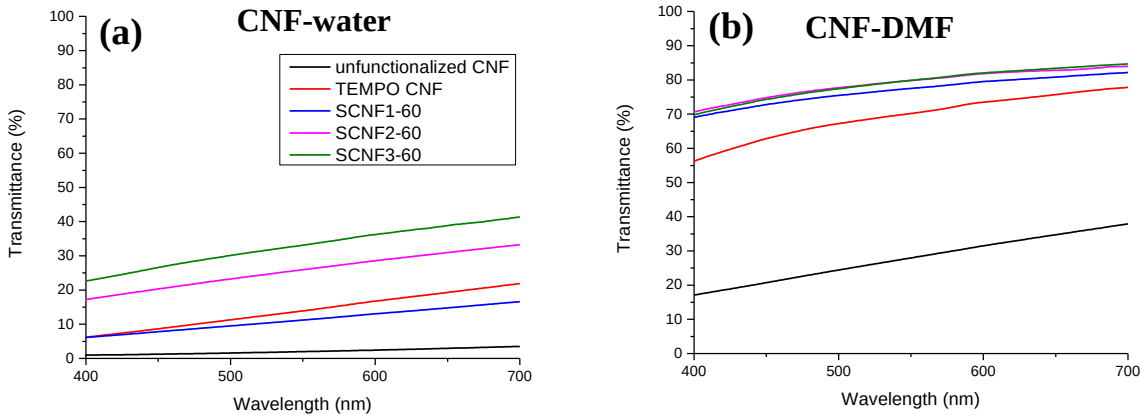

Figure 4.4. UV-Vis spectra of CNF dispersions in **(a)** water and **(b)** DMF after 3 days of sonication showing all functionalized samples have higher transparency than the unfunctionalized sample.

4.3.6 Effect of Dispersing and/or Heating in Different Solvent

The effects of dispersing CNFs in DMF versus water, and heating of CNF-solvent suspensions on the functional groups were also studied, because materials often undergo heating in solvent in the process of making composites. Films were made by the process previously described with the 3 days of dispersion. After the dispersion half of the suspension was cast to produce films, while the other half of the suspension was then subjected to 70 °C for 3 days before being cast into films.

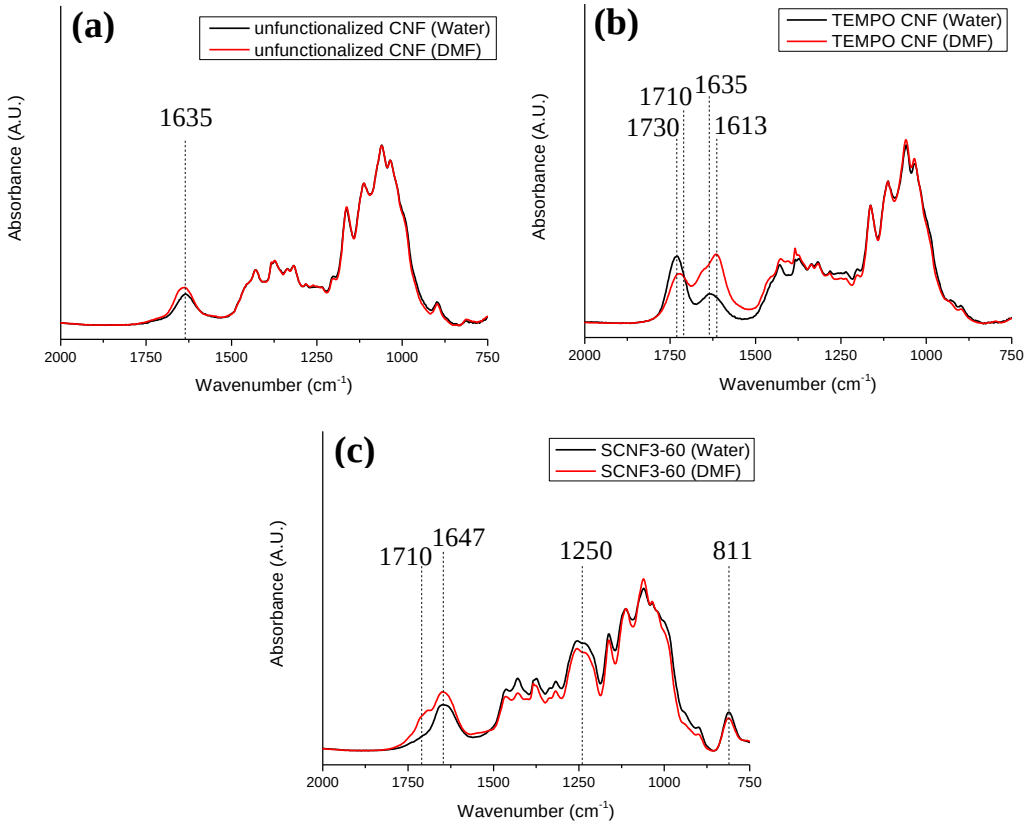

Figure 4.5. Comparison of FTIR spectra of CNF film cast after being dispersed in water versus DMF (no heating). **(a)** unfunctionalized CNF showing no difference, **(b)** TEMPO CNF showing a decrease in the 1730 cm^{-1} peak and a newly developed peak at 1613 cm^{-1} associated with the COO^- when dispersed in DMF, and **(c)** SCNF3-60 developing shoulder at 1710 cm^{-1} when dispersed in DMF.

FTIR comparison of the unfunctionalized CNF films cast from CNF-DMF versus CNF-water suspensions shows there was minimal differences (**Figure 4.5**). The SCNF3-60 sample dispersed in DMF showed a slight decrease in magnitude of the peaks associated with sulfate groups (1250 and 811 cm^{-1}). Additionally, there was the development of a shoulder at 1710 cm^{-1}, which could be associated with C=O in formate and will be discussed later. The TEMPO CNF cast from DMF exhibited a broadening of and decreased amplitude of the peak associated with COOH (~1730 cm^{-1}), and also a peak develops at 1613 cm^{-1} that is associated with COO^- [82, 151]. The decrease in the 1730 cm^{-1} peak and the newly developed 1613 cm^{-1} peak is due to the acid form carboxyl groups forming (carboxyl dimethylammonium groups), and will be discussed later. The broadening of the 1730 cm^{-1} peak occurs due to the larger peaks at 1613 and 1635 cm^{-1} overlapping with the 1730 cm^{-1} peak.

FTIR comparison of the films cast from CNF-water suspensions with and without heating indicates there is no change in unfunctionalized and TEMPO CNF when it was heated (**Figure 4.6**). For SCNF3-60, there was a drastic decrease in the peak heights associated with sulfonation (1250 and 811 cm^{-1}), suggesting a cleavage of the sulfate groups off the CNFs, as has been previously reported for cellulose nanocrystals when heated [162-164].

FTIR comparison of the films cast from CNF-DMF suspensions with and without heating indicates there was no change in unfunctionalized and TEMPO CNF as a result of heating (**Figure 4.7**). For the SCNF3-60 sample, a peak develops at 1710 cm^{-1}, where only a shoulder was present without heating. There was a decrease in the peaks associated with

sulfonation (1250 and 811 cm^{-1}), similarly to what happened after heating the CNF-water suspensions. There was also a shoulder previously because of the larger peak at 1635 cm^{-1} for bound water before heating due to more sulfate groups and its hydrophilicity.

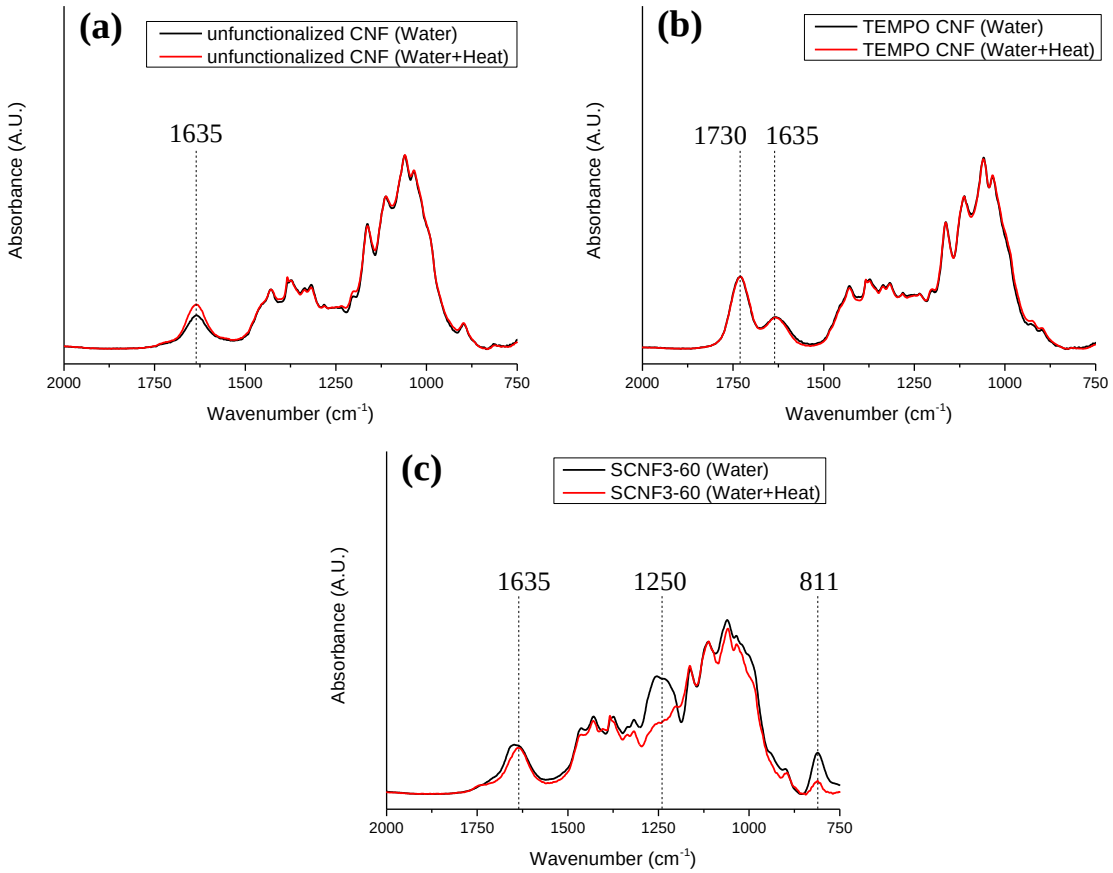

Figure 4.6. Comparison of FTIR spectra of CNF dispersed in water (no heating) and cast versus the dispersion heated for 3 days at 70 °C then cast. After heating the **(a)** unfunctionalized CNF shows no change, **(b)** TEMPO CNF shows no change, and **(c)** SCNF3-60 shows a decrease in the 1250 and 811 cm^{-1} due to cleavage of the sulfate groups.

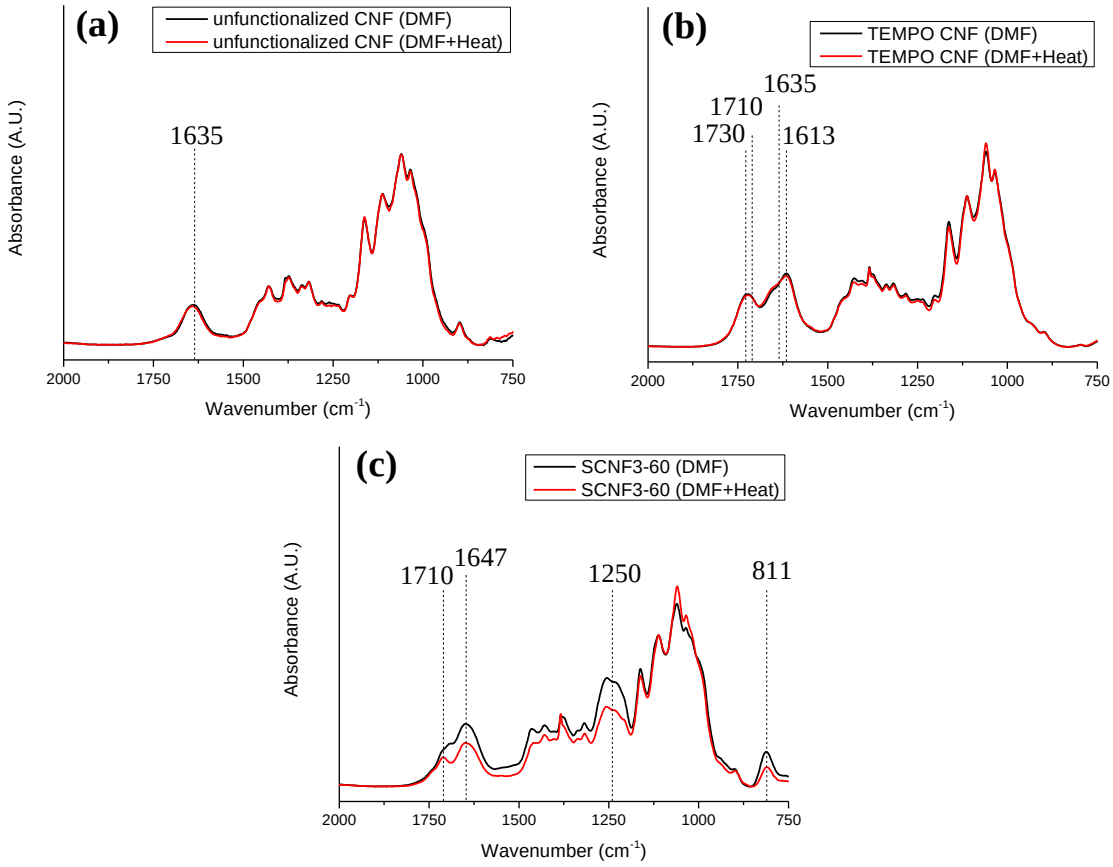

Figure 4.7. Comparison of FTIR spectra of CNF dispersed in DMF (no heating) and versus the dispersion heated for 3 days at 70 °C then cast. After heating the **(a)** unfunctionalized CNF shows no difference, **(b)** TEMPO CNF shows no difference, and **(c)** SCNF3-60 showing a decrease in the 1250 and 811 cm^{-1} due to cleavage of the sulfate groups. Also a decrease in the 1647 cm^{-1} peak and the shoulder at 1710 cm^{-1} developing into a peak

The mechanism for additional functionalizations to TEMPO and sulfonated CNF when dispersed in DMF occurs because dimethylformamide decomposes into formic acid and dimethylamine in the presences of water. These two compounds can undergo partial ionization to form dimethylammonium cations and formate anions [165]. The decomposition of DMF can be seen in the equations below.

$$HCON(CH_3)_2 + H_2O \rightarrow HCOOH + (CH_3)_2NH \quad \textbf{(4.2)}$$

$$HCOOH + (CH_3)_2NH \leftrightarrow HCOO^- + (CH_3)_2NH_2^+ \quad \textbf{(4.3)}$$

Upon addition of CNFs to DMF trace amount of water is introduced that promotes the formation of the DMF degradation products. The peak observed at 1710 cm^{-1} in the FTIR spectrum of the sulfonated samples when dispersed in DMF is typically associated with carbonyl groups, suggests that an exchange of functional groups may be occurring during mixing CNF in DMF. It is known that cellulose formate can form when formic acid is added to a cellulose/DMF suspension. The formic acid formation due to the degradation of DMF results in formate groups forming on the CNF. It has also been shown that sulfuric acid can act as a catalyst for the formation of cellulose formate [166, 167]. Since the sulfate groups can cleave off the cellulose into the solvent, it could help promote cellulose formate formation. This would explain why such a strong peak was seen in SCNF3-60, but not seen in the unfunctionalized and TEMPO CNF. The formation of cellulose formate can be seen in **Equation 4.4**.

$$CNF^{SO_3^-} + [HCOOH] + [H^+] \leftrightarrow CNF^{COOH} + [SO_4]^- + [H^+] \quad \textbf{(4.4)}$$

The dimethylammonium cations can therefore undergo a neutralization reaction with the carboxylic acid groups (COO^-) of TEMPO CNF or the sulfate groups (SO_3^-) of the sulfonated CNF to form a dimethylammonium salt [165]. The reaction for TEMPO CNF after dissociating in the solvent to form carboxyl dimethylammonium can be seen below. The same reaction can possibly happen for sulfonated CNF in the equations below the COO- can be replaced with SO_3^- representing the sulfate group after dissociating.

$$_{CNF}COO^- + (CH_3)_2NH_2^+ \leftrightarrow [_{CNF}COO^-][(CH_3)_2NH_2^+] \quad \textbf{(4.5)}$$

Evidence for this type of reaction can be seen by examining the FTIR spectrum of the TEMPO CNF (**Figure 4.5**) that shows a decrease in the peak associated with COOH and a newly developed peak associated with COO^- when dispersed in DMF. This peak associated with COO^- was not seen when the TEMPO CNF was dispersed in water. This peak at 1613 cm^{-1} associated with COO^- does not exist in the sulfonated and unfunctionalized CNF films whether they were cast from water or DMF.

To further support the formation of this dimethylammonium functional group on the CNF, when TEMPO and sulfonated CNF–DMF suspensions were heated at 70 °C for 3 days, the suspensions turned yellowish with TEMPO CNF being more yellow than the sulfonated CNF (**Figure C.4**). This yellowing was not seen in the unfunctionalized CNF heated in DMF, and in any of the CNF samples when heated in water. Previously it was shown that CNF film functionalized with an ammonium carboxylate group ($COONH_4$) would turn yellow after undergoing heating, though the reason for yellowing was unclear [168]. The dimethylammonium carboxyl CNF derivative is similar in chemistry to the CNF functionalized with an ammonium carboxylate group mentioned above and should behave similarly. The amount of yellowing is possibly an indicator of how much dimethylammonium has neutralized the ionized groups on the CNF, which would mean it is more prominent in the TEMPO CNF than the sulfonated CNF.

To test the possibility that the yellowing of TEMPO CNF in DMF was a result of inadequate removal of reagents used for the functionalization, separate dispersions of

TEMPO, NaCl, and HClO in DMF were left at 70 °C for 3 days. It was found that none of these chemicals in DMF or DMF itself turned yellow. **Figure C.5** contains images of these results. Acetic acid, which has a similar functional group to the TEMPO CNF (carboxylic acid), was also mixed with DMF and heated as previously described and it also did not lead to a yellowing of the solution (**Figure C.5**).

4.4 Conclusion

Existing CNFs were successfully sulfonated with a DMF and CSA solution resulting in a sulfonated CNFs with a high surface charge while retaining a fibril-like morphology. This one step reaction is relatively rapid, and a reaction time of as little as 5 minutes leads to a significant increase in the zeta potential and dispersibility in water and DMF when compared to the unfunctionalized CNFs. A post-TEMPO oxidation treatment on existing CNFs and regioselective bisulfite oxidation method can yield CNF with similar dispersibility but they require multiple step reactions and longer reaction times. For sulfonated CNFs, higher CSA to AGU ratio, and longer reaction times leads to higher sulfur content on the CNFs and also lower crystallinity. This decrease in crystallinity was much less than the regioselective bisulfite oxidation process reported in the literature for the same amount of sulfonation. It was observed that when TEMPO and sulfonated CNF were dispersed in DMF, additional functionalization occurred that did not happen with unfunctionalized CNF. The TEMPO CNF's additional functionalization is mainly dimethylammonium carboxyl groups, and the sulfonated CNF's additional functionalization is mainly cellulose formate. These results suggest that this post

sulfonation method can be used to rapidly tailor the dispersibility of unfunctionalized CNF for a wide range of applications.

CHAPTER 5. GEL SPINNING OF POLYACRYLONITRILE AND CELLULOSE NANOFIBRIL FIBERS

5.1 Introduction

Surface chemistry has a significant effect on how nanofillers disperse in and interact with polymer. To study the effect of surface chemistry on the reinforcement effect of CNFs in PAN two different type of functionalized CNF were incorporated into PAN fibers. One of the functionalization studied is the TEMPO oxidized CNF, because it is the most common functionalization of CNFs. The other functionalization looked at is an amination method that has not yet been done on cellulose nanofibrils. The amine group is hypothesized to interact better with PAN than the carboxylic acids groups on the TEMPO oxidized CNF.

CNF polymer fiber composites have been less studied than CNC polymer fiber composites. There is only 1 study where polymer-CNF fibers were continuously spun and then continuously post drawn. This fiber was made with PVA with only a CNF loading of 1 wt% [68]. In this study we looked at polymer-CNF fibers with CNF loadings as high as 10 wt%. In addition to the effect of CNF functionalization on resulting fiber properties, the effect of spinning, and drawing parameters were also investigated.

5.2 Experimental

5.2.1 Materials

Polyacrylonitrile-co-methacrylic acid (PAN-co-MAA; 4 wt% of MAA content, viscosity average molecular weight: 2.47×10^5 g/mol) was obtained from Exlan Co., Japan, and will be referred to as PAN-co-MAA powder. Mechanically ground CNF in water (2.5

wt% solids) (lot# 2012-FPL-CNC-48/051) were obtained from the University of Maine, US. ACS grade Dimethylsulfoxide (DMSO), Sodium meta periodate (NaIO) (≥99%), and Ethylenediamine (≥99%) were obtained from Sigma-Aldrich co. TEMPO free radical (98%), sodium hypochlorite (NaClO) (9.8 % available chlorine in water), and sodium hydroxide (NaOH), were obtained from Alfa Aesar. ACS grade methanol was obtained from VWR and used as is.

5.2.2 TEMPO oxidation of Cellulose Nanofibrils

In a large container 160 gram of the CNF slurry (2.5 wt%) and 340 mL of DI water were mixed with an overhead stirrer to create a 0.8 wt% CNF slurry. Then 0.08 g of TEMPO free radical and 0.5 g NaBr was added to the suspension while undergoing stirring that maintained a vortex for 1 hour to make sure the chemicals were dissolved. The pH of the suspension was adjusted to 10.5 by adding 0.5 M NaOH aqueous solution. The pH was monitored with a pH meter UltraBASIC (Denver Instruments). Then 12.9 g of NaClO aqueous solution (9.8 wt% available chlorine) was added drop wise, after this addition, the pH was monitored and adjusted to stay between 10-10.5 by adding 0.5 M NaOH aqueous solution. Once the pH stabilizes the reaction is finished (~1 hour). Afterward the CNF was centrifuged and washed with DI water until the pH of the supernatant was neutral (pH strips were used), followed by two additional washings. The solid content of the washed CNF was determined by thermogravimetric analysis and then adjusted to a solid content of 0.4 wt%. The CNF suspension (0.4 wt%) was then homogenized with 2 passes through a Nano DeBEE Laboratory homogenizer at a pressure of 25000 psi through an orifice with a diameter of 0.2 mm. The CNF-water suspension was mixed with equals parts DMSO and

the excess water was vacuum distilled out with a rotary evaporator. The TEMPO CNF will be referred to as TCNF for the rest of the paper. (See **Appendix D** for discussion on the TEMPO CNF processing procedure used).

5.2.3 Amination of Cellulose Nanofibrils

The CNF functionalization was done by in a large container 320 gram of the CNF slurry (2.5 wt%) and 680 mL of DI water were mixed with an overhead stirrer to create a 0.8 wt% CNF slurry. The slurry was heated to 45 °C and the pH was lowered to 3.5 and then reacted with 32 grams of sodium meta periodate for 2.5 hours (container was covered in aluminum foil to prevent light degrading the periodate). Then 75 ml of polyethylene glycol was added and stirred for 30 minutes to end the reaction. The sample was then clean through centrifugation with a Sorvall Evolution RC Centrifuge 5 times. 18 liters of DI water was used during this whole centrifugation cleaning process. The sample was then dispersed in 1 L of DI water and heated to 30 °C and 100 ml of ethylenediamine was added an allowed to react overnight. 9.3 grams of sodium borohydride was dissolved in 50 ml of 0 °C DI water and added to the cellulose suspension to end the reaction. The sample was then clean with the same centrifugation process mentioned above. The functionalized CNF was dispersed in DI water to a solid content of 0.4 wt% (Checked with TGA). The pH was lowered to 4 with 0.3 M acetic acid. The suspension was then homogenized by passing it through a Nano DeBEE laboratory homogenizer with a 0.20 mm diameter orifice at a pressure of 25,000 psi 2 times. This aminated CNF will be referred to as ACNF for the rest of the paper (reaction scheme seen in **Figure 5.1**). The ACNF-water suspension was mixed with equals parts DMSO and the excess water was vacuum distilled out with a rotary

evaporator. The reason DMSO was used instead of dimethylformamide (DMF) which was used in the previous chapters is because TCNF was found to not disperse well in DMF at higher concentrations (see **Figure 5.2**) forming aggregates while these aggregates where not seen when TCNF was dispersed in DMSO and concentrated. This was further tested by trying to pass the CNF dispersions through a 44 µm filter the TCNF-DMF suspension did not pass through the filter while the TCNF-DMSO suspension did.

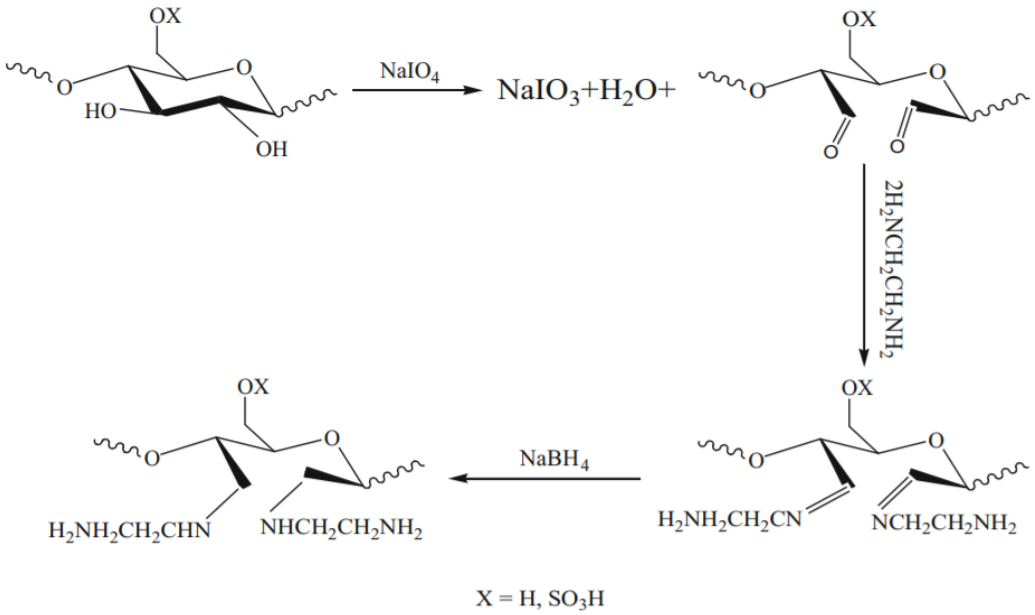

Figure 5.1. Reaction scheme used to make the aminated cellulose nanofibrils [169].

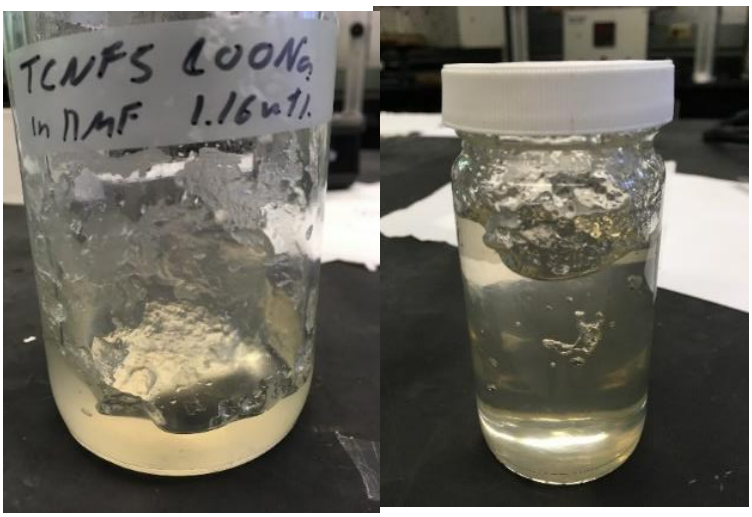

Figure 5.2. Image of TCNF dispersed in DMF **(Left)** and DMSO **(Right)**. It can be seen in the TCNF-DMF dispersion aggregates formed, and in the TCNF-DMSO dispersion aggregates did not form.

5.2.4 Solution/suspension preparation

Six different solutions/suspensions were made with 0 wt% CNFs, 1 wt% TCNFs, 5 wt% TCNFs, 10 wt% TCNFs, 1 wt% ACNFs, and 5 wt% ACNFs with respect to the weight of the polymer, these samples will be referred to as neat PAN-co-MAA, TCNF-1, TCNF-5, TCNF-10, ACNF-1, and ACNF-5 respectively. To make one solution/suspensions a total of 15 grams of solids were used. The desired amount of CNF (depending on desired final CNF content) were dispersed at 0.2 wt% in DMSO by sonicating in a bath sonicator (Branson 3510R-MT, 100 W, 42 kHz) for 24 hours before use. The neat PAN-co-MAA solution was made by adding the desired amount of neat PAN-co-MAA powder (depending on desired CNF content) into a glass reactor into 100 ml of DMSO, and mechanically mixed at 100 rpm at 70 °C for 3 hours. The neat PAN-co-MAA solution process stopped here. To make the PAN-co-MAA/CNF suspensions the process continued and the CNF/DMSO suspension was then added to PAN-co-MAA solution in

increments of up to 200 ml. The PAN-co-MAA/CNF/DMSO suspensions were heated to 100 °C, and the excess DMSO was removed by vacuum distillation. This was repeated until all the desired amount of CNFs has been added, and once the suspension has reached a desirable spinnability.

5.2.5 Fiber spinning and drawing

The fibers were spun using a Hills, Inc spinning unit with a one hole spinneret (200 µm). The solution/suspensions were spun into a room temperature methanol bath at a rate of 1 cm^3/min. The as spun fibers were collect onto a spool at 1x (32 m/min), 2x (64 m/min), and 3x (96 m/min) as spun draw ratios (ADR). If the fibers were cold drawn it was done at room temperature with a cold draw ratio (CDR) of 1.3x, and 1x CDR means it was not cold drawn. If the fibers were hot drawn it was done by passing the fiber through a glycerol bath between 125-165 °C depending on temperature the fibers were drawable at. The TCNF-10 fiber was hot drawn through an air oven at 170 °C instead of using a glycerol bath. The hot draw ratio (HDR) used for the fibers varied and an 1x HDR meant it was not hot drawn. The total draw ratio (TDR) was calculated by multiplying the ADR, CDR, and HDR together. Tables of all the fibers and their tensile properties can be seen in **Appendix D Table D.1-15.** (See **Appendix D** for discussion on other fiber spinning trials not reported in this chapter).

5.2.6 Characterization

Rheological measurements were performed on an ARES rheometer (Rheometric Scientific, Co.). The testing was done at room temperature, with 25 mm parallel plates, and a gap size of 1 mm. To prevent evaporation of solvent and absorption of water during

testing a layer of silicon oil was applied to the exposed sample surface around the sides of the parallel plates. The linear viscoelastic region (LVR) was determined for each sample by running a strain sweep test at an oscillatory frequency, ω, of 0.5, 10, 100, and 300 rad/s. The solid content of the final solution/suspensions was measured by thermogravimetric analysis (TGA500, TA instruments.).

Tensile tests were completed at room temperature at a strain rate of 60 %/min on 133 different samples (CNF loading, functionalization, and processing differences) at 25.4 mm gauge length using a FAVIMAT+ (Measured Solutions Inc.) for each sample 25 filaments were tested. The linear densities of each fibers were measured by a vibroscope before tensile testing. The measured linear density was converted to an effective diameter using the measured bulk density of PAN (1.18 g/cm^3) and cellulose nanofibrils (1.5 g/cm^3).

Wide-angle X-ray diffraction (WAXD) of all samples were done with a Rigaku MicroMax-002 (CuK_α, λ=0.1542 nm) and a Rigaku R-axis IV++ detector. MDI Jade 9 software was used to analyze the WAXD pattern.

5.3 Results and Discussion

5.3.1 Solution/suspension rheology

The solid content of the solution/suspensions used to spin fibers can be found in **Table 5.1**. The complex viscosity and tan delta curves of the solution/suspensions can be found in **Figure 5.3**. The solid content of the suspensions had to be lowered with increasing CNF loading to allow a spinnable suspension to be made. It can be seen that even though we lowered the solid content of the TCNF-10 suspension significantly to 8.9 wt% from 13.4 wt% for the neat PAN-co-MAA solution the viscosity of the TCNF-10

suspension was much higher at low shear rates. A high viscosity at low shear rates is a problem for spinning fiber because it inhibits air bubbles from leaving the solution/suspensions resulting in voids in the fibers, which is one of the reasons we had to reduce the solid content of the PAN-CNF suspensions. Another reason the total solid content of the suspensions was lowered was to reach a viscoelasticity behaviour from which a fiber could be spun.

Table 5.1. Overview of the solution/suspensions used in this study.

Sample	Solid content (wt%)
neat PAN-co-MAA	13.4
TCNF-1	13.5
TCNF-5	10.3
TCNF-10	8.9
ACNF-1	12.9
ACNF-5	12.4

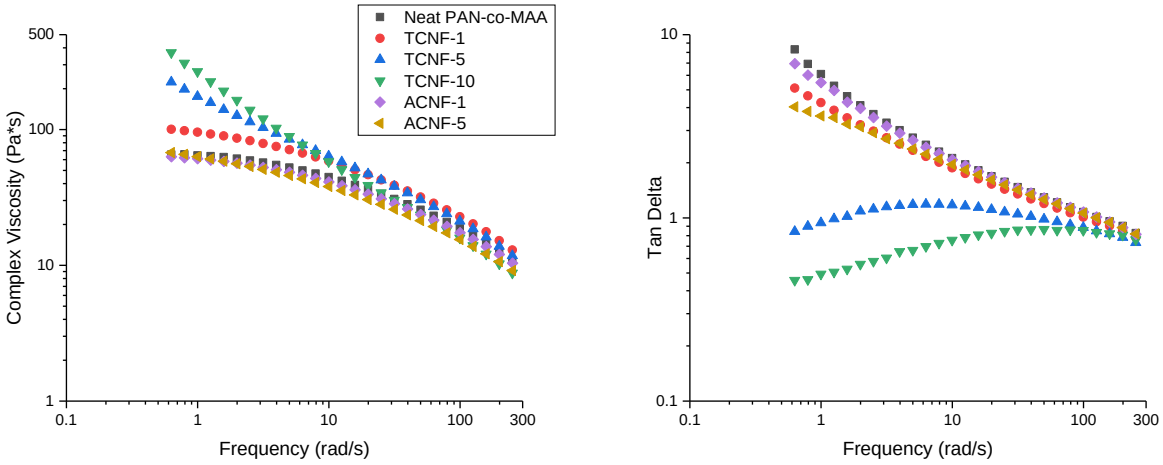

Figure 5.3. Rheological properties of the solution/suspensions **(a)** complex viscosity and **(b)** Tan delta.

We can see from **Table 5.1** and **Figure 5.3** that the TCNF had a much larger effect on the rheological properties than the ACNF. Even though the TCNF-5 had a lower

solid content than the ACNF-5, the viscosity was higher. We can also see in the tan delta plot, there is an increase in the tan delta at low shear rates for the TCNF-5 and TCNF-10, indicating that the suspension is getting more liquid like. The reason we believe this occurs is due to the breakdown of the TCNF percolation network in the suspensions when it is sheared. We do not see this behavior in the PAN/ACNF suspension samples indicating that there is little to no percolation network formed. Factors such as CNF and polymer interaction, CNF dispersion, and CNF aspect ratios can affect whether or not a percolation netowork forms.

5.3.2 Effect of as spun draw ratio and CNF loading on drawing conditions and drawability

It was found that for the PAN/TCNF fiber samples, higher loadings of TCNF resulted in the highest ADR being lower than for the neat PAN-co-MAA. TCNF-1 could have an ADR of up to 3. While the TCNF-5 could only have an ADR up to 2, and the TCNF-10 could only be spun with an ADR of 1. ACNF-1 and ACNF-5 could both be spun with an ADR of 3. The reason for the decrease in the ADR for the higher TCNF loaded samples is due to changes in viscoelasticity of the suspension due to the TCNF percolation network present, and because of the decrease in the total solid content of the suspensions.

It was found that fibers spun with a higher ADR had to be drawn at a lower glycerol temperature (**Table 5.2**). This is likely due to the larger diameter of the fibers spun at a lower ADR and these larger diameter fibers can survive the higher temperatures of the glycerol bath for longer period of time. It was also found that samples with higher CNF loading had to be drawn at lower glycerol temperature.

The higher CNF loaded fiber samples had a lower maximum TDR when compared to the neat PAN-co-MAA fibers. This is an expected result and typically when fillers are added, the drawability of the fiber decreases. Though there have been reports that drawability does not change and occasionally even increases with the incorporation of fillers. Such an increase in drawability with the incorporation of CNCs into PAN fibers was reported by Chang et al. [170].

Table 5.2. Drawing temperature for different fibers.

Sample	ADR	Glycerol drawing temperature (°C)
neat PAN-co-MAA	1	165
neat PAN-co-MAA	2	155
neat PAN-co-MAA	3	145
TCNF-1	1	155
TCNF-1	2	145
TCNF-1	3	135
TCNF-5	1	140
TCNF-5	2	125
ACNF-1	1	155
ACNF-1	2	145
ACNF-1	3	140
ACNF-5	1	155
ACNF-5	2	145
ACNF-5	3	135

The effect of processing parameters such as, ADR, CDR, and CNF loading had on the maximum TDR was looked at (**Table 5.3**). It was found that typically higher ADR lead to higher maximum TDR. From the data there is no consensus on whether cold drawing lead to higher maximum TDR. Three out of 11 samples with cold drawing and 5 out of 11 samples with no cold drawing at the same ADR had the higher maximum TDR (not comparing 3x ADR for neat PAN-co-MAA). There is not an obvious trend for why some sample had higher maximum TDR with or without cold drawing and it is possible that

different processing parameters with glycerol bath temperature and drawing speed might have to be optimized each sample to reach the maximum potential drawing limit.

Table 5.3. Difference between maximum total draw ratio of fibers depending on ADR ratio and whether it has been cold drawn.

	Samples	Maximum TDR of fibers with 1x CDR	Maximum TDR of fibers with 1.3x CDR
1x ADR fiber	Neat PAN-co-MAA	20	15
	TCNF-1	15	15
	TCNF-5	13	N/A
	TCNF-10	7	N/A
	ACNF-1	15	10
	ACNF-5	12	11
2x ADR fiber	Neat PAN-co-MAA	20	25
	TCNF-1	20	20
	TCNF-5	12	N/A
	TCNF-10	N/A	N/A
	ACNF-1	22	18
	ACNF-5	13	16
3x ADR ratio fiber	Neat PAN-co-MAA	N/A	35
	TCNF-1	25	20
	TCNF-5	N/A	N/A
	TCNF-10	N/A	N/A
	ACNF-1	20	28
	ACNF-5	15	19

5.3.3 Effect of drawing on strain at break

It was found that for all different compositions of fibers spun at different ADR that drawing the fibers at low draw ratios could increase the strain at break (**Appendix D. Tables D.1-D.15).** We can see in **Table 5.4** for all the fibers that could be cold drawn that there was an increase in strain at break after cold drawing.

Table 5.4. Strain at break comparison between as spun fiber, cold drawn fiber, and fully drawn fiber showing that strain at break increased after cold drawing. Also that the maximum drawn fiber can have a larger strain at break than the as spun fiber.

Sample	ADR	Strain at break of as spun fiber (%)	Strain at break after cold drawing (%)	Maximum TDR drawing conditions (ADR-CDR-HDR=TDR)	Strain at maximum TDR (%)
neat PAN-co-MAA	1	2.8 ± 0.5	6.1 ± 1.3	1x-1x-20x=20x	8.7 ± 0.5
neat PAN-co-MAA	2	24.1 ± 19.3	25.5 ± 14.4	2x-1.3x-9.6x=25x	8.3 ± 0.5
neat PAN-co-MAA	3	16.7 ± 14.0	77.3 ± 22.1	3x-1.3x-9x=35x	8.3 ± 0.5
TCNF-1	1	1.2 ± 0.4	3.3 ± 0.3	1x-1.3x-11.5x=15x	8.8 ± 0.5
TCNF-1	2	3.1 ± 0.4	4.9 ± 1.2	2x-1x-10x=20x	7.9 ± 0.9
TCNF-1	3	3.1 ± 0.4	7.4 ± 1.5	3x-1x-8.3x=25x	7.3 ± 0.4
TCNF-5	1	1.8 ± 0.6	N/A	1x-1x-13x=13x	5.5 ± 0.6
TCNF-5	2	1.5 ± 0.4	N/A	2x-1x-6x=12x	5.9 ± 0.9
TCNF-10	1	0.7 ± 0.2	N/A	1x-1x-7x=7x	7.3 ± 0.5
ACNF-1	1	2.6 ± 0.7	11.0 ± 7.6	1x-1x-15x=15x	9.3 ± 0.6
ACNF-1	2	9.6 ± 0.7	41.7 ± 8.8	2x-1x-11x=22x	8.7 ± 0.3
ACNF-1	3	9.5 ± 4.0	43.4 ± 13.4	3x-1.3x-7.2x=28x	7.8 ± 0.9
ACNF-5	1	2.7 ± 0.6	6.8 ± 2.5	1x-1x-12x=12x	9.5 ± 0.5
ACNF-5	2	6.1 ± 2.4	8.4 ± 9.1	2x-1.3x-5.8x=15x	8.5 ± 0.5
ACNF-5	3	10.1 ± 4.8	14.9 ± 5.4	3x-1.3x-4.9x=19x	7.2 ± 0.3

Chang et al. [170] previously reported that when PAN fiber with 40 wt% CNC loading was drawn the strain at break increased from 1.5% at 4x TDR to 8.0% at the maximum TDR. The authors associated this low strain at break at low draw ratio to the percolation network of the CNC, and that drawing removed the percolation network. In that study, the lowest draw ratio fiber was 4x which was made with an ADR of 3x and a CDR of 1.3x. Similar results were seen in our study, where that drawing the fiber to the maximum TDR could result in a fiber with a higher strain at break (typically around 7-9%) than the low draw ratio fiber, we see this behaviour in a majority of our composite fibers (**Table 5.3**). This increase in strain at break with drawing was also exhibited by the neat PAN-co-MAA fiber when spun with ADR of 1x. The strain at break development for the fibers with an ADR of 1 with no cold drawing with respect to the TDR can be found in **Figure 5.4**. Chang et al. [170] attributed this increase strain at break with drawing due to breaking the CNC percolation network in the PAN-CNC fibers, but our results here indicates that theory could possibly be incorrect. Since the behaviour of increase strain at break was observed in the neat PAN-co-MAA fiber with an ADR of 1 means this can occur in a system which does not contain fillers. Since the increase strain at break with drawing can occur in a neat polymer system, a percolation network break down is not the only reason an increase in strain at break can occur. This leads to the possibility that the fillers in the composites can be driving the PAN-co-MAA structure to develop similarly to the structure that formed in the neat PAN-co-MAA with an ADR of 1x, and it is this PAN-co-MAA structure that leads to the low strain at break in low TDR fibers. Though it is also possible as proposed by Chang et al. that the breakdown of the percolation network occurs

with drawing and the percolation network leads to the low strain at break or both of these are contributing factors.

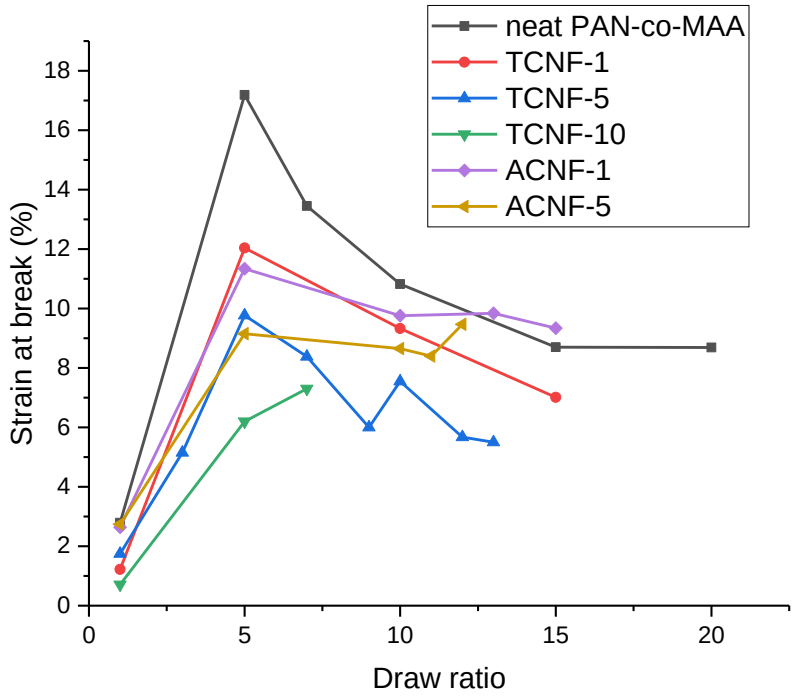

Figure 5.4. Strain at break with respect to draw ratio for a 1x ADR fiber with no cold drawing showing an initial increase in strain at break with drawing, but a leveling out at higher draw ratios.

5.3.4 Effect of drawing on tensile strength and elastic modulus

It was found there was a trend of increasing tensile strength and elastic modulus with increasing hot draw ratio for the fibers under the same ADR and cold draw ratio conditions. Higher total draw ratios did not lead to the highest properties in fact the fibers with an ADR of 1x typically had a lower maximum TDR compared to 2x and 3x ADR fibers, but the highest mechanical properties (**Appendix D Table D.1-D.15**). The tensile

strength and elastic modulus of the fibers with respect to draw ratio can be seen in **Figures 5.5** and **5.6**, respectively.

In a lot of published work on fillers and nanocellulose fillers containing fibers authors will compare the properties of the neat fiber and composite fiber at the same TDR or under small variations in processing conditions. In this work we undergo many more processing parameters to give a better overview if CNF can be utilized as a mechanical filler since processing has a large effect on the resulting properties. Also neat polymer fibers can typically be drawn to a higher draw ratio than the composite fibers and by comparing samples at the same draw ratio can lead to inaccurate representation of how well the fillers can reinforce the fibers when trying to make fibers with the best mechanical properties. Such as in a paper by Lee et al. [67] incorporated 40 wt% CNC into PVA and compared all the fibers mechanical properties at a TDR of 6. Their results indicated the PVA with 40 wt% CNC had a tensile strength of 880 MPa and an elastic modulus of 29.9 GPa, which is ~75% higher tensile strength and 200% higher elastic modulus than the neat PVA at the same draw ratio of 6 [67]. Akira Isogai's group has shown that PVA fibers could be drawn to TDR of 20 in their work and their neat PVA had a tensile strength of ~1.6 GPa and an elastic modulus of 45 GPa, which shows that the properties reached at a TDR of 6 in the previous study is likely not the maximum possible [68].

We will have a short discussion of the mechanical properties of our fibers comparing them at the same draw ratio. We will then shift our focus onto the fibers with the best mechanical properties since this is more important for adaptation of this technology by industry. The tensile strength and elastic modulus of the fibers with respect to draw ratio

can be seen in **Figures 5.5** and **5.6**, respectively, and the corresponding data can be found in **Appendix D Tables D.1-D.15**. Depending on the ADR, CDR, and HDR different interpretations can arise on whether the CNF acts as a mechanical reinforcement. We can see at the same TDR, TCNF-1, ACNF-1, and ACNF-5 fibers can have higher tensile strength then the neat PAN-co-MAA fiber. Also at the same TDR, all the composite fibers can have higher elastic modulus than the neat PAN-co-MAA fiber.

To further this discussion we will look at 1 processing condition; the 1x ADR fiber with 1x CDR, and a TDR of 10x, and the fibers with the highest tensile strength and elastic modulus produced with 1x ADR with 1x CDR. We can see in **Table 5.5** the percent change in the tensile strength and elastic modulus of the fibers compared to the neat PAN-co-MAA sample at a TDR of 10x and the fibers with the highest properties. We can see that for the ACNF-1 sample at a TDR of 10 it has a 49% higher tensile strength and 23% higher elastic modulus than the neat PAN-co-MAA. With these results it shows that ACNF loading at 1 wt% is a great reinforcement material, but when we look at these same fibers when drawn for the highest properties the ACNF-1 fiber only has a 9% increase in tensile strength and 2% decrease in elastic modulus when compared to the neat PAN-co-MAA fiber. Similarly, the TCNF-1 sample at a TDR of 10x has 20 % higher tensile strength and a 17% higher elastic modulus than the neat PAN-co-MAA, which is still a very good increase at 1 wt% TCNF loading. Though when we look at the TCNF-1 and neat PAN-co-MAA fibers drawn for the highest properties, the TCNF-1 had a 32% lower tensile strength and 9 % lower elastic modulus compared to the neat PAN-co-MAA fiber. These results show that comparing fibers at similar TDR can be misleading for the actual reinforcement and can

actually show the opposite of what will occur when the fibers are processed for the highest properties.

It was also found that depending on the processing parameters such as ADR, CDR, and CNF loading resulted in whether CNF had a reinforcement effect on PAN-co-MAA and which functionalization actually performs better when comparing the maximum TDR fibers' mechanical properties at each composition (**Table 5.6**). If we look at **Table 5.6** and don't take into account of 3x ADR with 1x CDR fiber since we did not have enough material to fully draw the neat PAN-co-MAA sample. We can note that neat PAN-co-MAA had the best tensile strength in 3 out of 5 processing conditions, while ACNF-1 performed best in 2 out of 5 processing conditions. So depending on how the fibers are processed it can be interpreted on whether ACNF actually has reinforcement effect. This indicates that looking at only 1 drawing condition can give a false interpretation of reinforcement capabiltiies of fillers. We can also note from this table that the ACNF-1 fiber with an ADR of 1x with no cold drawing had the highest tensile strength out of all the fibers and processing conditions with a tensile strength of 1160 MPa compared to the neat PAN-co-MAA tensile strength of 1060 MPa. A p-test was perfromed comparing the ACNF-1 fiber vs neat PAN-co-MAA fiber with the highest tensile strength and it was found the increase was statistically significant with a p-value $\leq$ 0.0001.

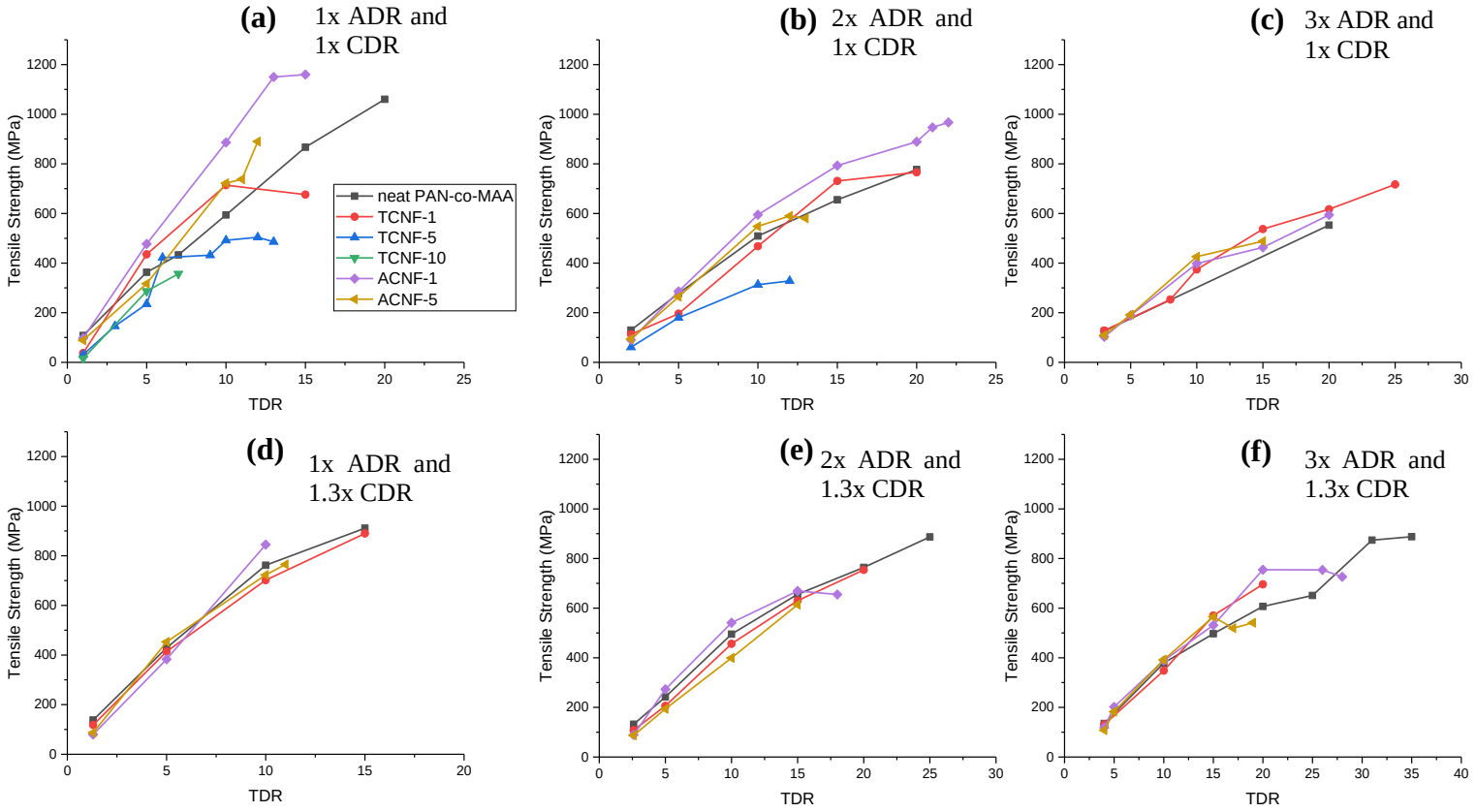

Figure 5.5. Tensile strength of the samples with respect to the total draw ratio (TDR). **(a)** 1x ADR and 1x CDR, **(b)** 2x ADR and 1x CDR, **(c)** 3x ADR and 1x CDR, **(d)** 1x ADR and 1.3x CDR, **(e)** 2x ADR and 1.3x CDR, **(f)** 3x ADR and 1.3x CDR.

Table 5.5. Percent change in tensile strength and elastic modulus for the composite fibers compared the neat PAN-co-MAA at a TDR of 10 and comparing the fibers with the highest mechanical properties. These fibers had an 1x ADR and no cold drawing.

Sample	Percent change in tensile strength for fiber at a TDR=10	Percent change in elastic modulus for fibers at a TDR=10	Percent change in the tensile strength for fibers with highest tensile strength	Percent change in the elastic modulus for fibers with elastic modulus
TCNF-1	20	17	-32	-9
TCNF-5	-17	1	-52	-13
ACNF-1	49	23	9	-2
ACNF-5	22	13	-16	-10

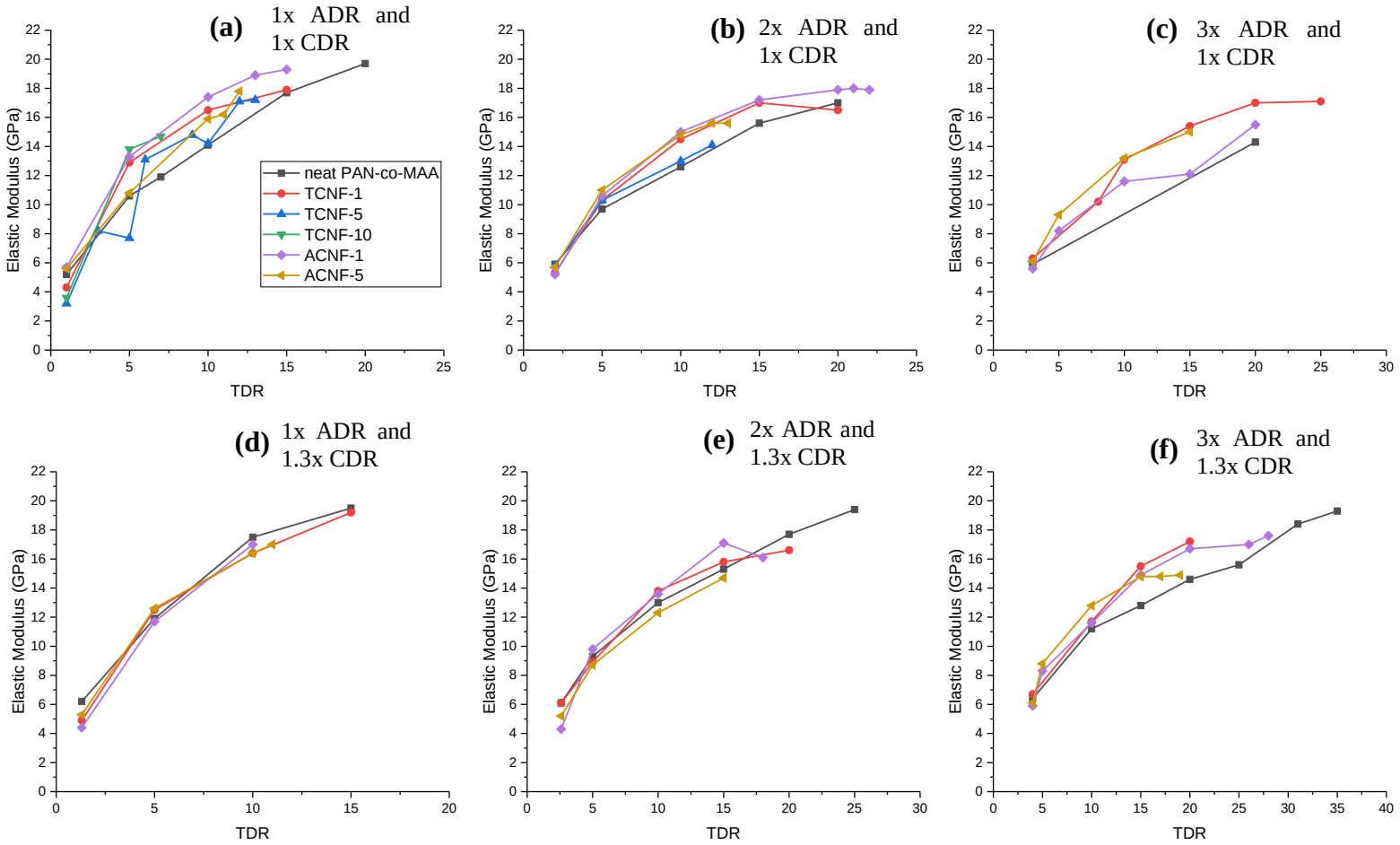

Figure 5.6. Elastic modulus of the samples with respect to TDR. **(a)** 1x ADR and 1x CDR, **(b)** 2x ADR and 1x CDR, **(c)** 3x ADR and 1x CDR, **(d)** 1x ADR and 1.3x CDR, **(e)** 2x ADR and 1.3x CDR, **(f)** 3x ADR and 1.3x CDR.

The only composite fiber with a higher tensile strength than the neat PAN-co-MAA sample, with the highest tensile strength, is the ACNF-1 sample. A plot of the maximum tensile strength values of each fiber composition can be found in **Figure 5.7**. The theoretical strength and elastic modulus are calculated with the isostrain model seen below in **Equation 5.1** where σ_c, σ_f, σ_m, V_f, and V_m is the tensile strength of the composite, tensile strength of the filler, tensile strength of the matrix, volume fraction of filler, and volume fraction of matrix, respectively. **Equation 5.1** can be also used to calculate the elastic modulus by replacing the variable σ with the variable E (elastic modulus). The density of CNF and PAN used was 1.5 g/cm^3 and 1.18 g/cm^3, respectively [171]. The tensile strength of the filler used was 3 GPa, and the tensile strength used for the matrix was the highest strength neat fiber made experimentally (1.06 GPa). The reason this model was used is because fibers are highly drawn materials with maximum strength in 1 direction. Also this model gives the highest theoretical strength, because it assumes the nanofillers are perfectly aligned with the fiber. We can see that ACNF-1 sample actually has a tensile strength higher than the theoretically predicted tensile strength, which should not be possible assuming there are no structural differences between the PAN in the ACNF-1 and the neat PAN-co-MAA. This points towards the ACNF affecting the PAN around the nanofillers in a way that would increase the tensile strength.

$$\sigma_c = \sigma_f V_f + \sigma_m V_m \qquad \textbf{5.1}$$

The predicted elastic modulus with the iso strain model is much higher than our experimental data, and our experimental data actually shows a decrease in elastic modulus

with increasing CNF loading. This is due to that elastic modulus being much more dependent on the orientation of the PAN and nanofiller than tensile strength. Due to the lower drawability of the composite fibers the orientation of the PAN is not has high as in the neat PAN-co-MAA fiber (**Table 5.7**), which would result in elastic modulus because the fiber is majority PAN-co-MAA.

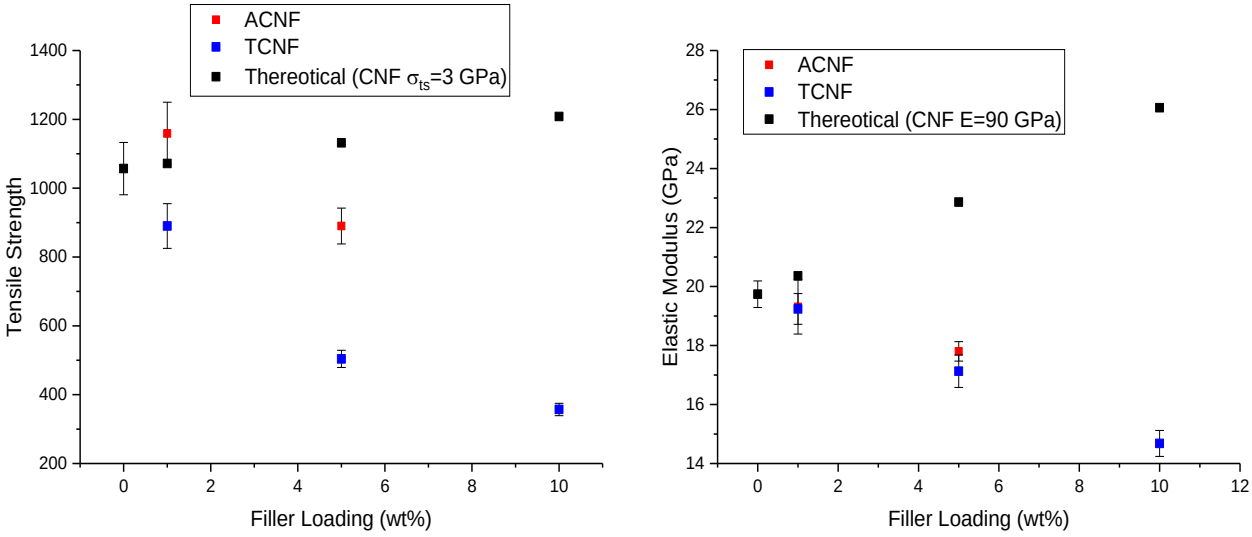

Figure 5.7. Plots showing the fibers with the highest **(Left)** Tensile strength, and **(Right)** elastic modulus.

Table 5.6. Differences between tensile strength and elastic modulus at maximum TDR of fibers depending on the ADR and CDR of the fibers.

Sample	ADR-CDR-HDR=TDR	Tensile strength at maximum TDR (MPa)	Elastic Modulus at maximum TDR (GPa)	ADR-CDR-HDR=TDR	Tensile strength at maximum TDR (MPa)	Elastic Modulus at maximum TDR (GPa)
Neat PAN-co-MAA	1x-1x-20x=20x	1060 ± 76	19.7 ± 0.5	1x-1.3x-11.5x=15x	911 ± 96	19.5 ± 1.0
TCNF-1	1x-1x-15x=20x	676 ± 49	17.9 ± 0.6	1x-1.3x-11.5x=15x	890 ± 65	19.2 ± 0.5
TCNF-5	1x-1x-13x=13x	486 ± 45	17.2 ± 1.1	N/A	N/A	NA
TCNF-10	1x-1x-7x=7x	357 ± 18	14.7 ± 0.4	N/A	N/A	N/A
ACNF-1	1x-1x-15x=15x	1160 ± 91	19.3 ± 0.9	1x-1.3x-7.7x=10x	845 ± 50	17.0 ± 0.6
ACNF-5	1x-1x-12x=12x	890 ± 52	17.8 ± 0.3	1x-1.3x-11x=11x	765 ± 94	17.0 ± 0.8
Neat PAN-co-MAA	2x-1x-10x=20x	777 ± 78	17.0 ± 0.8	2x-1.3x-9.6x=25x	887 ± 76	19.4 ± 0.6 16.6 ± 0.9
TCNF-1	2x-1x-10x=20x	766 ± 45	16.5 ± 0.7	2x-1.3x-7.7x=20x	754 ± 81	
TCNF-5	2x-1x-6x=12x	328 ± 30	14.1 ± 0.6	N/A	N/A	N/A
TCNF-10	N/A	N/A	N/A	N/A	N/A	N/A
ACNF-1	2x-1x-11x=22x	967 ± 57	17.9 ± 0.3	2x-1.3x-6.9x=18x	655 ± 52	16.1 ± 0.7
ACNF-5	2x-1x-6.5x=13.	590 ± 44	15.6 ± 0.5	2x-1.3x-5.8x=15x	638 ± 22	15.2 ± 0.3
Neat PAN-co-MAA	N/A	N/A	N/A	3x-1.3x-9x=35x	888 ± 52	19.3 ± 0.4
TCNF-1	3x-1x-8.3x=25x	717 ± 46	17.1 ± 0.8	3x-1.3x-5.1x=20x	696 ± 80	17.2 ± 1.1
TCNF-5	N/A	N/A	N/A	N/A	N/A	N/A
TCNF-10	N/A	N/A	N/A	N/A	N/A	N/A
ACNF-1	3x-1x-6.7x=20x	594 ± 51	15.5 ± 0.7	3x-1.3x-7.2x=28x	726 ± 51	17.6 ± 1.2
ACNF-5	3x-1x-5x=15x	488 ± 27	15.0 ± 0.4	3x-1.3x-4.9x=19x	541 ± 36	14.9 ± 0.4

Table 5.7. Table of structural parameters measured by WAXD of fibers with highest elastic modulus.

Sample	ADR-CDR-HDR=TDR	Orientation of PAN	Crystal Size of PAN (nm)	Crystallinity of PAN (%)	Orientation of CNF
neat PAN-co-MAA	1x-1x-20x=20x	0.87	13	65	N/A
TCNF-1	1x-1.3x-11.5x=15x	0.83	12	56	N/A
TCNF-5	1x-1x-13x=13x	0.80	8.8	63	0.83
TCNF-10	1x-1x-7x=7x	0.75	10	56	0.74
ACNF-1	1x-1x-15x=15x	0.81	9.9	59	N/A
ACNF-5	1x-1x-12x=12x	0.82	8.7	65	0.60

Looking at the tensile strengths in **Table 5.6** we can also see that TCNF-1 performs better than ACNF-1 in 3 out of 6 processing routes, and TCNF-5 performs worse than ACNF-5 in all processing routes. This is surprising that TCNF-1 performs better than ACNF-1 in half the processing routes since the max TCNF-1 tensile strength was 890 MPa, which is much lower than the maximum of ACNF-1 (1160 MPa). It is hard to dictate a trend for the processing conditions, because occasionally cold drawn samples results in the fiber having higher properties, and occasionally having a fiber with an ADR of 1 or 2 results in fibers with the best properties. It is possible that not all the samples were fully drawn to their maximum state resulting in the fiber not achieving their maximum properties thus making trends hard to find. It is known there are process variabilities when manufacturing samples and can lead to mechanical property variations, which can cause trends hard to find. One trend is shown in the tensile strength data is that higher CNF loading above 1 wt% leads to a decrease in tensile strength. This is likely due to lower

drawability of the fibers at higher CNF loadings, and aggregation of fillers acting as defect points.

The neat PAN-co-MAA sample (1x-1x-20x) had the highest modulus out of all the samples even though the ACNF-1 sample (1x-1x-15x) had the highest tensile strength. The neat PAN sample (1x-1x-20x) had an elastic modulus of 19.7 GPa and the ACNF-1 sample (1x-1x-15x) had an elastic modulus of 19.3 GPa. A p-test was performed, and it was found that the p-value = 0.0233, which is statistically significant assuming we use a p-value $\leq$ 0.05 as statistically significant. This elastic modulus difference is due to the higher hot draw ratio of this fiber resulting in higher orientation of the PAN crystals and will be discussed later. It is well known that higher orientation results in higher elastic modulus. The tensile strength is also affected by the orientation and crystallinity which is affected by drawing, but tensile strength is also related to other factors such as defects within the fibers.

5.3.5 WAXD comparison of fibers

WAXD was performed on our fiber samples to determine whether there were any changes in the PAN structure that were resulting in the different properties between the neat PAN-co-MAA sample and the composite samples. The WAXD integrated radial scan of the samples can be seen in **Figure 5.8**. The PAN peak can be seen at a $2\theta=16.7°$ for all the samples and for sample with 5 wt% and higher loadings of CNF a peak at $2\theta=22.6°$ associated with cellulose I can be seen. The 2-D WAXD pattern of the samples with the highest tensile strength can be seen in **Figure 5.9** and the $2\theta=22.6°$ for cellulose I can be

more easily in these 2-D WAXD patterns than in the WAXD radial scan. This appearance of the cellulose I peak supports that there is cellulose in our sample.

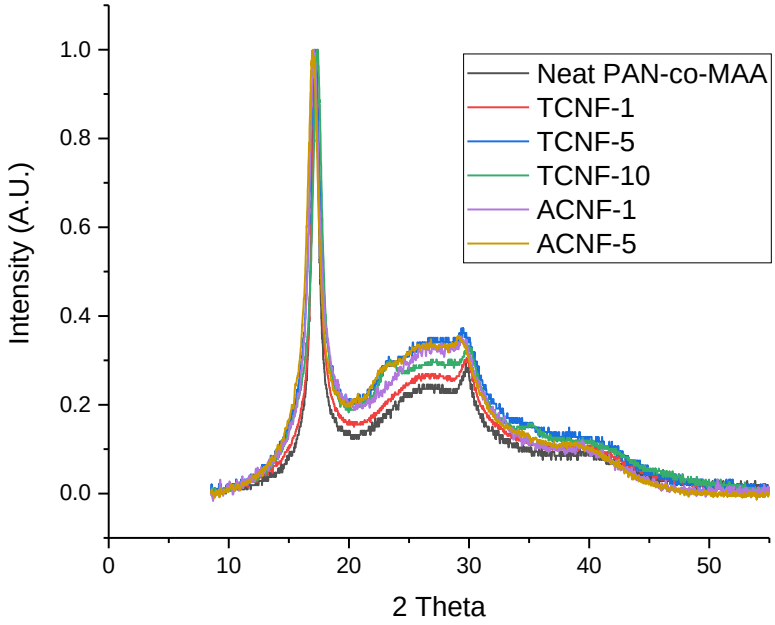

Figure 5.8. WAXD integrated radial scan of the neat PAN-co-MAA and composite fiber samples that displayed the highest elastic modulus for each composition.

The structural parameters of the fibers measured by WAXD for the samples with the highest tensile strengths can be seen in in **Table 5.7**. It can be seen that the neat PAN-co-MAA sample has a crystallinity of 65%, which is higher than all the samples except ACNF-5, but all these values are within experimental error except for the TCNF-1 and TCNF-10 samples both with a crystallinity of 56%. This indicates that PAN crystallinity is not a significant factor for the higher tensile strength of the ACNF-1 sample as compared to the neat PAN-co-MAA sample. So, the higher tensile strength of the ACNF-1 is derived from the beneficial properties due to the addition of ACNF. Even accounting for ACNF

tensile strength of 3 GPa the ACNF-1 tensile strength (1160 MPa) is still above the theoretical tensile strength of the composite predicted with the iso-strain model (1075 MPa). The tensile strength of the ACNF would have to be 16 GPa for the iso-strain model to predict the tensile strength of the ACNF-1 sample, which is even higher than the tensile strength of an idealized cellulose structure for CNC (7.5 GPa). This points towards a synergistic effect between the ACNF and the PAN-co-MAA resulting in the higher tensile strength. It has been previously theorized by other authors that the amorphous polymer in the proximity of the CNF is more ordered and oriented in the fiber direction than the rest of the amorphous polymer leading to increased mechanical properties [68]. The lower tensile strength of the other composite samples compared to the neat PAN-co-MAA could be due to aggregates of CNF acting as stress concentrators.

Among all the samples, the neat PAN-co-MAA has the highest PAN orientation, and higher orientation leads to higher elastic modulus [172]. This explains why the neat PAN-co-MAA sample had the highest elastic modulus out of all the samples. The higher orientation of PAN in these samples have a trend of higher elastic modulus as can be seen in **Figure 5.10**.

It can be noted that the neat PAN-co-MAA has the largest crystal size, and with increasing CNF loading the crystal size typically decreases except for the TCNF-10 sample which has crystal size larger than the TCNF-5 sample. This discrepancy for the TCNF-10 could be due to the different drawing process of using an air oven instead of a glycerol bath, and glycerol is a well known plasticizer. The smaller crystal size with increasing CNF loading could be due to the CNF acting as a blocker when the PAN crystal tries to grow

and runs into a CNF. Another possible reason for the smaller crystal size could also result from the lower drawing temperatures used in the polymer composite samples, because this would decrease the mobility of the PAN to reorganize themselves.

Figure 5.9. WAXD 2-D patterns of the fiber samples with the highest elastic modulus for each composition. The red arrows points to 2θ=22.6° indicating presence of cellulose I.

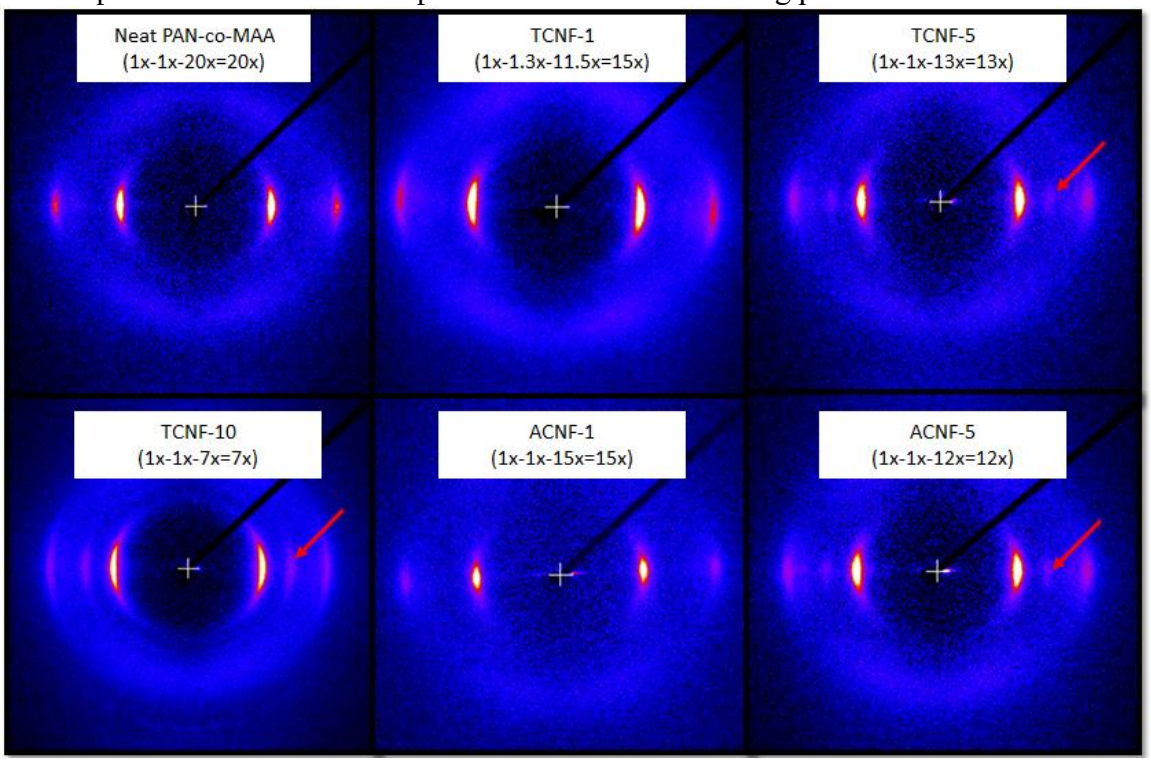

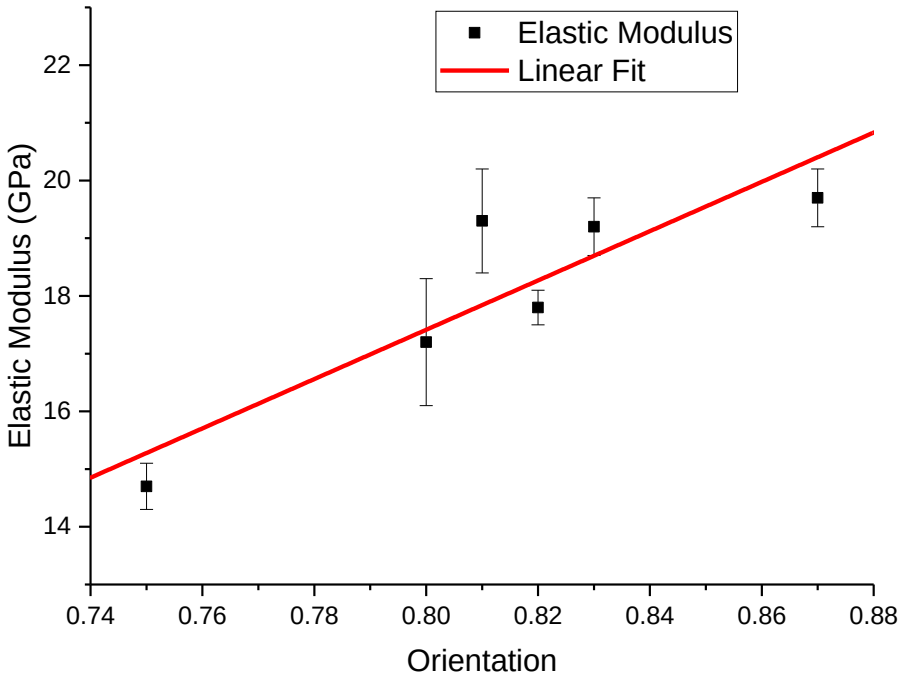

Figure 5.10. Graph showing the trend of increasing elastic modulus with increasing PAN orientation data each data plotted are the fibers with the highest elastic modulus for each fiber composition. Samples of the data plotted here can be seen in **Figure 5.8 & 5.9**.

5.4 Conclusions

Up to 10 wt% CNF was incorporated into PAN-co-MAA fiber through a gel spinning process, these fibers were then continuously post drawn. The previous highest reported solution spun CNF loaded fiber that was continuously post drawn had 1 wt% CNF loading in PVA. It was found that the TCNF had a much larger effect on rheology than the ACNF. Likely there is a stronger percolation network forming in the TCNF suspension than the ACNF suspensions. It was found that the higher CNF loaded sample had to be hot drawn at lower temperatures. Interestingly when the samples were drawn the strain at break could increase depending on the CNF loading and the ADR. It was shown that even the

neat PAN-co-MAA sample could experience an increase strain at break with drawing. This indicates that it could be polymer behaviour or filler interactions for why the strain at break increases when the composite fibers are drawn.

The ACNF-1 sample with the highest tensile strength had a ~10% higher tensile strength than the neat PAN-co-MAA sample with the highest tensile strength. A p-test was conducted and a p-value ≤ 0.0001 was calculated indicating that this increase in tensile strength is statistically significant. The crystallinity of the ACNF-1 and neat PAN-co-MAA sample was found to be similar, so this increase should not be due to higher PAN crystallinity in the ACNF-1 fiber

It was also found that the all the composite samples had lower maximum TDR than the neat PAN-co-MAA fiber. The neat PAN-co-MAA fiber had the highest elastic modulus, and it was found that the orientation of PAN was highest in the neat PAN-co-MAA fiber. This higher orientation is likely a factor for the higher elastic modulus compared to all the composite fiber samples.

CHAPTER 6. CONLCUSIONS AND RECOMMENDATIONS FOR FUTURE WORK

6.1 Conclusions

This research looks at the effect of high loading of nanocellulose in a PAN matrix in film and fiber form. The effect nanocellulose has on the mechanical properties of the resulting films and fibers as well as the effect it has on the stabilization kinetics was investigated. The effect the nanocellulose has on the rheological properties of PAN were also determined. Modification of surface chemistry was also performed and the effect surface chemistry has on reinforcement was also studied. Key results and conclusions are summarized in the following paragraphs.

PAN-CNC films were made with up to 40 wt% CNC loading through the solution casting process. There was a trend of a relatively linear increase in tensile strength and elastic modulus with increasing CNC loading. These films demonstrated a 68% increase in elastic modulus and a 76% increase in tensile strength at 40 wt% CNC loading and the Tg increased from 92 to 118 °C at 40 wt % CNC loading. These films could be manufactured with up to 40 wt% CNC loading with no change in optical transparency. Fitting the experimental tensile data to a micromechanical model it was determined that the interfacial shear strength between the PAN-co-MAA and the CNC was 27 MPa. Interaction between the MAA copolymerized with the PAN and the CNC was observed. It was found that the viscosity of the PAN-CNC suspensions at low shear rates would increase with time, which was not observed in the neat PAN solution.

The incorporation of CNCs into the PAN films reduced the activation energy of cyclization of PAN by 16% irrespective of CNC loading between 5 and 40 wt%. There was not a significant effect on the oxidation activation energy with the addition of CNCs. Depending on the reaction temperature the reaction rate of stabilization and oxidation can be increased with the addition of CNC. It was also found that CNCs were ~100 °C more thermally stable in the PAN-CNC composite film as compared to neat CNCs either in freeze dried powder or film form.

A quick 1 step sulfonation method of CNF was investigated, and it was found that with as low as 5 minutes of reaction time, significant improvement in dispersibility in DMF and water could be achieved. This method was much quicker than the commonly used TEMPO oxidation method for CNF, and this method is also much quicker than the sulfonated CNF made with periodate oxidized CNF. The TCNF and SCNF could undergo surface chemistry changes when dispersed in DMF. The TCNF would form dimethylammonium carboxyl groups, while the SCNF would form formate groups.

Amination of CNF was performed and the reinforcement properties of the ACNF compared to TCNF in PAN fibers was done. The effect of different processing parameters were studied to see how they affect the resulting fiber properties. It was discovered that the TCNF increased the viscosity of the suspensions significantly more than that of the ACNF. At 1 wt% CNF loading, the PAN-ACNF fibers had 30% higher tensile strength than the PAN-TCNF fibers, and at 5 wt% CNF loading the PAN-ACNF fiber had a 78% higher tensile strength than the PAN-TCNF. The PAN-ACNF fiber at 1 wt% ACNF loading had

a 9% higher tensile strength than that of the neat PAN fiber. A p-test was performed and it was found that this 9% increase in tensile strength is a statistically significant.

6.2 Recommendations

6.2.1 Polymer-CNC Films with Higher CNC loading

It was found that when CNC were incorporated into PAN-co-MAA films that the thermal stability of the CNC increased by ~100 °C, even for CNC loadings as high as 40 wt%. Additional work could be to explore the mechanism for this increased thermal stability, and explore methods to optimize this process in PAN and other polymer systems. If a small addition of polymer significantly increases the thermal stability of the CNC, it could have applications where CNC is desired, but the thermal stability is lacking.

6.2.2 PAN-CNC Films with Lower CNC loading

The decrease in the cyclization activation energy by 16% with the incorporation of 5-40 wt% CNC into PAN-co-MAA could indicate that CNCs act as a catalyst for the cyclization reaction. If this is true, then a small addition of CNCs could be used to reduce the activation energy, and the cost of stabilization of PAN for the production of carbon material. Additional work should be completed to identify and confirm the mechanism/pathway for the drop in the cyclization activation energy from the CNC additions, and then optimize the loading needed.

6.2.3 PAN-CNF Fiber with Higher CNF loading

In the current PAN fiber work there was a reduction in tensile properties after 5 wt% CNF loading, however, it may be possible to increase tensile properties after a critical CNF loading is reached. At this point, the properties will be more dependent on the CNFs

and less on the polymer. In partial support of this, previously reported work found that 90 wt% CNF fibers could be make with a tensile strength of 812 MPa and an elastic modulus of 50.2 GPa. A possible way to increase the CNF loading above the 10 wt% CNF loading in PAN done in **Chapter 5** is by increasing the PAN molecular weight, because less polymer is required to reach the same viscosity needed for spinning. For example, a 247 kg/mol molecular weight PAN-co-MAA ~15g/dL solid content is needed while for a 967 kg/mol molecular weight PAN-co-MAA ~6g/dL is needed for the viscoelastic properties for the neat polymer to be spun. Thus when making 100 ml of solution/suspensions for the 247 kg/mol PAN to make of a 10 wt% CNF loaded fiber, 1.5g of CNF is needed (assuming a final solid content is 15g/dL). In contrast, for the 967 kg/mol PAN, 1.5g of CNF results in a 25 wt% CNF loaded fiber (assuming a final solid content of 6g/dL). Since both suspensions would contain 1.5g of CNF the rheological effect from the CNF on the suspension should be similar, but the higher molecular weight PAN suspension would result in a fiber with a higher wt% CNF.

6.2.4 PAN-CNF Sheath-Core fiber

PAN(sheath)-CNF(core) sheath-core fibers were attempted to be made, and it is discussed in **Appendix D.** Due to the much lower solid content of the TCNF core compared to the PAN sheath this results in decrease in sheath stability during spinning. This reduction in the sheath stability is due to the diffusion of the solvent in the core to the sheath due to the solvent concentration gradient. This diffusion of solvent lowers the solid content of the sheath and changes the rheological properties, which made fiber spinning more difficult. One possible solution to this problem is instead of a dry-jet wet spinning process to use a

wet spinning process. A wet spinning process does not require the high stability needed to to pass through an air gap also there will be less time for the solvent in the core to diffuse into the sheath before coagulation starts. Another suggestion is using a higher molecular polymer in the sheath like 967 kg/mol PAN the high solvent of the content of the core will have less effect on the sheath since there is a lower drive for diffusion of solvent from the core to sheath since the concentration gradient is not as high as when using 247kg/mol PAN.

6.2.5 Fiber with Below 1x As Spun Draw Ratio

It was found that typically the 1x as spun draw ratio fiber when fully processed produced fibers with higher tensile strength and elastic modulus than the 2x as spun draw ratio fibers, and the 2x as spun draw ratio fibers had higher properties than the 3x as spun draw ratio fibers. This was trend was found for to occur for the neat PAN-co-MAA fibers and the composite fibers at all CNF loadings. It is hypothesized that the higher hot draw ratio for the fibers spun with a lower as spun draw ratio results in fibers with higher properties. Additional work should explore fibers produced with an as spun draw ratio below 1, and asses the role of as spun draw ratio and hot draw ratio to optimize further improvements in fiber properties.

APPENDIX A: SUPPORTING INFORMATION FOR CHAPTER 2

A.1 Percolation threshold calculation

Percolation threshold [34] was estimated according to **Equation A.1**, with ϕ_c, L, and D being volume fraction for percolation threshold, length of particle, and diameter of particle, respectively.

$$\phi_c = \frac{0.7}{L/D} \quad \textbf{(A.1)}$$

A.2 Wide-Angle Characterization Procedure

There was no orientation of the PAN-co-MAA and CNC in the films and it can be determined from the isotropic pattern seem in **Figure A.8**. Qualitative change in crystallinity of the PAN-co-MAA was determined from the integral scan from 2θ=8.5 ° to 2θ=55 °. To qualitatively determine if there are significant change in crystallinity of the PAN-co-MAA in the composite systems relative to the neat PAN-co-MAA, the composite wide-angle X-ray diffraction (WAXD) integral scans were attempted to be recreated from the neat PAN-co-MAA and neat CNC WAXD integral scans. This is based on the idea that a sample's diffraction pattern is an additive sum of all its separate parts [173]. This was done by **Equation A.2** with a solver that minimized the sum of the squared error, E, by solving for fitting parameters X_1 and X_2 simultaneously. With Y_1, Y_2, and Y_3 being intensity of the neat CNC spectra, intensity of the neat PAN-co-MAA spectra, and the intensity of the composite spectra respectively. Each composite's solution of X_1 and X_2 was solved independently of other composites.

$$E = \sum_{2\theta=8.5^\circ}^{2\theta=55^\circ} (Y_3(2\theta) - (Y_1(2\theta)X_1 + Y_2(2\theta)X_2))^2 \quad \textbf{(A.2)}$$

The intensity of a component is linear with respect to the volume of the component [174]. Since an x-ray diffraction pattern is an additive sum of its separate parts the amount of intensity a component gives off in a composite should be same once we normalize to volume fraction of that component in the composite. Using **Equation A.3** we assessed the consistency of the rule of mixture curves. The ϕ_1, ϕ_2, i_1, and i_2 are the volume fraction of CNC, volume fraction of PAN-co-MAA, intensity coefficient of CNC, and intensity coefficient of PAN-co-MAA, respectively. The volume fraction of CNC in the films can be found in **Table 2.1**. The Y_1, Y_2, X_1, and X_2 are the same as **Equation A.2** for each composite. The i_1 and i_2 should be the same for all composites, because it is a material property of the CNC and PAN-co-MAA. The variables i_1 and i_2 were solved simultaneously for all composite with the least squared method.

$$\frac{CNC\ Intensity}{Total\ Itensity} = \sum_{2\theta=8.5^\circ}^{2\theta=55^\circ} \frac{Y_1(2\theta)X_1}{(Y_1(2\theta)X_1+Y_2(2\theta)X_2)} = \frac{\emptyset_1 i_2}{\emptyset_1 i_1+\emptyset_2 i_2} \quad \textbf{(A.3)}$$

A.3 Wide Angle X-ray Result

WAXD patterns can be seen in **Figure A.8**. PAN has a very distinct diffraction peak around 2θ=16.7°, and CNC has distinct diffraction peaks around 2θ=20.4° for cellulose II and 2θ= 22.6° for cellulose I [107, 139, 140]. CNCs produced at the Forest Product Laboratory are known to contain both cellulose I and II. The cellulose peaks can be seen more distinctly in the WAXD patterns as the CNC loading is increased. From the WAXD patterns it was determined through the azimuthal scan that there was no orientation for the CNC or PAN-co-MAA, which is expected because the films were made by solution casting without applying any shear. In an attempt to determine crystallinity of the PAN, peak deconvolution with the Hinrichsen method [175] and the Gupta and Singhal method [140] was employed.

The two methods showed very inconsistent results due to the high amount of overlap of the neat PAN-co-MAA and neat CNC pattern, the pattern of each can be seen in **Figure A.9 (a)** and **(g)**. Since these two methods gave inconclusive results, the composite WAXD patterns were attempted to be recreated with the neat PAN-co-MAA and neat CNC WAXD patterns to qualitatively determine if there was significant change in PAN crystallinity with **Equation A.2**. The process of making the composites should not structurally change the CNCs meaning its WAXD pattern shape should not change between the CNC film and in the composite. The reason for this is because the CNC is not soluble in any of the materials used, and the temperatures used in the process should not be high enough to cause any structural changes. The experimental integrated radial scans of the films and rule of mixture integrated radial scan pattern made with the neat PAN-co-MAA and neat CNC patterns with **Equation A.2** can be seen in **Figure A.9**. It can be seen that the experimental and rule of mixture graphs of the composite are very similar indicating qualitatively that there is not much change in the PAN-co-MAA crystallinity between the composite and neat sample. If there was significant change to the PAN-co-MAA structure in the composites, the composites pattern would not be able to be reproduced with the addition of the neat PAN-co-MAA and neat CNC WAXD patterns. To further check the accuracy of these rule of mixture graphs **Equation A.3** was applied for the CNC intensity. The solved i_1 and i_2 gave an equation with an R^2=0.997 to our rule of mixture cellulose intensity divided by total intensity (**Figure A.10**). This allows us to know the rule of mixture graphs are being produced with the consistent ratios of PAN and CNC intensities relative to the CNC volume percent in the films.

Previously it was shown that the addition of 10 wt% CNC in PAN-co-MAA when spun into a fiber with a total draw ratio (TDR) of 10, increased the crystallinity of the PAN-co-MAA from 50 to 62 % [41]. Though there did not seem to be significant change in crystallinity in our current work, it has been seen in previous studies that the addition of fillers into polymers can increase or decrease the crystallinity of the polymer. The fillers can act as a crystallization nucleation point which would increase final crystallinity, but the addition of filler can also decrease the chain mobility of the polymer which can decrease the final crystallinity. These competing factors will dictate how the addition of fillers will influence the final crystallinity of the polymer [58, 176, 177]. From our results and the previous results of PAN-co-MAA/CNC fibers, it is possible that CNC act as a nucleation point for crystallization of PAN-co-MAA. The high shear during fiber spinning reduces the effect of the decrease in chain mobility caused by the CNCs, while still allowing the CNCs to act as nucleation points. In our study because of the solution casting method it is possible the effect of CNCs acting as nucleation points was neutralized by the CNC reducing the chain mobility of the polymer, thus leading to no observable significant change in crystallinity of the films.

A.4 Solution/Suspensions Making Procedure Development

The solution/suspensions made and reported in the **Chapter 2** were made with a target solid content of 3.7 wt%. Before deciding to use 3.7 wt% solid content solution/suspensions for the work in **Chapter 2**, 10 wt% solid content solution/suspensions were originally made followed by 7 wt% solid content solution/suspensions. The 10 wt% solution/suspensions could be made up to 10 wt% CNC loading, but at 20 wt% CNC

loading air bubbles could not be removed due to the high viscosity, so homogenous films could not be made. To reduce the viscosity, we reduce the solid content down to 7 wt%, but at 40 wt% CNC loading, the air bubbles could not be removed. This resulted in making films from solution/suspension with a solid content of 3.7 wt%, which had a viscosity low enough that the air bubbles could to be removed at 40 wt% CNC loading.

A.5 Film Making Procedure Development

The final procedure that was decided to be used was solution casting the solution/suspensions in a glass mold 4 hours after the solution/suspensions were made in a 70 °C oven with air circulation. Other procedures were tried such as in a 70 °C oven with no air circulation, but this resulted in large amount of solvent in the oven due to evaporation and condensation. This also resulted in the occasional solvent condensation to drop on the film resulting in nonhomogeneous films. We also tried using an oven under vacuum at 70 °C, but this could result in air bubbles forming in solution/suspensions leading to bubbles in the film so this process was also not used.

The reason the films were cast 4 hours after the solution/suspensions were made was because we noticed the viscosity of the suspensions would change over time, and we were not sure how this would affect the properties of the films. Originally films were made without taking into account how old the solution/suspensions were. Since this could have resulted in properties changes all new films were made and tested once this was noticed.

Another things we had to do was to get rid of the residual stress that were in the films due to the bottom of the film being in contact with the glass while the top of film was not in contact with any surfaces restricting motion during the drying process. If this step was

not done, the films would curl and could not be worked with. Another problem we had was determining how to test these films, because the films with high CNC loadings were difficult to cut into shapes for testing. It was found that by submerging these films in water, and letting it interact with the water over a period of time made the films more flexible and able to be cut with a straight edge instead of random cracks occurring. Though even with this submerging in water process the films had to be slowly cut, when the films were cut with a die (all at once) the samples would crack and a testable tensile sample could not be made. So a cutting apparatus was made that allowed films to be cut with a consistent width, and allowed the film to be cut from top to bottom (not all at once), which resulted in tensile samples that could be tested. From what we learned described here we developed the procedure used in **Chapter 2**.

A.6 Effect of Aged Suspension on Resulting Film Properties

Due to the increase in viscosity of the neat PAN-co-MAA/CNC suspensions over time, there could be change in the resulting film properties. Aging is likely a factor of time, temperature, and concentration of the solution/suspension. To test the effect of aging on the suspensions on the resulting film properties we made a new CNC-20 suspension with the process mentioned in chapter 2, and casted films at 1 hour, 2, 4, 7, 9, 11 days after the solution/suspensions have been made. To reduce the effect of time the films were made thinner than the films made in **Chapter 2**, and dried under vacuum to reduce the time it took for the film to dry. The vacuum oven was also set to 25 °C to reduce the effect of temperature instead of the 70 °C used in the process for **Chapter 2**.

The tensile testing procedure was the same for these films as used in **Chapter 2** except only 4 successful tests were conducted in the aging study. The tensile properties can be found in **Table A.2**. From the data, it can be noted that there is no trend in the change of elastic modulus over aging time. The elastic modulus seems to be related to film thickness (**Figure A.11)**, and that thinner films have higher elastic modulus and this could be related to how thickness is measured. The thickness is measured by a caliper which applies pressure on the film during the measurement. Assuming all films are compressed the same amount when measuring thickness, thinner samples would be compressed more, and this could be a problem if the compression is significant.

For the tensile strength of the CNC-20 samples (**Table A.2)** it was found that there was a slight trend of increasing tensile strength with increasing aging time. With the sample casted for the 1 hr old suspension having a tensile strength of 118 MPa while the film casted from the 11 day old suspension had a tensile strength of 139 MPa (~18% increase). A p-test was performed for these sample and the p-value=0.0377, which indicates this increase in tensile strength is statistically significant. We did not see an obvious trend of changing tensile strength with film thickness (**Figure A.11)**. The increase in tensile strength with increasing aging time can result due to adsorption of polymer onto the CNC surface leadings to stronger polymer and CNC interaction.

We also did WAXD studies on these films to determine if there are any structural changes in these films as a result of solution/suspension aging. The WAXD 2-D pattern can be found in **Figure A.12**, and the integrated radial scan can be found in **Figure A.13**. The WAXD 2-D pattern, and azimuthal scans done indicates that none of the films have any orientation that would contribute to differences in properties. The integrated scan intensity was normalized to the cellulose I peak (2θ=~22.6°). Using fitting the integrated radial scan the PAN crystallinity and PAN crystal size was determined. The PAN crystal size was calculated using the Scherrer equation with the peak fitted at a 2θ=17° [41], and the data can be found in **Table A.2**. It was found that there was no significant change in crystallinity over time. There was a trend of decreasing PAN crystal size of the films casted from the suspensions with increasing aging time This decrease in crystal size could be due to the increase in suspension viscosity with time. This would reduce polymer mobility as the suspension is drying leading to a reduction in the crystal size.

Table A.1. Glass transition and cyclization onset temperature determined by DSC at a heating rate of 10 °C/min in air. DSC curves can be found in **Figure A.7**.

	neat PAN-co-MAA	CNC-5	CNC-10	CNC-20	CNC-30	CNC-40
Tg (°C)	80	86	88	89	94	100
Cyclization onset temperature (°C)	207	211	211	215	221	229

Table A.2. Film properties of CNC-20 casted at different aging times.

Time after the solution/suspension has been made before casting	E (GPa)	σ (MPa)	ε (%)	Width (micron)	Thickness (micron)	Crystallinity (%)	PAN crystal size (nm
1 Hour	5.2 ± 0.1	118 ± 13	2.9 ± 0.4	2814 ± 91	29 ± 1	23	5.8
2 Days	5.3 ± 0	121 ± 4	2.8 ± 0.2	2798 ± 17	30 ± 1	22	5
4 Days	4.8 ± 0.2	130 ± 8	3.5 ± 0.3	2814 ± 28	40 ± 3	21	5
7 Days	5.5 ± 0.3	128 ± 8	3.1 ± 0.4	2778 ± 30	27 ± 5	21	4.7
9 Days	5.0 ± 0.2	128 ± 10	3.4 ± 0.6	2777 ± 83	35 ± 2	22	4.5
11 Days	5.3 ± 0.1	139 ± 9	3.4 ± 0.4	2829 ± 79	32 ± 2	21	4.9

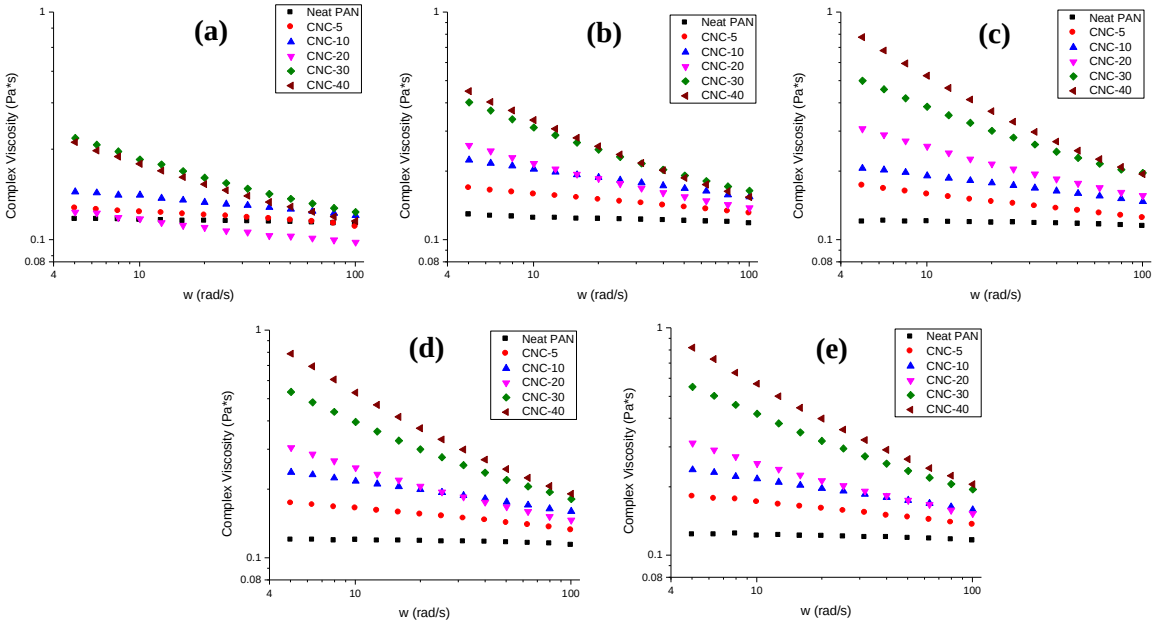

Figure A.1. Complex viscosities of solution/suspensions after **(a)** 4 hours, **(b)** 4 days, **(c)** 14 days, **(d)** 30 days, and **(e)** 90 days after the solution/suspensions have been made.

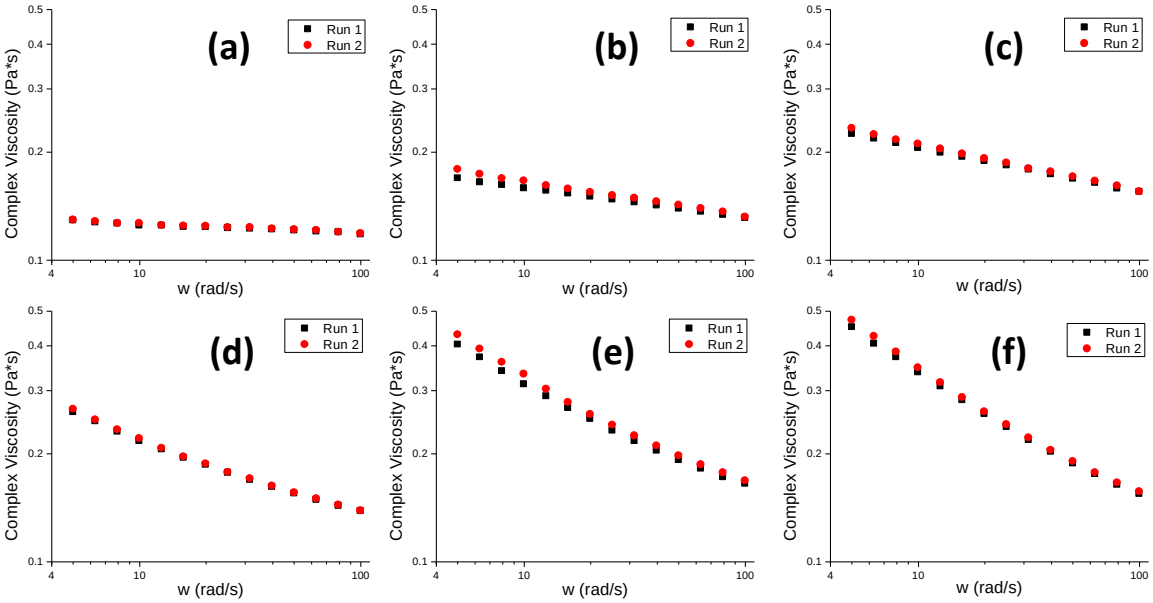

Figure A.2. Comparison between the first and second runs in the rheology aging study of the 4 day old solution/suspensions. Curve shows there is minimal change between the first and second run indicating no change in structure between runs, and little to no solvent evaporation and water absorption.

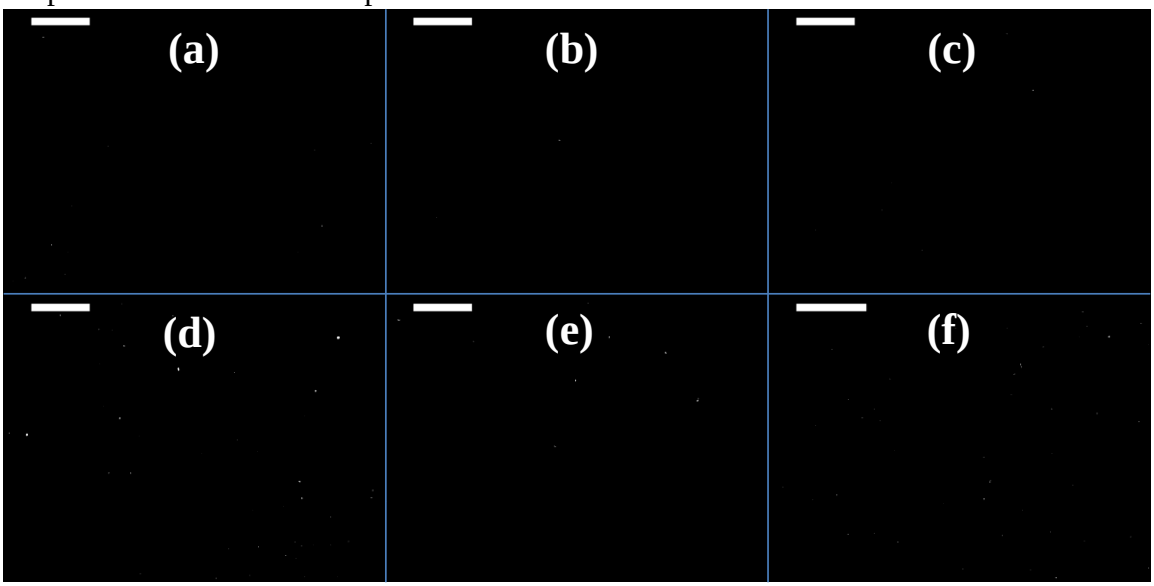

Figure A.3. Representative optical microscopy images of the films under cross polarizers showing little to no birefringence **(a)** Neat PAN-co-MAA, **(b)** CNC-5, **(c)** CNC-10, **(d)** CNC-20, **(e)** CNC-30, **(f)** CNC-40. Scale bar =500 μm.

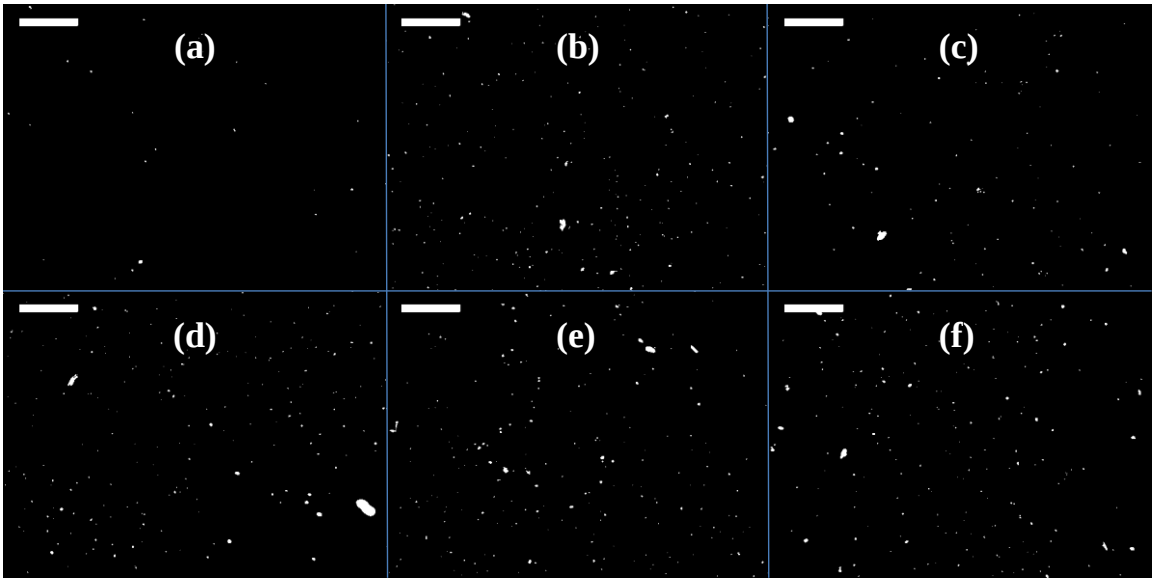

Figure A.4. Optical microscopy images of the films under cross polarizers in areas of the films with high CNC agglomerations (not representative of whole film) **(a)** Neat PAN-co-MAA, **(b)** CNC-5, **(c)** CNC-10, **(d)** CNC-20, **(e)** CNC-30, **(f)** CNC-40. Scale bar =500 μm.

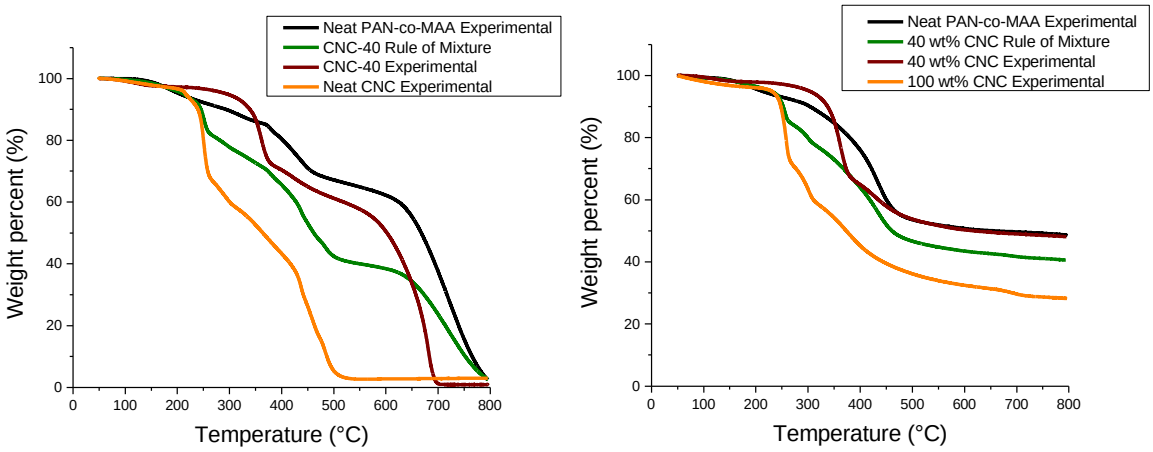

Figure A.5. Experimental and rule of mixture degradation curves of CNC-40 **(Left)** in air, and **(Right)** in nitrogen at a heating rate of 10 °C/min.

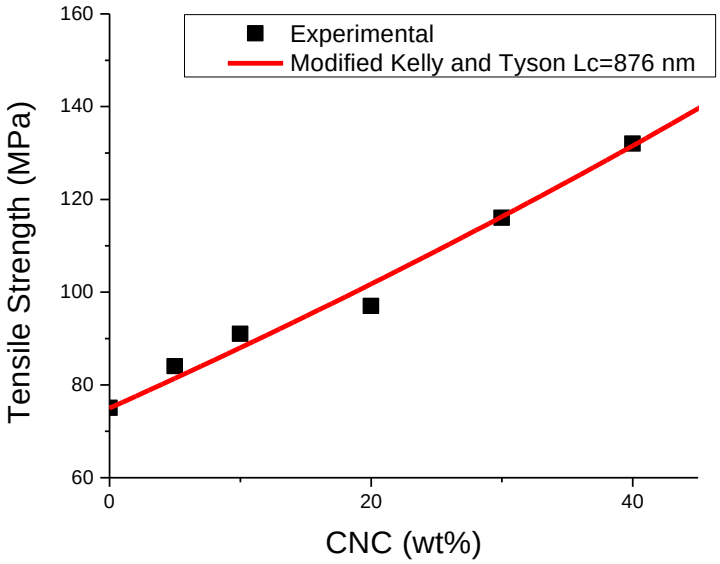

Figure A.6. Experimental tensile strength and the predicted tensile strength from the modified Kelly and Tyson equation with a critical reinforcement length of 876 nm.

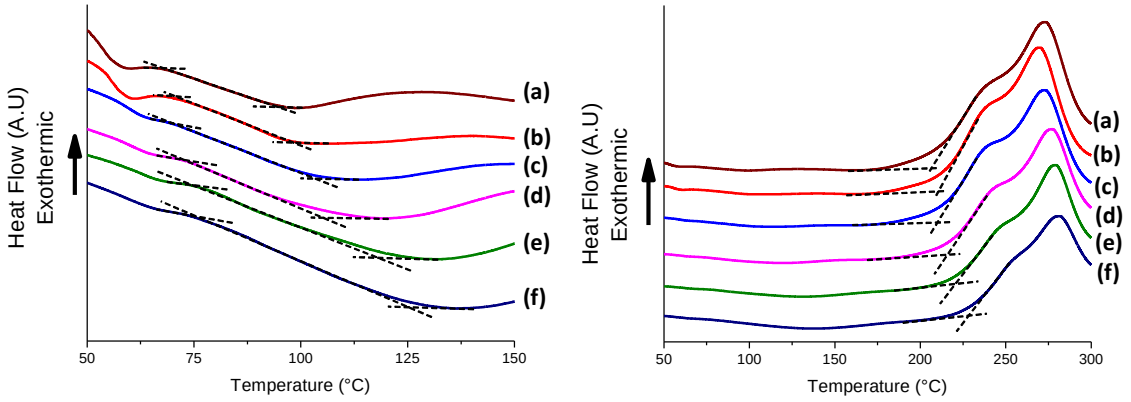

Figure A.7. DSC curves of the films at a heating rate of 10 °C/min in air. **(Left)** Showing the temperature range from 50 to 150 °C (the region where the glass transition occurs). The Tg is the midpoint between where the dash lines intersect for each film. The curve shows a trend of increasing Tg with increasing CNC loading. **(Right)** DSC curve of films from 50 to 300 °C showing an increase in the cyclization onset temperature with increasing CNC loading. The cyclization onset temperature for each film is where the dash lines intersects. **(a)** neat PAN-co-MAA, **(b)** CNC-5, **(c)** CNC-10, **(d)** CNC-20, **(e)** CNC-30, and **(f)** CNC-40. Values of Tg and cyclization onset temperature is listed in **Table A.1**.

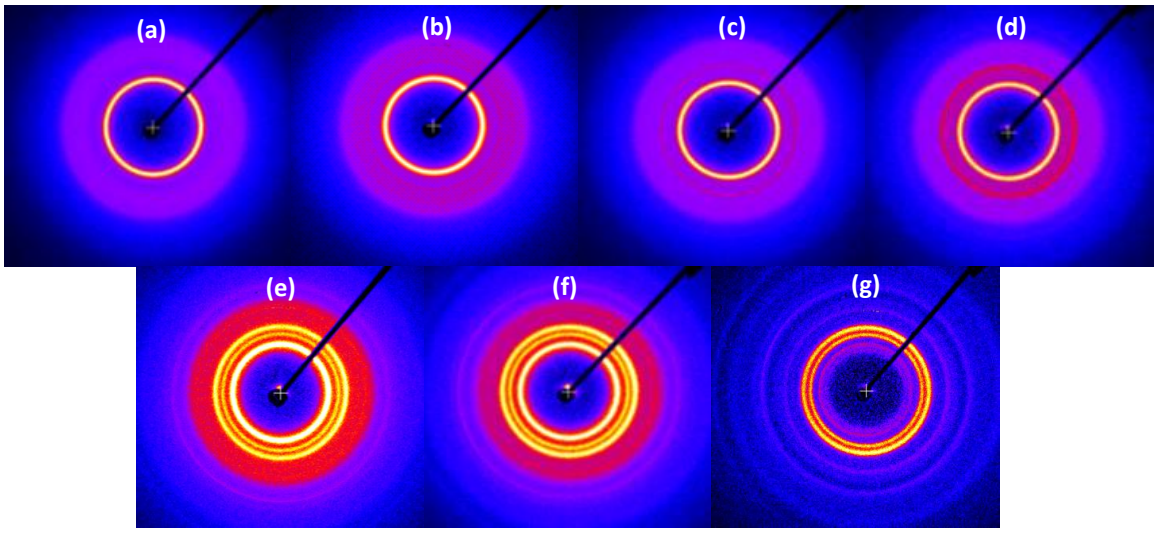

Figure A.8. WAXD patterns of films: **(a)** neat PAN-co-MAA, **(b)** CNC-5, **(c)** CNC-10, **(d)** CNC-20, **(e)** CNC-30, **(f)** CNC-40, **(g)** neat CNC.

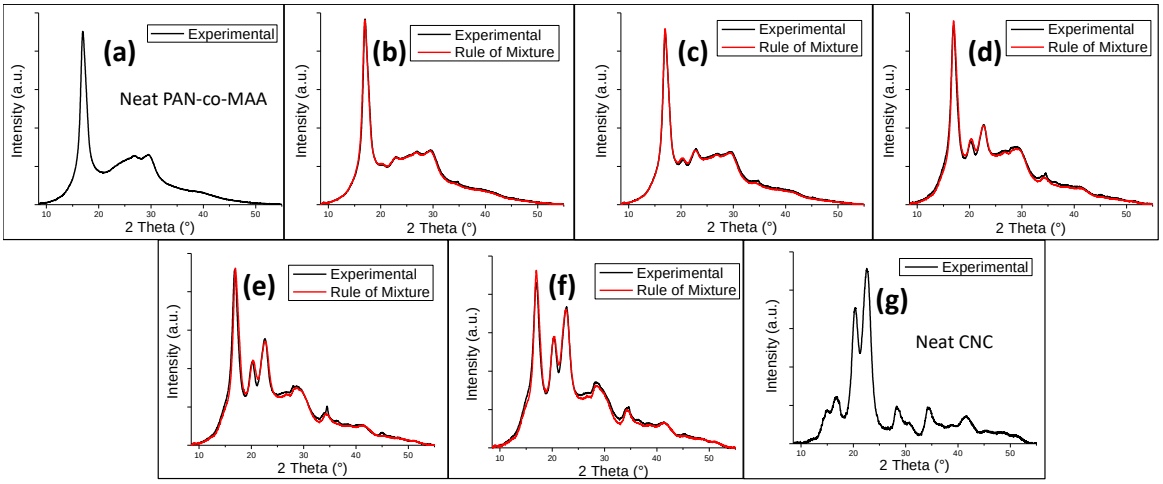

Figure A.9. Experimental and rule of mixture WAXD integrated radial scan of films: **(a)** neat PAN-co-MAA, **(b)** CNC-5, **(c)** CNC-10, **(d)** CNC-20, **(e)** CNC-30, **(f)** CNC-40, **(g)** neat CNC.

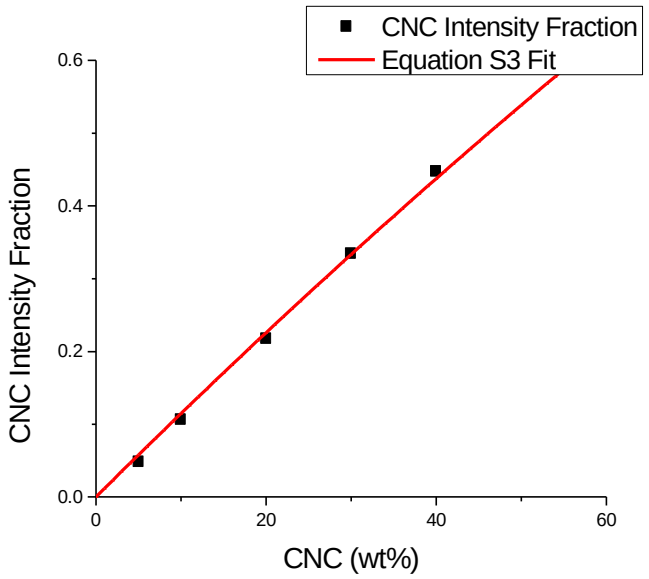

Figure A.10. Fit of Equation A.3 to CNC intensity divided by total intensities of the rule of mixture WAXD patterns solved by Equation A.2 and seen in **Figure A.9**.

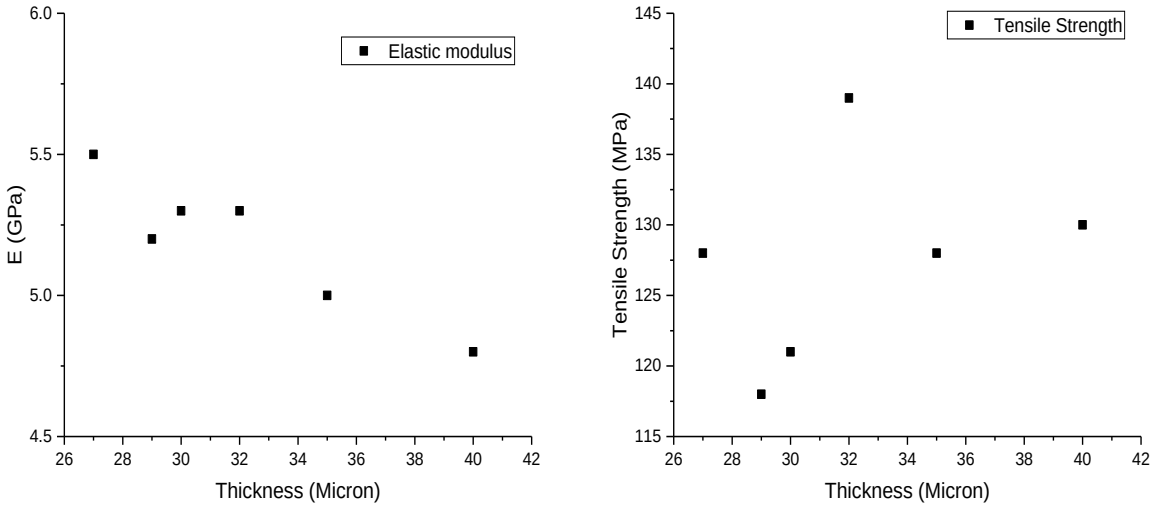

Figure A.11. Relationship of elastic modulus and tensile strength of the CNC-20 films with respect to film thickness showing elastic modulus decreases with increasing film thickness while tensile strength does not seem to be affected much.

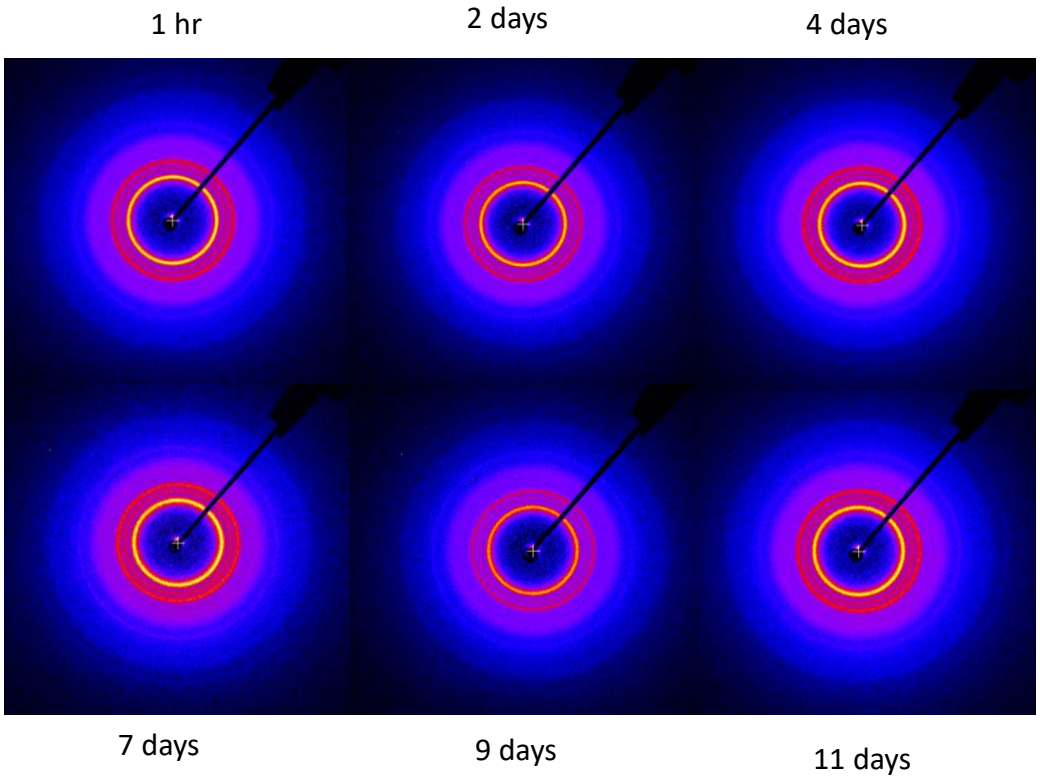

Figure A.12. 2-D WAXD patterns of CNC-20 films casted from aged suspensions.

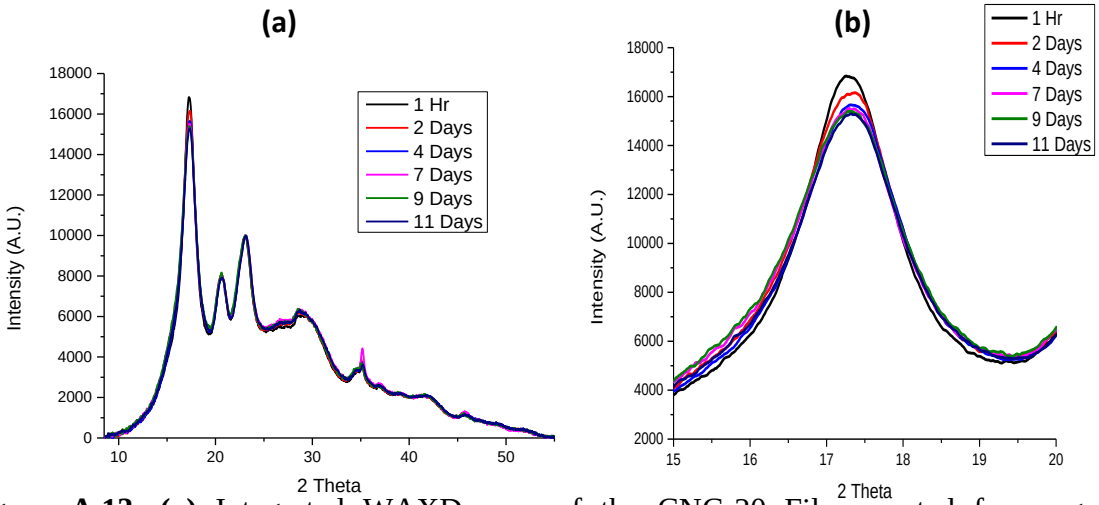

Figure A.13. (a) Integrated WAXD scan of the CNC-20 Films casted from aged suspensions. **(b)** Closer up image of the peak at 2θ=~17° showing a decrease in the peak with increasing aging time. Intensity was normalized to the cellulose I peak (2θ=~22.6°)

APPENDIX B. SUPPORTING INFORMATION FOR CHAPTER 3

B.1 Fibers vs Film Specific Surface Area Calculations

The surface area to volume ratio (SA:V) was calculated for the PAN-co-MAA fiber and film to determine how much higher the fiber's SA:V was than the films'. These calculations were done assuming that the fiber geometry was a long rod, while the films were assumed to be a thin square plate geometry. The equations for the calculations can be found below (**Equation B.1-B.3**). The variables r, L, W, and t are radius of the fiber, length of the fiber, with of the film, and thickness of the film, respectively. It was assumed L>>r and W>>t so in the equations below for the fiber $\frac{2}{r}+\frac{2}{L}$ could be approximated by $\frac{2}{r}$, and for the film $\frac{2}{t}+\frac{4}{W}$ could be approximated by $\frac{2}{t}$. A radius of 7.5 µm was used for the fiber and thickness of 93 and 13 µm was used for the film as measured in **Chapter 2 & 3**.

B.1.1 Fiber surface area to volume ratio (15 micron diameter film):

$$\frac{Surface\ Area}{Volume}=\frac{2\pi rL}{\pi r^2L}+\frac{2\pi r^2}{\pi r^2L}=\frac{2}{r}+\frac{2}{L}\approx\frac{2}{r}=\frac{2}{(7.5\ \mu m)}\approx 0.267\ \mu m^{-1} \quad \textbf{(B.1)}$$

B.1.2 Film surface area to volume ratio (93 micron thick film):

$$\frac{Surface\ Area}{Volume}=\frac{2W^2}{W^2t}+\frac{4Wt}{W^2t}=\frac{2}{t}+\frac{4}{W}\approx\frac{2}{t}=\frac{2}{93\ \mu m}\approx 0.022\ \mu m^{-1} \quad \textbf{(B.2)}$$

B.1.3 Film surface area to volume ratio (13 micron thick film):

$$\frac{Surface\ Area}{Volume}=\frac{2W^2}{W^2t}+\frac{4Wt}{W^2t}=\frac{2}{t}+\frac{4}{W}\approx\frac{2}{t}=\frac{2}{93\ \mu m}\approx 0.022\ \mu m^{-1} \quad \textbf{(B.3)}$$

B.2. FTIR and WAXD Analysis

To investigate if there was any different structure development and/or reaction in the composite samples compared to the neat PAN-co-MAA and neat CNC samples before and after the endo and exothermic reactions, FTIR was done on neat PAN-co-MAA, CNC-40 and neat CNC samples before it was heated and after heating to 160, 310, and 400 °C in nitrogen. Heating the samples to 400 °C in nitrogen followed by heating in air to 400°C and directly in air to 400 °C was also done.

Plots of FTIR of films heated to different temperatures and environment at a heating rate of 10 °C /min are given in **Figure B.2**. For PAN-co-MAA the peak at 3435 cm^{-1} is related to the hydroxyl groups and the 1730 cm^{-1} peak is related to the carbonyl peak of the MAA and neither peak is seen in neat PAN [84, 178]. The peaks at 2926 and 1453 cm^{-1} are related to CH_2, and the 1254 and 1384 cm^{-1} peak is related to CH in both the MAA and PAN. The 2243 cm^{-1} is present due to C≡N in the polyacrylonitrile. The peaks 1664, 1097, and 1064 cm^{-1} are most likely related to residual DMF during processing [84, 85, 179-181]. When the PAN-co-MAA film is heated to 160 °C there is not much change from when it is unheated except for decreases in the peaks related DMF, 1664 ,1097, and 1074 cm^{-1}. Consistent with the DSC results at 310 °C, the FTIR spectra indicates that the cyclization reaction has ended. The FTIR supports this with the C≡N peak decreasing significantly and forming a peak at 1612 cm^{-1} and a shoulder at 1580 cm^{-1} which is related to the C=N and C=C. The CH peak at 1250 cm^{-1} also becomes more prominent due to conversion of CH_2 into CH. The hydroxyl peak related to the MAA goes away, and the peak at 1148 cm^{-1} also develops which did not exist in the film heated to 160°C and is likely CO which formed

from the MAA. From 310 °C to 400 °C there is no new development of peaks, just changes in height of existing peaks. The peak ratio of 1148, 1254, and 1612 cm^{-1} with respect to 1384 cm^{-1} decreases. The small peak still left at 2243 cm^{-1} at 310 °C is no longer present after heating to this temperature. As seen in the DSC, there is large no endothermic or exothermic reaction from 310 °C to 400°C in nitrogen, with primarily the cyclization reaction finishing at a temperature slightly higher than 310 °C. For the film followed by heating to 400 °C in air after being heated to 400 °C in nitrogen there is little change in the FTIR curve compared to the film heated only to 400 °C in nitrogen. The lack of change in the FTIR is likely due to the slow oxygen diffusion into PAN and the low amount of surface area for the PAN. This lack of reaction in the air reruns was also seen in the run in the DSC. The DSC exhibited a low exothermic reaction compared to fibers and thinner films. For the film directly heated in air compared to the film first run in nitrogen then air the FTIR spectra were similar.

For the neat CNC film, the peaks at 3435 and 670 cm^{-1} are related to the hydroxyl groups. The peaks at 2898 and 1384 cm^{-1} are related to CH, 1652 cm^{-1} is bound water and likely some DMF, 1433 cm^{-1} is CH_2 and OCH, 1319 cm^{-1} is CH_2, 1164 cm^{-1} is CO in ring and the bridge oxygen stretch, 1117 cm^{-1} is COC, 1058 cm^{-1} and 1036 cm^{-1} are due to C-O, and 897 cm^{-1} is due to CH or CH_2 [137, 138]. As the neat CNC is heated to 160 °C there is very little difference compared to the unheated CNC. The peak at 1652 cm^{-1} (DMF + water) became more symmetric and shifted to 1645 cm^{-1} (bound water) likely due to the removal of some of the DMF. DMF has a peak at 1664 cm^{-1} which skewed the peak to a higher wave number. After the film was further heated to 310 °C the 3435 cm^{-1} peak

(hydroxyl) narrowed and the 670 cm^{-1} peak decreased due to the dehydration reaction of cellulose. Two very strong peaks developed at 1631 and 1707 cm^{-1} with the 1631 cm^{-1} corresponding to C=C, and the 1707 cm^{-1} most likely representing the C=O that formed due to dehydration. Peaks from 1664 cm^{-1} to 897 cm^{-1} started to lose their distinct shapes and began to merge [96]. A peak also started to develop at 2920 cm^{-1}, which encompassed the peak at 2898 cm^{-1}. Once the film is heated to 400 °C the broad peak that was originally at 2898 cm^{-1} (CH) further developed into 3 peaks at 2970, 2920, and 2854 cm^{-1}. These 3 peaks are associated with different carbon hydrogen bonds. A shoulder started to develop at 1577 cm^{-1} which could be C=C that formed after thermal scission, and a peak at 1440 cm^{-1} might be more apparent due to the addition of OCH that formed after thermal scission. The peaks around 1030 to 1170 cm^{-1} merged and a peak at 1117 cm^{-1} remained. Once this film was rerun in air to 400 °C, the peak at ~800 cm^{-1} disappeared which is associated with ring breathing; this would indicate the benzene ring has broken down. A sharp peak developed at 1658 cm^{-1} with both peaks at 1714 and 1631 cm^{-1}. A small peak also started to develop at 1256 cm^{-1}. The FTIR spectrum for a film which had been run directly in air to 400 °C was similar to the film ran to 400 °C in nitrogen, except for an additional peak at 1658 cm^{-1} that was also seen in the film that was run in nitrogen followed by air. The aromatic ring peak (~800 cm^{-1}), 1631 cm^{-1} and 1714 cm^{-1} peaks were still observed in this sample, unlike for the film that was first heated to 400 °C in nitrogen followed by 400 °C in air where these 3 peaks were no longer present.

The CNC-40 film was analyzed with FTIR as it was heated to different temperatures to determine if it followed a rule of mixture behavior when heated or if there

were different developments. As the film was heated to 160 °C there was not much difference between this sample and the unheated state. Some DMF evaporated off, causing the skew of the peak at 1656 cm^{-1} to disappear and the new peak present at 1645 cm^{-1}, which is the bound water on the cellulose. The same result of DMF evaporation was observed in both the PAN-co-MAA and cellulose films after heating to this temperature. As the film was heated to 310 °C the hydroxyl peak developed a slight skew and the peaks shifted from 3435 cm^{-1} to 3395 cm^{-1}. The reason for the skew and shift is unclear at this temperature. In the neat PAN-co-MAA film the hydroxyl peak completely disappeared, and in the neat CNC the peak narrowed due to dehydration. Peaks that are associated with cellulose such as 1117, 1058, 1036, and 897 cm^{-1} were still present in the CNC-40, while in the neat CNC film these peaks merged and could not be separated from each other at this temperature. This indicates that when CNC is in the PAN/CNC composite, the CNC is more thermally stable than neat CNC film. This conclusion is supported by WAXD data showing that the cellulose structure is still present after heating to this temperature, which will be discussed later. This is further supported by the TGA data seen in **Figure 3.2** where mass loss for CNC-40 occurred at a much higher temperature than neat CNC. This seems to indicate that dehydration and thermal scission may not occur until a higher temperature or at least at a much slower rate, which could be due to the CNC being well dispersed in the polymer matrix. The peaks that are associated with PAN-co-MAA appear to have developed similarly to pure PAN-co-MAA film, with the significant lowering of the C≡N peak at 2243 cm^{-1} and the 1614 and 1250 cm^{-1} peaks developing. The peak at 1383 cm^{-1} started to broaden similar to what happened in pure PAN-co-MAA. At this temperature it

seems that the PAN-co-MAA in the composite still undergoes the same reaction as pure PAN-co-MAA while the neat CNC in the composite seems to be stable with no interaction. In the pure CNC film the dehydration reaction has already proceeded at this temperature. As the CNC-40 films were heated to 400 °C in nitrogen, they showed some differences to the neat components. One significant difference was the hydroxyl peak becoming very weak, though in the DSC between 310 °C and 400 °C there was no endothermic peak showing no dehydration was observed. This indicates that the OH bonds on the cellulose did not form water, and possibly the oxygen reacted with the polyacrylonitrile for the oxidation reaction. While the heating to 400°C did show that CNC were more thermally stable in the composite, it didn't provide evidence of interaction between the CNC and PAN-co-MAA. Along with the lowering of the hydroxyl peak, the peak at 2919 cm^{-1} was reduced significantly, even though it was present in the pure cellulose film. This could have been due to the oxygen forming bonds with the polyacrylonitrile or donating the oxygen to the polyacrylonitrile for oxidation. A strong peak at 1117 cm^{-1} developed in the pure cellulose film, which was the shoulder that forms in the CNC-40 FTIR. This peak was related to the CO which exists at 1150 cm^{-1} in the PAN film. There does seem to be a small peak development at 1150 cm^{-1} in the composite film though not as sharp due to the overlapping 1117 cm^{-1} peak. This shows that the new exothermic peak seen after cyclization in the DSC is in fact a different reaction than the extremely broad peak seen the in pure CNC. The film that was heated to 400 °C in nitrogen and further heated to 400 °C in air had the peak magnitude change relative to the 1384 cm^{-1} peak, with the peaks at 1270, 1605, 1653, 1150, 3410, 2919, and 2858 cm^{-1} increasing. Comparing the film heated

directly in air to the film heated in nitrogen followed by air, the spectra look relatively similar. Comparing the peak ratios with respect to the 1384 cm^{-1} peak, the peaks at 1648, 2858, 2919, and 3410 cm^{-1} increased when the film was ran directly in air.

The WAXD 2-D integral plots of films heated to different temperatures and in different environments at a heating rate of 10 °C/min can be seen in can be seen in **Figure B.3**. PAN has a very distinct diffraction peak around 2θ=16.7°, and the CNC from the USDA Forest Service FPL has distinct diffraction peaks around 2θ=20.4° for cellulose II and 2θ= 22.6° for cellulose I [107, 134, 139, 140]. For the neat PAN-co-MAA without heating the sharp peak at 2θ=16.7° was noted. As the neat PAN-co-MAA is heated to 160 °C there is no real change to the WAXD spectra, which is supported by the DSC and FTIR data. When the film was further heated to 310 °C the peak at 2θ=16.7 disappeared and a very broad peak at 2θ=~20° developed. Continued heating of the sample to 400 °C revealed that the broad peak at 20° started to develop two peaks at 2θ=16° and 25.3°. When the sample was rerun in air after being heated in nitrogen there was not much difference between the WAXD spectra, aside from the peaks at 2θ=16° and 25° getting slightly sharper. Compared to the neat PAN-co-MAA sample ran directly in air there was no significant difference observed. There was also no difference noted in FTIR between these samples.

For the unheated CNC, the distinct diffraction peaks around 2θ=20.4° for cellulose II and 2θ= 22.6° for cellulose I were observed. As the CNC film was heated to 160 °C there was not much change from the unheated state. As the sample was further heated to 310 °C it was observed that peaks at 2θ=20.4° and 2θ=22.6° disappeared, and a broad peak at

2θ=~18.5 developed. Multiple smaller peaks developed at 2θ=23.5°, 25.7°, 32.3°, 33.5°, 34.5°, 46.6°, and 47.6°. Once the film was heated to 400 °C the peak at 2θ=~18.5° shifted to 2θ=~20.5°. When the sample was rerun in air the broad peak shifted further to a higher 2θ value, increasing from 2θ=20.5° to 2θ=23.5°. This increase in 2θ value with further heating would indicate that the structure is densifying. There was no significant difference between the sample ran directly in air and the sample ran in nitrogen followed by air.

For the unheated CNC-40 sample the strong PAN (2θ=16.7°) and cellulose I (2θ=22.6°) and II (2θ=20.4°) peaks can be seen. As it was heated to 160 °C there was no change in the WAXD pattern. When it was further heated to 310 °C the peak associated with PAN (2θ=16.7°) decreased, similar to what was seen when PAN-co-MAA was heated to 310 °C. The cellulose I and II peaks were still very prevalent in the WAXD pattern indicating the structure of cellulose was maintained at this temperature. Though it was observed in the pure CNC film at this temperature, these peaks no longer exist due to the breakdown of the cellulose structure. This further supports that CNC maintains its structure to a higher temperature in a PAN-co-MAA/CNC composite compared to a neat CNC film. As the film was further heated to 400 °C a peak developed at 2θ=25.3° similar to PAN at this temperature. There also exists a shoulder at a lower 2θ of 2θ=25.3° which appeared to have come from the addition of the peak at 2θ=16° seen in neat PAN-co-MAA and the very broad peak observed in neat CNC at 2θ=18.5° at 400 °C. Three small peaks were noted at 2θ=~23.5°, ~32.3°, and ~33.6° which were also seen in the neat CNC. The other small peaks found in the neat CNC at this temperature cannot be discerned, possibly due to low intensity. When the sample was rerun in air the peak at 2θ=25.3° had a slight

increase in magnitude; this was also seen in the neat PAN-co-MAA when under this condition. The sample that was run directly in air was similar to the sample that was first run in nitrogen followed by running in air.

B.3. DSC Testing Procedure Development

It has been shown in TGA that PAN-co-MAA undergoes thermal degradation in the range of 200-400 °C. During this thermal degradation, products are formed and in the DSC, it is possible that these products can contaminate the DSC cell. The amount of contamination is a factor of heating rate and sample size. It was found that due to the low exothermic reaction of the PAN-co-MAA films when it is rerun in air that this contamination, from the PAN-co-MAA film run nitrogen, would have a large effect on the DSC curve. Though it was observed that even in PAN-co-MAA fibers that the contamination would affect the curves of the samples rerun in air, but in a much less significant way than the PAN-co-MAA films. We found that a cleaning cycle of heating the cell to 500 °C in air and holding the temperature for 5 minutes would be able to clean out the cell, this procedure will be referred to as a cleaning cycle for the rest of the **Section B.3**.

We wanted to see how the contamination would affect the DSC curves, and the curves of this study can be found in **Figure B.4**. In **Figure B.4 (a)** are the DSC curves of the cleaning cycles of an empty DSC cell after running a PAN-co-MAA sample in nitrogen. The first cleaning cycles removes most of the contaminates, and the second cleaning cycle curve is relatively smooth. **Figure B.4. (b)** shows 2 DSC curves of PAN-co-MAA film ran in nitrogen after a different PAN-co-MAA film has been ran in nitrogen prior, but for 1

curve a cleaning cycle has been performed between the 2 film runs and the other curve no cleaning cycle was performed. The cyclization peak is a highly exothermic reaction and cleaning or no cleaning between runs did not result in any significant difference in the curves. In **Figure B.4 (c)** we looked at how the contamination would affect the DSC curves of the PAN-co-MAA films rerun in air. In the curve without cleaning beforehand 2 peaks can be seen, 1 peak for the oxidation of the PAN film and another for the reaction of the degradation products of the PAN-co-MAA that was created during the run in nitrogen. In the other curve where we cleaned the cell beforehand we do not see the 2nd exothermic peak related to the reaction of the PAN-co-MAA degradation products. In **Figure B.4 (d)** we can see the DSC curve of the PAN-co-MAA film ran in nitrogen, and the cleaning cycle curves after a PAN-co-MAA film has been reran in air. It can be noted that though there is some cleaning that is done during the cleaning run, the curve height is relatively insignificant to the overall peak of the sample. Though, for good practice we still used a cleaning cycle for the DSC between every sample run to prevent the effect of contamination. These effects are less apparent in PAN-co-MAA fibers, due to the larger exothermic peaks due to higher surface area, but it is still suggested to clean the DSC cell between runs for the most accurate measurements.

Table B.1. Enthalpy of reaction as measured by DSC for the dehydration and thermal scission of bridge oxygen that occurs in CNC.

Sample	Enthalpy of reaction (J/g)	Onset of reaction (°C)
CNC film cast from DMF	191	260
CNC film cast from DMF and ground	287	270
CNC film cast from water	104	250
CNC film cast from water and ground	243	264
As received freeze dried CNC	288	287

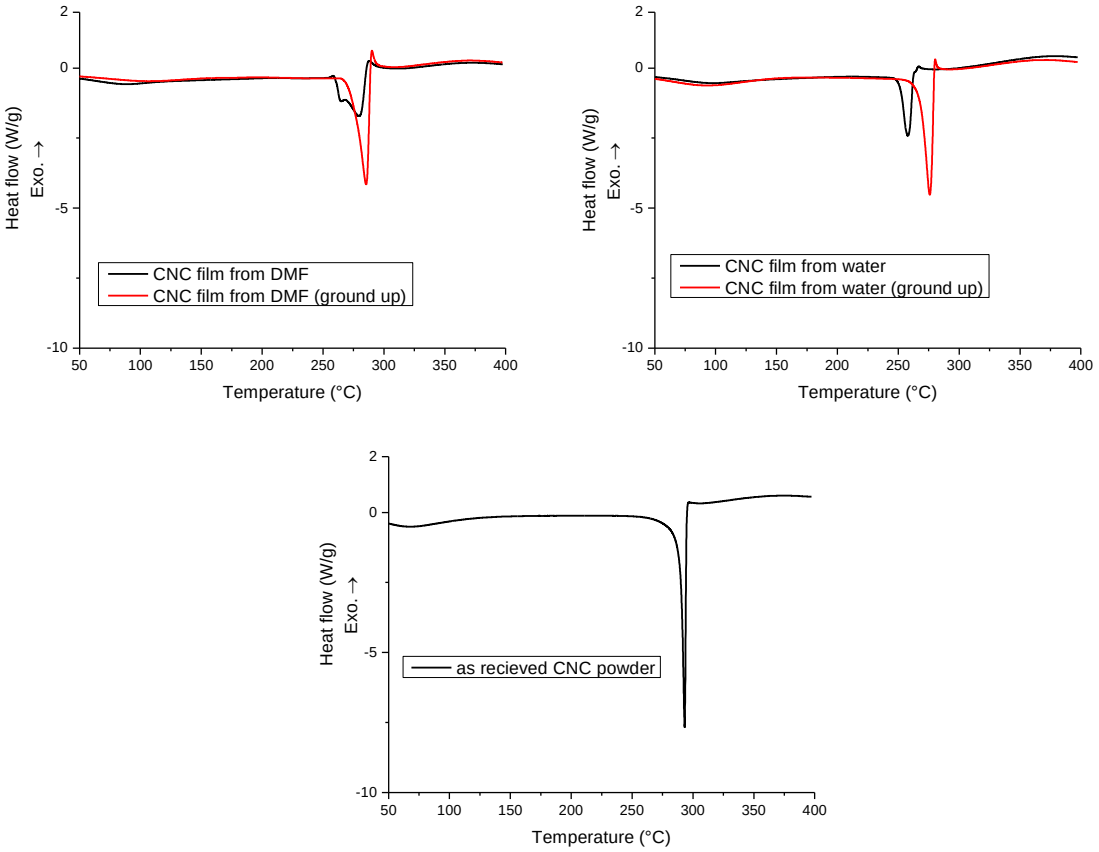

Figure B.1. DSC plots of CNC films prepared by different methods heated at 10 °C/min in nitrogen showing difference in curve shape and onset and peak temperatures. **(Top left)** CNC film cast from DMF, **(Top Right)** CNC film cast from water, and **(Bottom)** as received CNC powder.

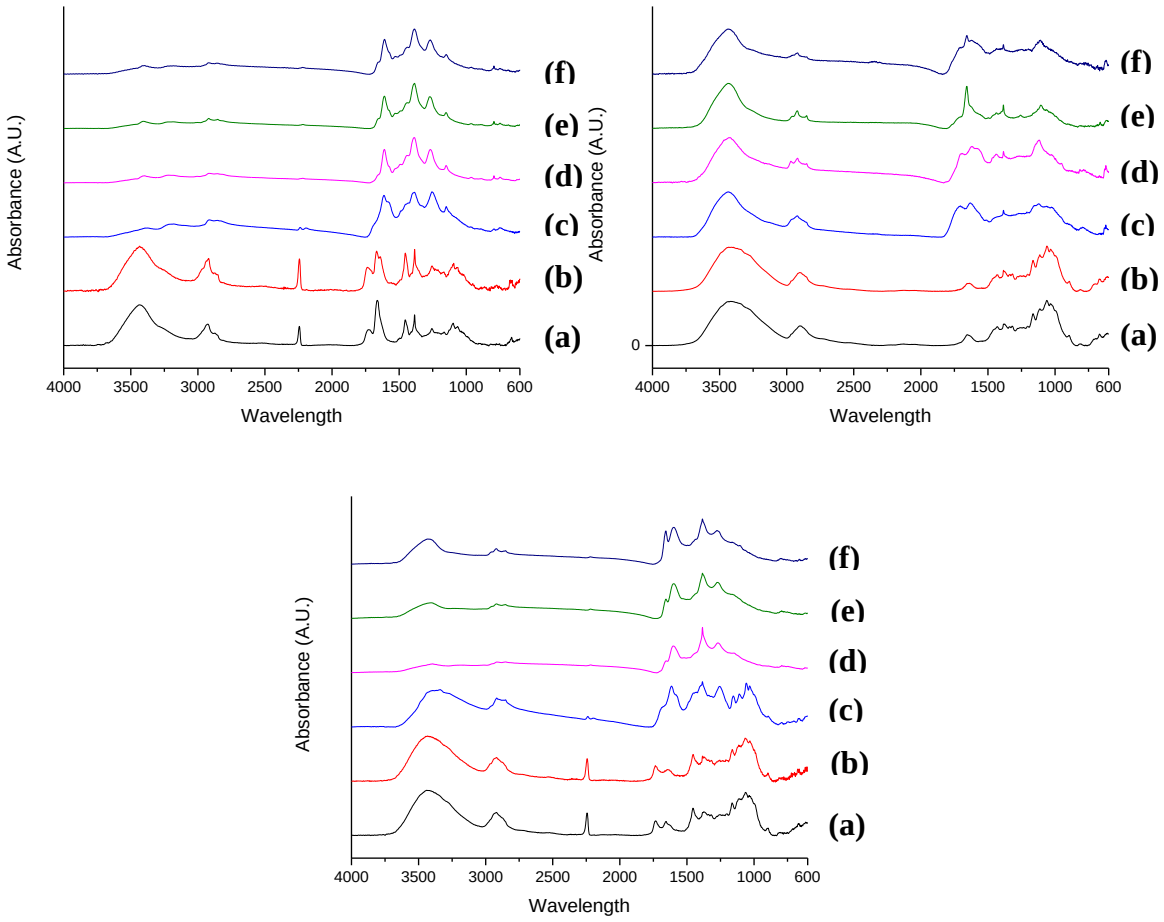

Figure B.2. FTIR of **(Top Left)** neat PAN-co-MAA, **(Top Right)** neat CNC, and **(Bottom)** CNC-40 heated at 10 °C/min to **(a)** unheated, **(b)** 160 °C in Nitrogen, **(c)** 310 °C in Nitrogen, **(d)** 400 °C in Nitrogen, **(e)** 400 °C in nitrogen followed by 400 °C in air, and **(f)** 400 °C in air.

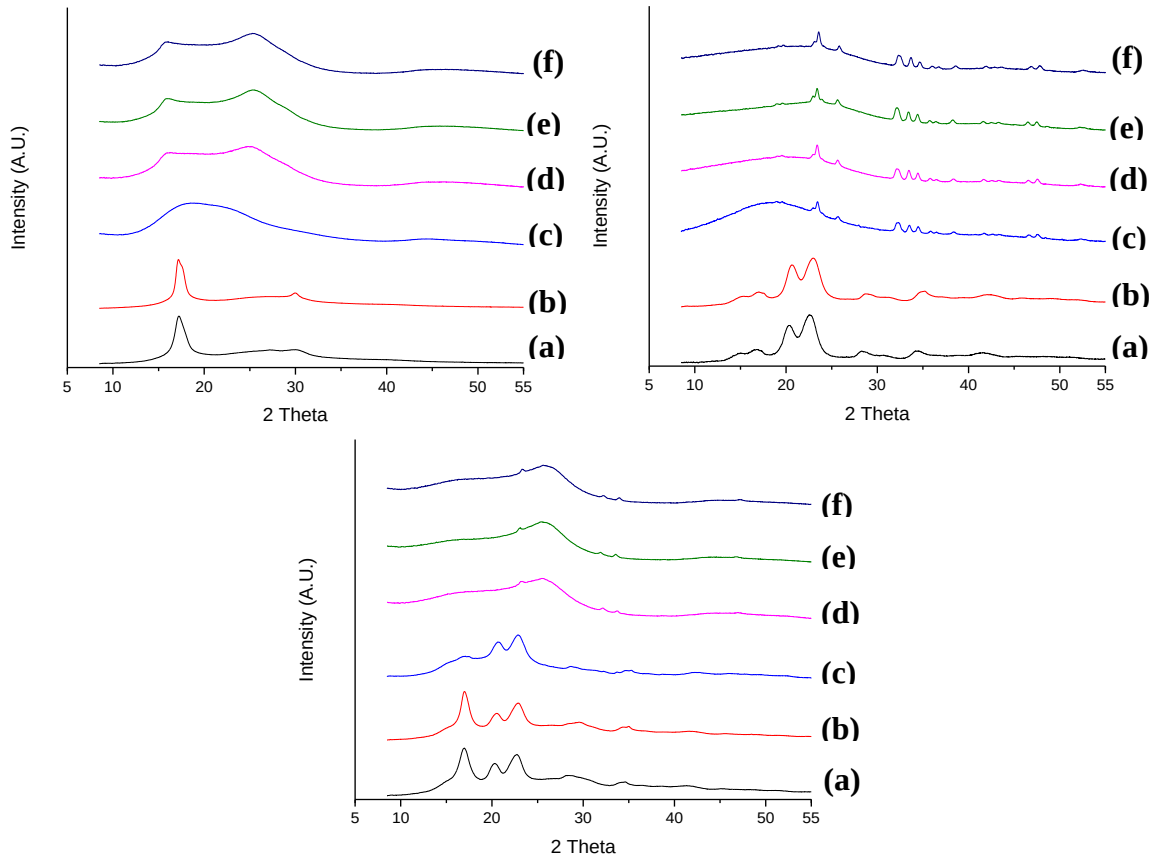

Figure B.3. WAXD 2-D integral plot of **(Top Left)** neat PAN-co-MAA, **(Top Right)** neat CNC, and **(Bottom)** CNC-40 heated at 10 °C/min to **(a)** unheated, **(b)** 160 °C in Nitrogen, **(c)** 310 °C in Nitrogen, **(d)** 400 °C in Nitrogen, **(e)** 400 °C in nitrogen followed by 400 °C in air, and **(f)** 400 °C in air.

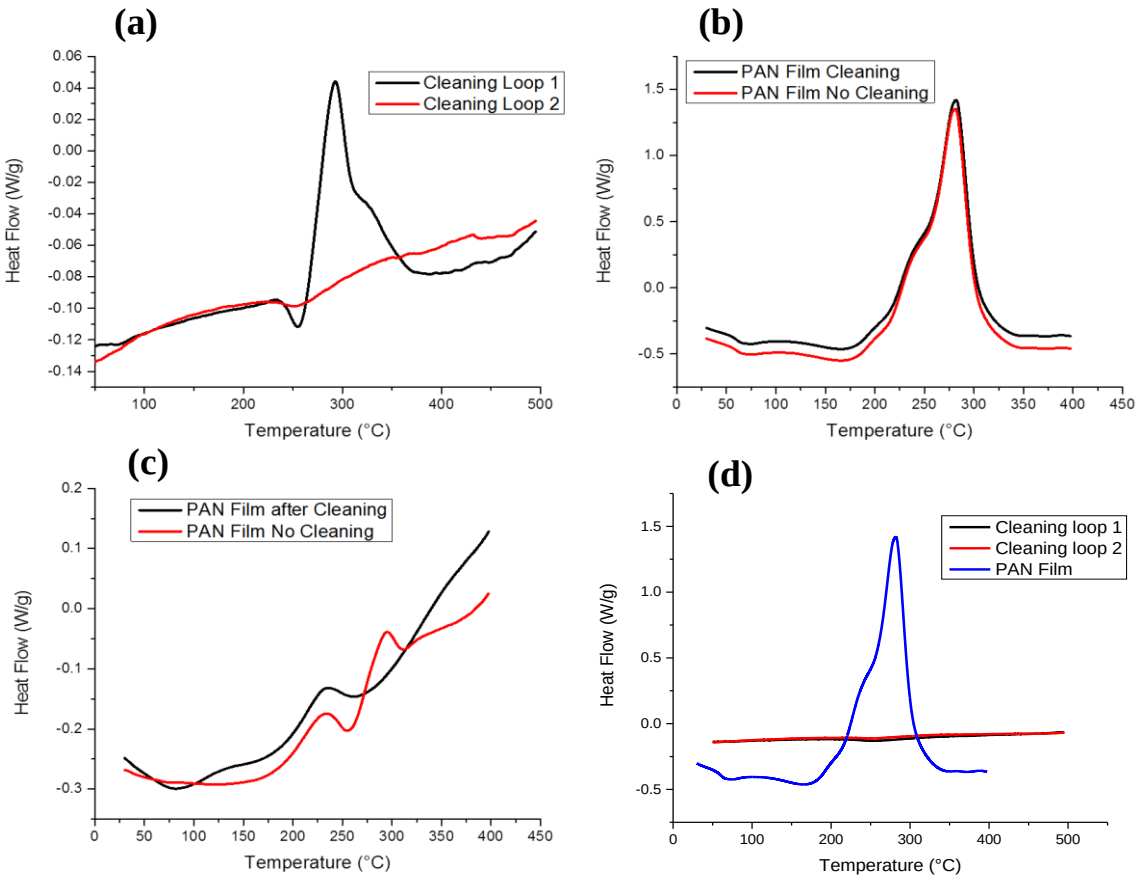

Figure B.4. **(a)** Curves from cleaning the DSC cell after running a PAN-co-MAA film in nitrogen showing 1 cleaning cycle is enough. **(b)** runs of the PAN-co-MAA film in nitrogen with and without cleaning after a PAN-co-MAA film run in nitrogen indicating no significant differences in the DSC curve. **(c)** Rerun of the PAN-co-MAA films in air with and without cleaning after a PAN-co-MAA film run in nitrogen, showing that cleaning must be done or the curve shape changes completely. **(d)** PAN-co-MAA film ran in nitrogen compared to the cleaning curves of the DSC cell after rerunning a PAN-co-MAA film in air indicating that there is not much contamination and it would not have a significant effect on the curve of a PAN-co-MAA film sample ran in nitrogen.

APPENDIX C. SUPPORTING INFORMATION FOR CHAPTER 4

C.1 Degree of Substitution Calculations (Sulfonation)

The degree of substitution of cellulose can be calculated based on the sulfur content measured from elemental analysis with **Equation C.1** where x is the degree of substitution. The concentration of sulfonated groups can also be calculated with **Equation C.2** where x is the degree of substitution found in **Equation C.1**. The 32.06 is the molar mass of sulfur, 162.14 is the molar mass of an anhydroglucose unit, and 80.06 is the molar mass of the sulfate group minus hydrogen.

$$\frac{x(32.06)}{162.14 + x(80.06)} X\ 100 = sulfur\ content\ (wt\%) \quad \textbf{(C.1)}$$

$$\frac{x}{162.14}\ X\ 1000 = \frac{mmol\ sulfate\ groups}{grams\ of\ cellulose} \quad \textbf{(C.2)}$$

C.2 Conductive Titration of TEMPO CNF

Conductive titration was performed by dispersing 168 mg of sodium form TEMPO CNF in 75 ml of DI water. This solution was continuously stirred with a magnetic stir bar. 1 M HCl was added to the suspension until the pH reached 2 (measured with a pH meter UltraBASIC (Denver Instruments) and stirred for 30 minutes before further experimentation to allow the sample to protonate. A 0.05 M NaOH solution was incrementally added to the suspension while conductivity was measured with a Thermo Scientific Orion Star with a conductivity probe attachment. NaOH was added until the pH of the sample reached 10. The conductivity titration curves can be found in **Figure C.6**. The degree of substitution was calculated with **Equation C.3** below with x, C, w, V_2, and

V_1 are degree of substitution, concentration of NaOH solution used (mol/L), weight of dried cellulose added (g), and V_2 and V_1 are the amounts of NaOH solution added at point indicated in **Figure C.6** [77]

$$x = \frac{162 * C * (V_2 - V_1)}{w - 36 * C * (V_2 - V_1)} \quad \textbf{(C.3)}$$

C.3 Earlier Sulfonation Trials and Reasons for Failures

Many failed trials occurred before we could determine how to make sulfonated CNF. The main cause of these failures is the water sensitivity of the reaction. Even for our highest CSA:AGU ratio sample (2.5:1) 1.1 ml of water will end the reaction, while the 0.5:1 and 1.5:1 CSA: AGU ratio samples only need 0.2 and 0.7 ml of water to end the reaction. This is because CSA reacts with water to form sulfuric acid (which would require much higher concentrations for sulfonation), while CSA is needed to convert into sulfur trioxide to do the reaction. The degradation pathway of CSA we desire is seen in **Equation C.4**, while the degradation pathway when there is water can be seen in **Equation C.5**. The calculation for the amount of water to convert all the CSA to HCl and sulfuric acid can be seen in **Equation C.6**. The c, R, and w in **Equation C.6** is the weight of CNF used in grams, R is the ratio of CSA to AGU, and w is amount of water needed to convert the CSA into HCl and sulfuric acid in ml. The 162 is the molecular weight of an AGU unit and 18 is the molecular weight of water.

$$ClSO_3H \rightarrow HCl + SO_3 \quad \textbf{(C.4)}$$

$$ClSO_3H + H_2O \rightarrow HCl + H_2SO_4 \quad \textbf{(C.5)}$$

$$\frac{c}{162} * R * 18 = w \quad \textbf{(C.6)}$$

Initially we started doing this reaction with CNF slurry acquired from the University of Maine (lot# 2012-FPL-CNC-48/051). We did this by diluting the CNF slurry into nonanhydrous DMF and distilling out the excess water. Though DMF and water do not form an azeotrope, it is very difficult to remove all the excess water due to how hydrophilic the cellulose and DMF is. So we started to use freeze dried CNF from the University of Maine that we dry in a vacuum oven at 70 °C for 1 day to try to reduce any bound water. Also we started to use anhydrous DMF to reduce the amount of water that might be introduced from the DMF. With the freeze dried CNF we were getting better results, but we could still not get sulfonated CNF at low CSA to AGU ratios even though we were drying the glassware with a heat gun before doing the reaction. To solve this problem, we started keeping the glassware in a 110 °C oven 1 day prior to the experiment, and using it almost directly out of the oven to reduce the effect of moisture. With this method we could get sulfonated sample even for our 0.5:1 CSA:AGU sample which only require 0.2 ml of water to convert all the CSA to sulfuric acid.

Figures and Tables

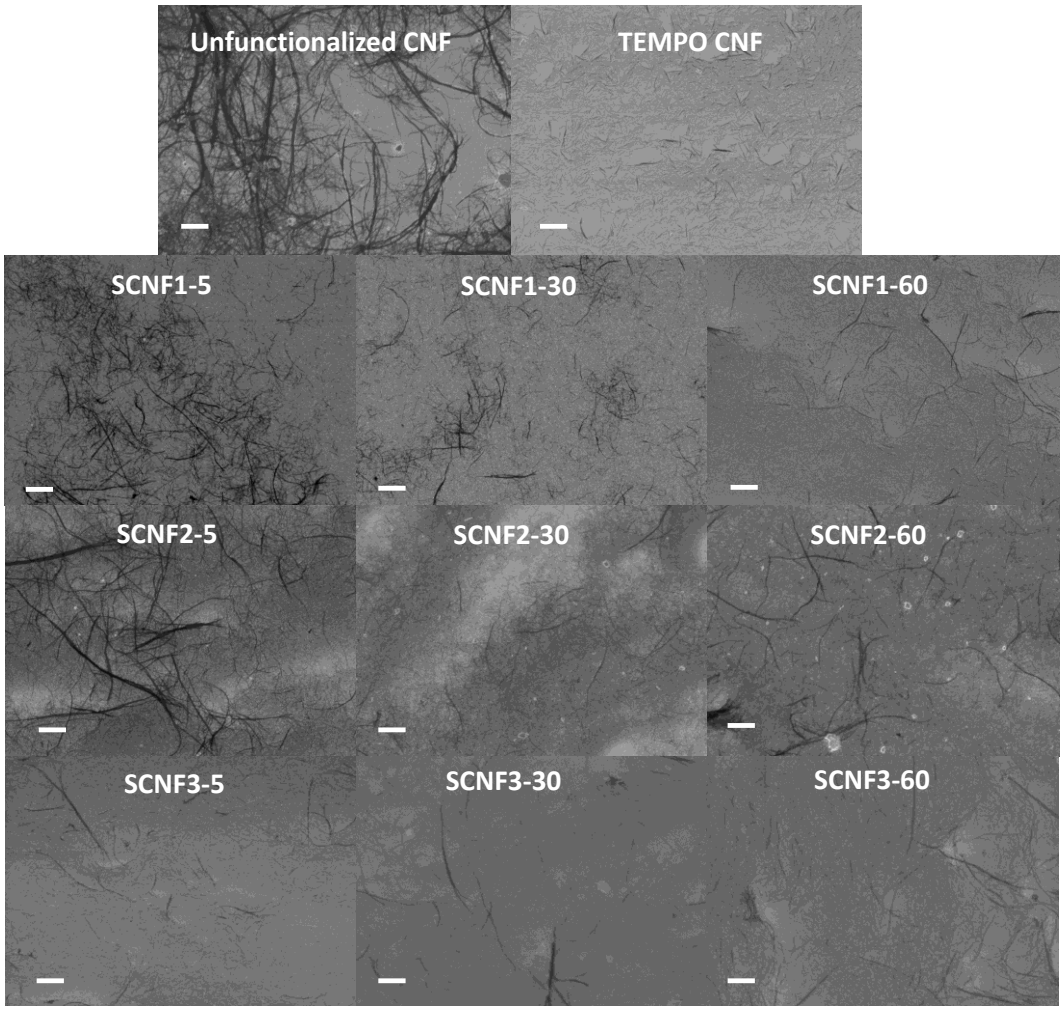

Figure C.1. SEM images of the all unfunctionalized and functionalized CNF samples, which shows that all sulfonated CNF samples retain fibril like morphology. Scale bar is 2 μm.

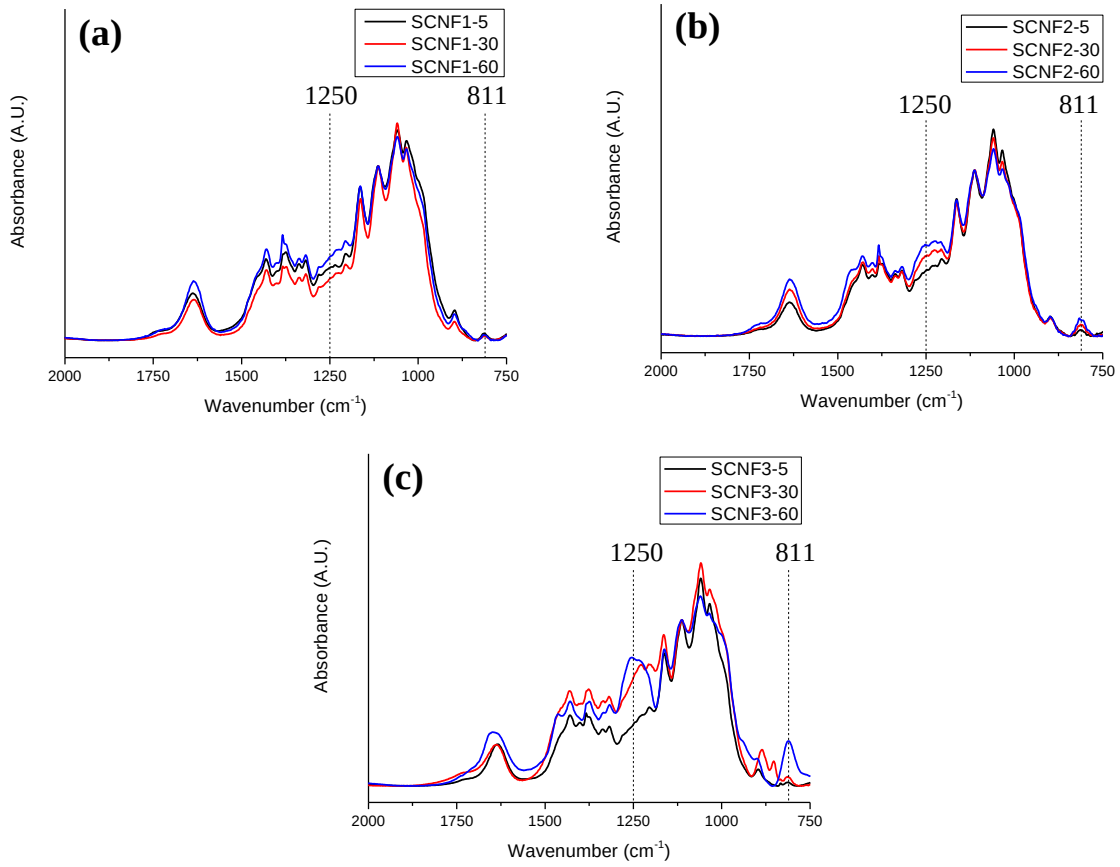

Figure C.2. FTIR spectra of **(a)** SCNF1, **(b)** SCNF2, and **(c)** SCNF3 films at different reaction times showing a trend of increasing 1250 and 811 cm^{-1} peaks with increasing sulfonation time. CNF films were cast from CNF dispersed in water.

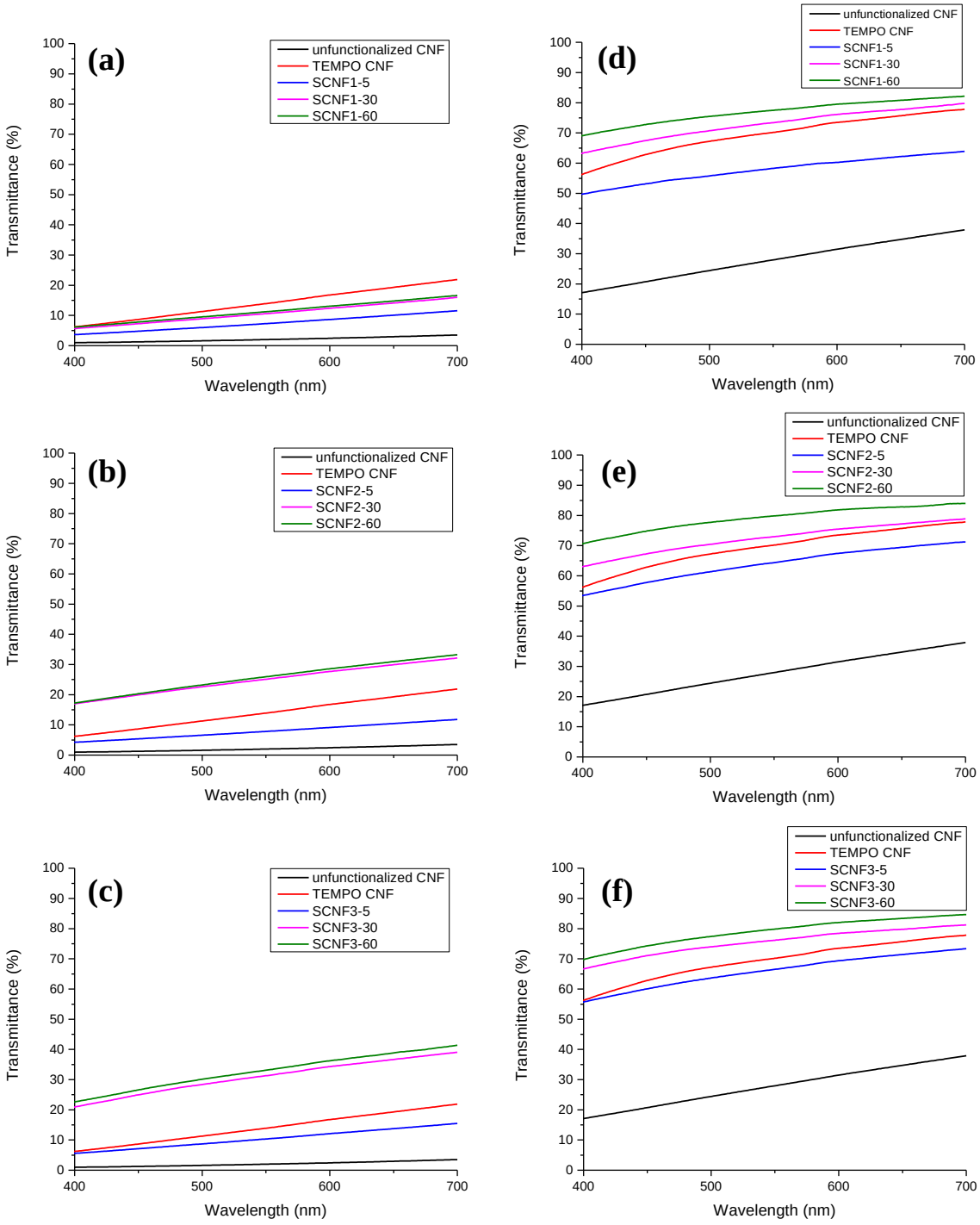

Figure C.3. Transmittance of suspensions (0.1 wt%) of sulfonated CNF compared to the unfunctionalized and TEMPO CNF dispersions as measured by UV-Vis. **(a)** SCNF1, **(b)** SCNF2, and **(c)** SCNF3 in DI water, and **(d)** SCNF1, **(e)** SCNF2, and **(f)** SCNF3 in DMF showing increasing reaction times leads to higher transmittance.

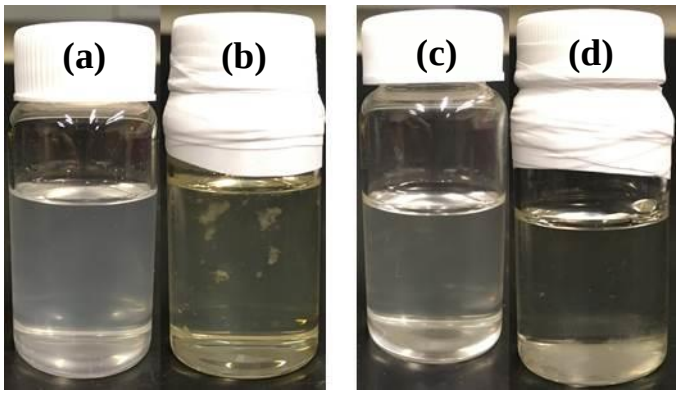

Figure C.4. (a) TEMPO CNF dispersed in DMF (0.1 wt%), and **(b)** TEMPO CNF dispersed in DMF (0.1 wt%) after undergoing heat treatment at 70 °C for 3 days showing a strong yellow hue developed. **(c)** SCNF3-60 dispersed in DMF (0.1 wt%), and **(d)** SCNF3-60 dispersed in DMF (0.1 wt%) after undergoing heat treatment at 70 °C for 3 days showing a slight yellow hue developed.

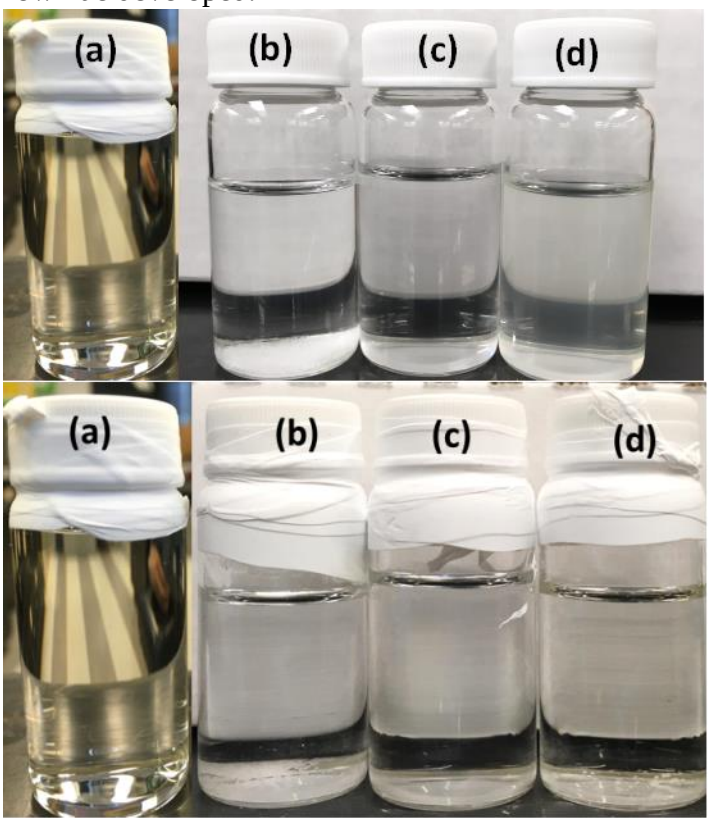

Figure C.5. (Top) chemicals used for TEMPO oxidation before heating in DMF **(a)** TEMPO radical (8.5 mg/ 100 ml), **(b)** NaCl (2g/100 ml), **(c)** acetic acid (7 ml/100ml), and **(d)** 14.5 wt% NaClO (7 ml/100 ml). **(Bottom)** Same chemicals as mentioned above, but after being heated at 70 °C for 3 days, images show no large change in color observed after heating.

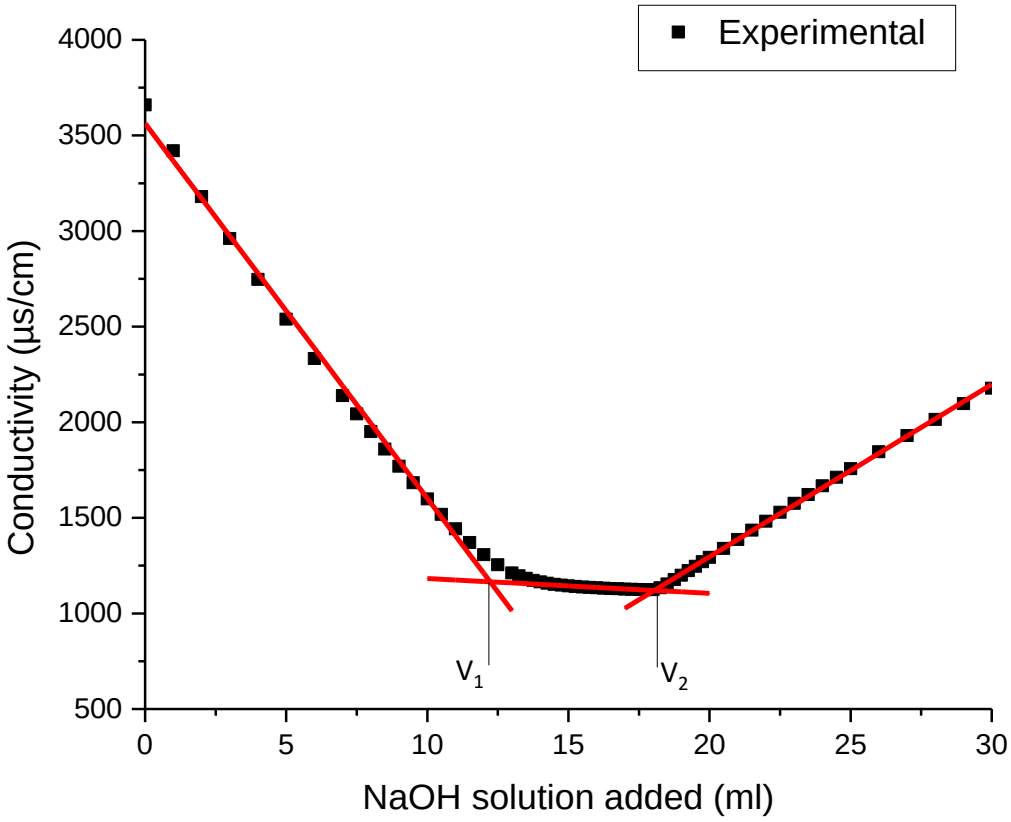

Figure C.6. Conductivity titration curve of the TEMPO CNF used to determine the degree of substitution.

APPENDIX D. SUPPORTING INFORMATION FOR CHAPTER 5

D.1 TEMPO Oxidation Procedure

The procedure for making TEMPO CNF and the effect of different processing procedures that can occur is not well documented. Due to this reason, there were initial troubles when TEMPO CNF was attempted to be made. It was found that if the TEMPO CNF was in the protonated form fibrillation of the CNF would not occur to the same degree as compared to TEMPO CNF in the sodium form. This can be seen in **Figure D.1 (a)** and **(b)**, showing that the TEMPO CNF in the sodium form after undergoing homogenization is relatively transparent, while the TEMPO CNF in the protonated form after undergoing the same homogenization procedure is still very opaque. To achieve relatively disperse TEMPO CNF in the protonated form, it was found that you could protonate fibrillated TEMPO CNF in the sodium form, and then undergo further homogenization of the protonated TEMPO CNF (**Figure D.1 (c)**).

D.2 Initial PAN-CNF Composite Fiber Spinning Trials

Initially unfunctionalized cellulose nanofibrils with PAN-co-MAA using DMF as the solvent were attempted to be spun, but the unfunctionalized CNF would not disperse well and clog the filters used in the spinning set up. To counteract this, we tried to spin without a filter, but do to the high inhomogeneity of the suspension it did not result in continuous fiber with the gel spinning process.

It was therefore decided, to increase the dispersibility of the CNF to spin these fibers so. To improve the dispersibility we tried using functionalized CNF with the most common functionalization, which is TEMPO oxidation. We made suspensions with

TEMPO CNF and PAN-co-MAA in DMF, but the solutions also became very heterogenous and would lead to clogging of the filter. After removing the filter continuous fiber could still not be made. As has been shown in **Chapter 5**, TEMPO CNF does not disperse well in DMF at high concentrations. This is hypothesized to occur due to all the ions that are generated with the degradation of DMF.

We determined that TEMPO CNF dispersed well in DMSO even at high concentrations this is due to the higher chemical stability of DMSO unlike DMF which would form ions due to degradation at elevated temperatures. Due to these findings suspensions of TEMPO CNF and PAN-co-MAA in DMSO were made, and with these suspensions, fibers could be spun without clogging the filter packs. Though the tensile properties of these fibers even at low CNF loading of 1 wt% were lower than the mechanical properties of the neat PAN-co-MAA fibers. This decrease in mechanical properties is likely due to low interaction between this functionalization and PAN-co-MAA. When the suspensions become concentrated, because the TEMPO CNF does not want to interact with the PAN-co-MAA it will aggregate with itself leading to stress concentrators in the final fiber. To counteract this problem a functionalization that interacted better with the PAN-co-MAA was needed. An amine group on the CNF should interact better with the PAN so amination of the CNF was done and the results of this CNF can be seen in **Chapter 5**.

D.3 PAN-CNF Sheath-Core Fiber

PAN-co-MAA as the sheath and TEMPO CNF as the core was attempted to be spun through the dry jet wet spinning process. The first attempt was using PAN-co-MAA

using DMF as the solvent and TEMPO CNF with water as the solvent mimicking the idea of how hollow fibers are spun. It was found that our spinning set up could not work with this method since the water in the TEMPO CNF interacted with the PAN-co-MAA solution in the distribution plates and would coagulate the PAN-co-MAA resulting in clogging of the system. We then tried the same set up but with TEMPO CNF in DMF, as mentioned before it was found that TEMPO CNF was found to aggregate in DMF and clog the filter pack, which is what occurred in this instance. Following this we tried using PAN-co-MAA with DMSO as the solvent and TCNF with DMSO as the solvent. Even with this the fibers could not be successfully continuously spun through we did obtain some fiber by dry-jet wet spinning into a coagulation bath and removing the fibers after it had coagulated. To spin these fibers a 500 μm diameter spinneret was used. The sheath was PAN-co-MAA at 15 wt% solid content, and the core was TEMPO CNF at ~1.3 wt% solid content. The reason we could not get consistent fiber is due to the high solvent content of the TEMPO CNF in the core, which reduce the stability of the sheath. Images of the fiber we spun can be found in **Figure D.2**. The fibers have a very non-circular cross section due to low solid content of the core and solidification during the drying process. We can also see that in some sections of the fibers that there is no CNF that can be seen indicating inhomogeneity along the fiber.

Figures and Tables

Table D.1. Draw ratios and tensile properties of neat PAN-co-MAA fibers spun with an ADR of 1.

ADR	CDR	HDR	TDR	Tensile strength (MPa)	Elastic modulus (GPa)	Strain at break (%)
1	1	1	1	108 ± 20	5.2 ± 1.0	2.8 ± 0.5
1	1	5	5	363 ± 37	10.6 ± 0.5	17.2 ± 1.2
1	1	7	7	433 ± 48	11.9 ± 1.0	13.5 ± 1.3
1	1	10	10	594 ± 70	14.1 ± 0.8	10.8 ± 0.7
1	1	15	15	867 ± 63	17.7 ± 0.5	8.7 ± 0.5
1	1	20	20	1060 ± 76	19.7 ± 0.5	8.7 ± 0.4
1	1.3	1	1	138 ± 5	6.2 ± 0.2	6.1 ± 1.3
1	1.3	3.8	5	429 ± 21	11.9 ± 0.3	15.1 ± 0.8
1	1.3	7.7	10	762 ± 45	17.5 ± 0.3	10.2 ± 0.7
1	1.3	11.5	15	911 ± 96	19.5 ± 1.0	8.8 ± 0.5

Table D.2. Draw ratios and tensile properties of neat PAN-co-MAA fibers spun with an ADR of 2.

ADR	CDR	HDR	TDR	Tensile strength (MPa)	Elastic modulus (GPa)	Strain at break (%)
2	1	1	2	130 ± 1	5.9 ± 0.1	24.1 ± 19.3
2	1	2.5	5	278 ± 15	9.7 ± 0.3	33.5 ± 7.1
2	1	5	10	509 ± 43	12.6 ± 0.7	13.9 ± 1.5
2	1	7.5	15	655 ± 71	15.6 ± 0.7	10.2 ± 1.1
2	1	10	20	777 ± 78	17.0 ± 0.8	9.1 ± 0.5
2	1.3	1	3	132 ± 2	6.1 ± 0.2	25.5 ± 14.4
2	1.3	1.9	5	242 ± 14	9.3 ± 0.3	39.2 ± 5.3
2	1.3	3.8	10	495 ± 30	13.0 ± 0.5	13.7 ± 1.3
2	1.3	5.8	15	656 ± 62	15.3 ± 0.5	10.9 ± 0.7
2	1.3	7.7	20	764 ± 114	17.7 ± 0.8	8.6 ± 0.7
2	1.3	9.6	25	887 ± 76	19.4 ± 0.6	8.3 ± 0.5

Table D.3. Draw ratios and tensile properties of neat PAN-co-MAA fibers spun with an ADR of 3.

ADR	CDR	HDR	TDR	Tensile strength (MPa)	Elastic modulus (GPa)	Strain at break (%)
3	1	1	3	126 ± 2	5.9 ± 0.4	16.7 ± 14.0
3	1	6.7	20	553 ± 34	14.3 ± 0.3	9.5 ± 0.5
3	1.3	1	4	135 ± 4	6.4 ± 0.1	77.3 ± 22.1
3	1.3	2.6	10	379 ± 18	11.2 ± 0.3	15.4 ± 1.3
3	1.3	3.8	15	497 ± 18	12.8 ± 0.3	11.1 ± 0.4
3	1.3	5.1	20	607 ± 30	14.6 ± 0.4	9.8 ± 0.5
3	1.3	6.5	25	651 ± 56	15.6 ± 0.8	9.7 ± 0.5
3	1.3	8	31	874 ± 58	18.4 ± 1.7	8.2 ± 0.5
3	1.3	9	35	888 ± 52	19.3 ± 0.4	8.3 ± 0.5

Table D.4. Draw ratios and tensile properties of TCNF-1 fibers spun with an ADR of 1.

ADR	CDR	HDR	TDR	Tensile strength (MPa)	Elastic modulus (GPa)	Strain at break (%)
1	1	1	1	37 ± 20	4.3 ± 0.7	1.2 ± 0.4
1	1	5	5	435 ± 23	12.9 ± 0.4	12.0 ± 0.6
1	1	10	10	714 ± 45	16.5 ± 0.4	9.3 ± 0.5
1	1	15	15	676 ± 49	17.9 ± 0.6	7.0 ± 0.4
1	1.3	1	1	118 ± 17	4.9 ± 1.1	3.3 ± 0.3
1	1.3	3.8	5	414 ± 48	12.5 ± 1.0	13.6 ± 1.6
1	1.3	7.7	10	702 ± 63	16.4 ± 0.8	10.2 ± 0.7
1	1.3	11.5	15	890 ± 65	19.2 ± 0.5	8.8 ± 0.5

Table D.5. Draw ratios and tensile properties of TCNF-1 fibers spun with an ADR of 2.

ADR	CDR	HDR	TDR	Tensile strength (MPa)	Elastic modulus (GPa)	Strain at break (%)
2	1	1	2	113 ± 7	5.3 ± 0.5	3.1 ± 0.4
2	1	2.5	5	196 ± 34	10.3 ± 0.6	5.7 ± 2.9
2	1	5	10	468 ± 37	14.5 ± 1.0	8.5 ± 0.4
2	1	7.5	15	731 ± 55	17.0 ± 0.7	9.8 ± 0.6
2	1	10	20	766 ± 45	16.5 ± 0.7	7.9 ± 0.3
2	1.3	1	3	108 ± 4	6.1 ± 0.1	4.9 ± 1.2
2	1.3	1.9	5	206 ± 16	8.9 ± 0.4	15.3 ± 1.9
2	1.3	3.8	10	456 ± 52	13.8 ± 0.9	9.9 ± 0.6
2	1.3	5.8	15	630 ± 51	15.8 ± 0.7	8.9 ± 0.7
2	1.3	7.7	20	754 ± 81	16.6 ± 0.9	7.9 ± 0.9

Table D.6. Draw ratios and tensile properties of TCNF-1 fibers spun with an ADR of 3.

ADR	CDR	HDR	TDR	Tensile strength (MPa)	Elastic modulus (GPa)	Strain at break (%)
3	1	1	3	123 ± 8	6.3 ± 0.4	3.1 ± 0.4
3	1	2.6	8	253 ± 29	10.2 ± 0.7	10.5 ± 1.0
3	1	3.3	10	374 ± 22	13.1 ± 0.6	9.5 ± 0.5
3	1	5	15	537 ± 33	15.4 ± 0.5	8.2 ± 0.5
3	1	6.7	20	617 ± 58	17.0 ± 0.8	7.3 ± 0.6
3	1	8.3	25	717 ± 46	17.1 ± 0.8	7.3 ± 0.4
3	1.3	1	4	131 ± 11	6.7 ± 0.5	7.4 ± 1.5
3	1.3	2.6	10	348 ± 47	11.7 ± 1.0	10.3 ± 0.9
3	1.3	3.8	15	570 ± 71	15.5 ± 0.9	9.5 ± 0.7
3	1.3	5.1	20	696 ± 80	17.2 ± 1.1	8.2 ± 0.5

Table D.7. Draw ratios and tensile properties of TCNF-5 fibers spun with an ADR of 1.

ADR	CDR	HDR	TDR	Tensile strength (MPa)	Elastic modulus (GPa)	Strain at break (%)
1	1	1	1	31 ± 4	3.2 ± 0.8	1.8 ± 0.6
1	1	3	3	146 ± 13	8.2 ± 1.0	5.2 ± 0.9
1	1	5	5	235 ± 21	7.7 ± 0.6	9.8 ± 0.5
1	1	7	7	422 ± 42	13.1 ± 0.7	8.4 ± 0.6
1	1	9	9	432 ± 27	14.8 ± 0.6	6.0 ± 0.4
1	1	10	10	492 ± 45	14.2 ± 0.9	7.6 ± 0.7
1	1	12	12	504 ± 25	17.1 ± 0.6	5.7 ± 0.3
1	1	13	13	486 ± 45	17.2 ± 1.1	5.5 ± 0.6

Table D.8. Draw ratios and tensile properties of TCNF-5 fibers spun with an ADR of 2.

ADR	CDR	HDR	TDR	Tensile strength (MPa)	Elastic modulus (GPa)	Strain at break (%)
2	1	1	2	61 ± 20	5.8 ± 0.4	1.5 ± 0.4
2	1	2.5	5	180 ± 43	10.3 ± 1.0	4.3 ± 1.6
2	1	5	10	313 ± 30	13.0 ± 0.8	6.0 ± 0.9
2	1	6	12	328 ± 30	14.1 ± 0.6	5.9 ± 0.9

Table D.9. Draw ratios and tensile properties of TCNF-10 fibers spun with an ADR of 1.

ADR	CDR	HDR	TDR	Tensile strength (MPa)	Elastic modulus (GPa)	Strain at break (%)
1	1	1	1	15 ± 6	3.6 ± 1.1	0.7 ± 0.2
1	1	5	5	287 ± 28	13.8 ± 0.7	6.2 ± 0.6
1	1	7	7	357 ± 18	14.7 ± 0.4	7.3 ± 0.5

Table D.10. Draw ratios and tensile properties of ACNF-1 fibers spun with an ADR of 1.

ADR	CDR	HDR	TDR	Tensile strength (MPa)	Elastic modulus (GPa)	Strain at break (%)
1	1	1	1	98 ± 20	5.7 ± 0.4	2.6 ± 0.7
1	1	5	5	477 ± 23	13.3 ± 0.2	11.3 ± 0.8
1	1	10	10	886 ± 50	17.4 ± 0.3	9.8 ± 0.6
1	1	13	13	1150 ± 91	18.9 ± 0.4	9.8 ± 0.8
1	1	15	15	1160 ± 91	19.3 ± 0.9	9.3 ± 0.6
1	1.3	1	1.3	80 ± 13	4.4 ± 0.7	11.0 ± 7.6
1	1.3	3.8	4.94	383 ± 115	11.7 ± 1.6	10.3 ± 1.5
1	1.3	7.7	10	845 ± 50	17.0 ± 0.6	9.6 ± 0.7

Table D.11. Draw ratios and tensile properties of ACNF-1 fibers spun with an ADR of 2.

ADR	CDR	HDR	TDR	Tensile strength (MPa)	Elastic modulus (GPa)	Strain at break (%)
2	1	1	2	91 ± 21	5.2 ± 0.8	9.6 ± 6.3
2	1	2.5	5	286 ± 11	10.6 ± 0.2	15.8 ± 1.9
2	1	5	10	595 ± 48	15.0 ± 0.4	10.7 ± 0.9
2	1	7.5	15	793 ± 47	17.2 ± 0.3	9.1 ± 0.6
2	1	10	20	889 ± 56	17.9 ± 0.3	8.6 ± 0.6
2	1	10.5	21	947 ± 34	18.0 ± 0.3	8.7 ± 0.3
2	1	11	22	967 ± 57	17.9 ± 0.4	8.7 ± 0.3
2	1.3	1	3	89 ± 4	4.3 ± 0.2	41.7 ± 8.8
2	1.3	1.9	5	273 ± 34	9.8 ± 0.4	17.0 ± 2.3
2	1.3	3.9	10	541 ± 39	13.6 ± 0.7	11.1 ± 0.9
2	1.3	5.8	15	669 ± 43	17.1 ± 0.3	7.8 ± 0.5
2	1.3	6.9	18	655 ± 52	16.1 ± 0.7	8.3 ± 0.8

Table D.12. Draw ratios and tensile properties of ACNF-1 fibers spun with an ADR of 3.

ADR	CDR	HDR	TDR	Tensile strength (MPa)	Elastic modulus (GPa)	Strain at break (%)
3	1	1	3	103 ± 4	5.6 ± 0.2	9.5 ± 4.0
3	1	1.7	5	189 ± 41	8.2 ± 1.3	20.4 ± 4.5
3	1	3.3	10	398 ± 31	11.6 ± 0.5	12.9 ± 0.7
3	1	5	15	463 ± 36	12.1 ± 0.6	10.4 ± 0.7
3	1	6.7	20	594 ± 51	15.5 ± 0.7	7.9 ± 0.4
3	1.3	1	4	119 ± 4	5.9 ± 0.1	43.4 ± 13.4
3	1.3	1.3	5	202 ± 21	8.3 ± 0.5	21.4 ± 3.9
3	1.3	2.6	10	389 ± 32	11.6 ± 0.5	12.4 ± 0.8
3	1.3	3.8	15	531 ± 50	14.9 ± 0.5	9.1 ± 0.9
3	1.3	5.2	20	755 ± 57	16.7 ± 0.6	9.7 ± 0.8
3	1.3	6.7	26	754 ± 75	17.0 ± 1.0	8.7 ± 0.5
3	1.3	7.2	28	726 ± 51	17.6 ± 1.2	7.8 ± 0.9

Table D.13. Draw ratios and tensile properties of ACNF-5 fibers spun with an ADR of 1.

ADR	CDR	HDR	TDR	Tensile strength (MPa)	Elastic modulus (GPa)	Strain at break (%)
1	1	1.0	1	89 ± 13	5.6 ± 0.1	2.7 ± 0.6
1	1	5.0	5	317 ± 100	10.8 ± 1.8	9.2 ± 2.5
1	1	10.0	10	722 ± 50	15.9 ± 0.5	8.7 ± 0.6
1	1	11.0	11	738 ± 50	16.2 ± 0.5	8.4 ± 0.6
1	1	12.0	12	890 ± 52	17.8 ± 0.3	9.5 ± 0.5
1	1.3	1.0	1	87 ± 8	5.3 ± 0.4	6.8 ± 2.5
1	1.3	3.9	5	453 ± 60	12.6 ± 1.0	15.6 ± 2.5
1	1.3	7.8	10	723 ± 92	16.4 ± 1.4	10.4 ± 1.4
1	1.3	8.5	11	765 ± 94	17.0 ± 0.8	9.6 ± 0.7

Table D.14. Draw ratios and tensile properties of ACNF-5 fibers spun with an ADR of 2.

ADR	CDR	HDR	TDR	Tensile strength (MPa)	Elastic modulus (GPa)	Strain at break (%)
2	1	1.0	2	94 ± 6	5.7 ± 0.2	6.1 ± 2.4
2	1	2.5	5	264 ± 24	11.0 ± 0.6	15.4 ± 2.6
2	1	5.0	10	548 ± 38	14.8 ± 0.4	10.5 ± 1.0
2	1	6.0	12	590 ± 44	15.6 ± 0.5	8.9 ± 0.7
2	1	6.5	13	580 ± 43	15.6 ± 0.5	8.4 ± 0.6
2	1.3	1.0	3	87 ± 13	5.2 ± 0.5	8.4 ± 9.1
2	1.3	1.9	5	194 ± 10	8.7 ± 0.3	15.9 ± 1.4
2	1.3	3.9	10	399 ± 16	12.3 ± 0.3	9.5 ± 0.5
2	1.3	5.8	15	614 ± 50	14.7 ± 0.2	9.2 ± 0.9

Table D.15. Draw ratios and tensile parameters of ACNF-5 fibers spun with an ADR of 3.

ADR	CDR	HDR	TDR	Tensile strength (MPa)	Elastic modulus (GPa)	Strain at break (%)
3	1	1.0	3	109 ± 6	6.1 ± 0.2	10.1 ± 4.8
3	1	1.7	5	192 ± 10	9.3 ± 0.3	15.0 ± 1.1
3	1	3.3	10	426 ± 19	13.2 ± 0.4	11.7 ± 0.7
3	1	5.0	15	488 ± 27	15.0 ± 0.4	7.7 ± 0.8
3	1.3	1.0	4	108 ± 9	6.1 ± 0.4	14.9 ± 5.4
3	1.3	1.3	5	183 ± 9	8.8 ± 0.3	19.6 ± 1.4
3	1.3	2.6	10	392 ± 37	12.8 ± 0.6	14.1 ± 1.3
3	1.3	3.9	15	565 ± 45	14.8 ± 0.5	11.0 ± 0.9
3	1.3	4.4	17	519 ± 37	14.8 ± 0.5	7.6 ± 0.8
3	1.3	4.9	19	541 ± 36	14.9 ± 0.4	7.2 ± 0.3

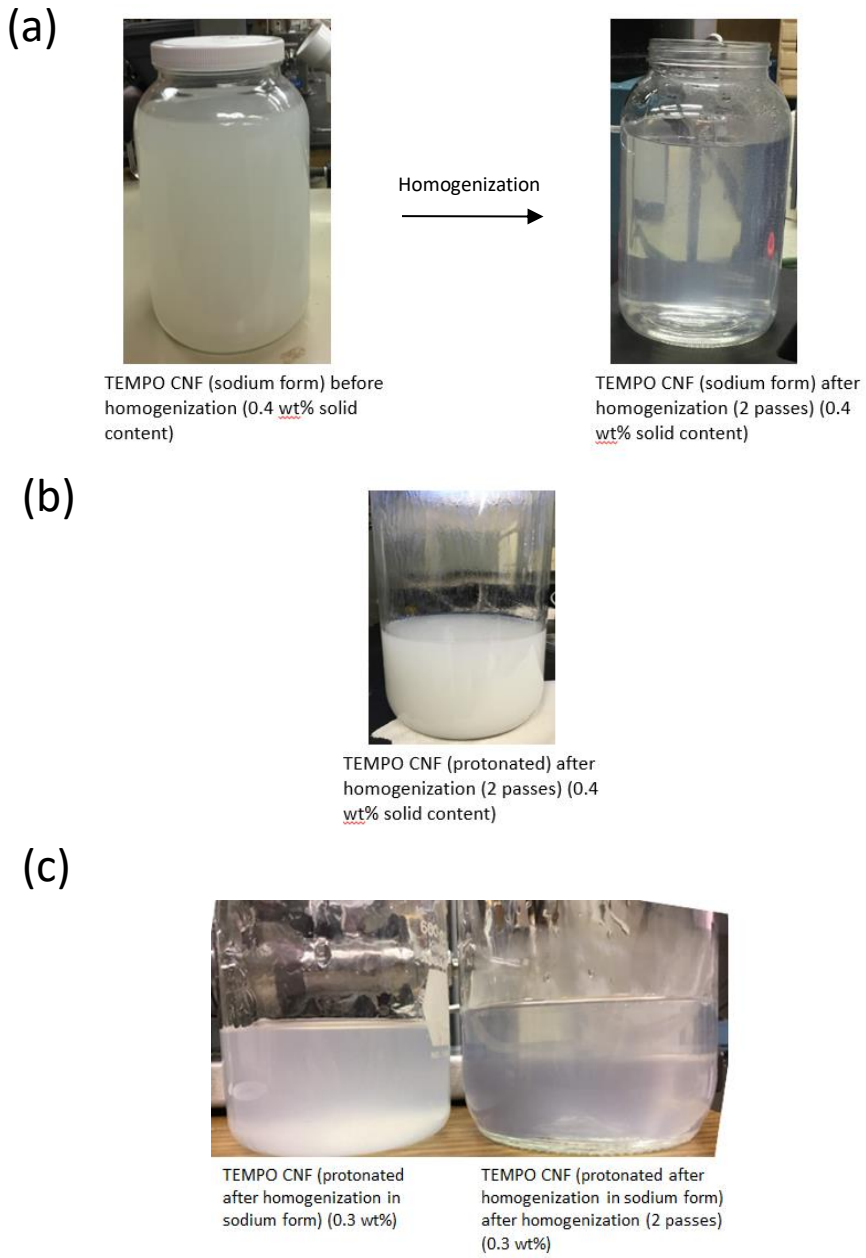

Figure D.1. **(a)** Showing the increase in transparency of the TEMPO CNF in sodium form after 2 passes at 25000 psi in a homogenizer. **(b)** showing that even after two passes the protonated TEMPO CNF is still very opaque indicating the dispersion is not very good and the TEMPO CNF is likely not well fibrillated (more passes were done and sample never reached much better transparency). **(c)** Method to achieve relatively well dispersed protonated TEMPO CNF by protonating fibrillated sodium form TEMPO CNF followed by additional homogenization.

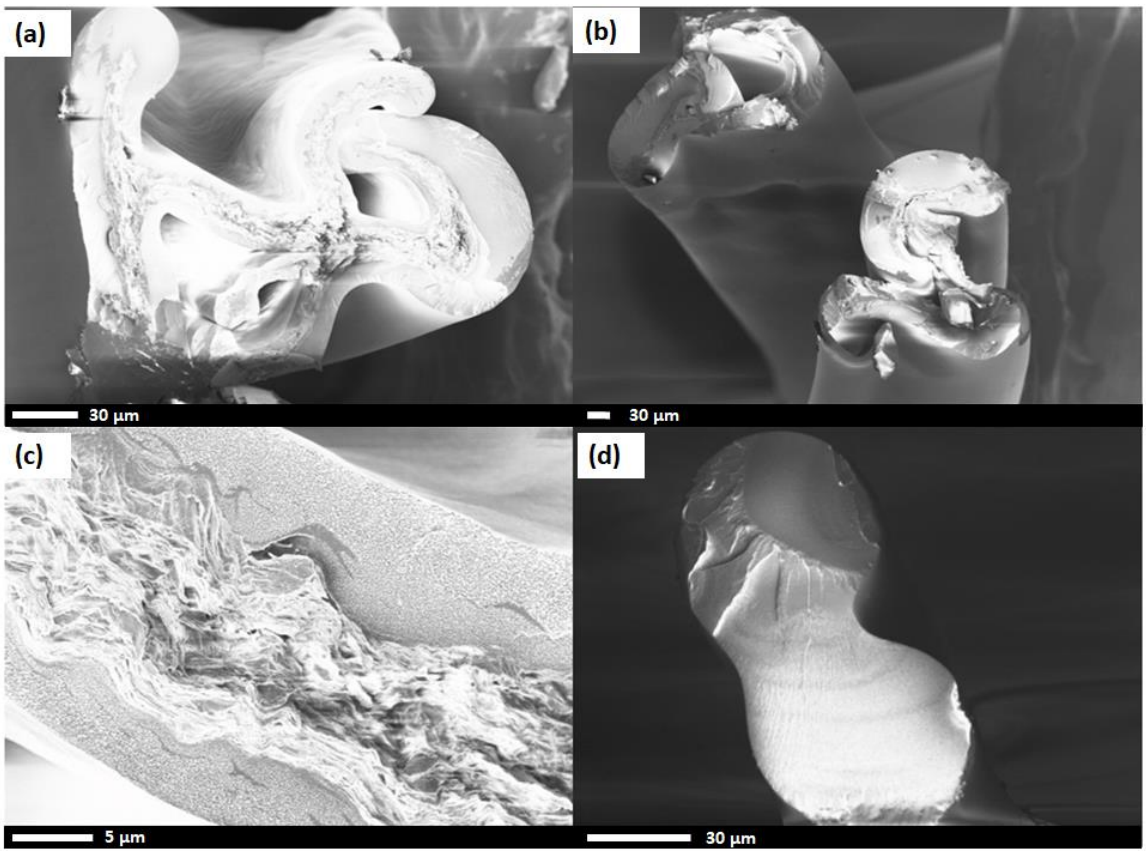

Figure D.2. **(a, b)** Showing cross section of PAN-TEMPO CNF sheath-core fiber showing that the cross section is highly irregular. **(c)** More zoomed in image of the CNF core showing the difference in texture between the CNF and PAN-co-MAA. **(d)** Cross section of the PAN-TEMPO CNF sheath-core fiber that does not show any CNF in the core.

REFERENCES

1. Capone, G.J. and J.C. Masson, *Encyclopedia Of Polymer Science and Technology*. 2002: John Wiley & Sons, Inc.

2. Seymour, R.B. and R.S. Porter, *Manmade fibers: their origin and development*. 1993: Springer Netherlands. 466.

3. Robson, R., M. Lewin, and E. Pearce, *Handbook of fiber chemistry*. 1998, New York: Marcel Dekker Inc.

4. Rahaman, M.S.A., A.F. Ismail, and A. Mustafa, *A review of heat treatment on polyacrylonitrile fiber.* Polymer Degradation and Stability, 2007. **92**(8): p. 1421-1432.

5. Herbert, R., *Manufacture of shaped articles of polymeric acrylic acid nitrile*, US, Editor. 1938, IG Farbenindustrie AG US.

6. Park, S.-J., *Carbon fibers*. 2015: Springer.

7. Masson, J., *Acrylic fiber technology and applications*. 1995, New York: CRC Press. 408.

8. Scharnagl, N. and H. Buschatz, *Polyacrylonitrile (PAN) membranes for ultra-and microfiltration.* Desalination, 2001. **139**(1-3): p. 191-198.

9. Klemm, D., et al., *Cellulose: fascinating biopolymer and sustainable raw material.* Angewandte Chemie International Edition, 2005. **44**(22): p. 3358-3393.

10. Eveleigh, D., *Cellulase: a perspective.* Philosophical Transactions of the Royal Society of London A: Mathematical, Physical and Engineering Sciences, 1987. **321**(1561): p. 435-447.

11. Moon, R.J., et al., *Cellulose nanomaterials review: structure, properties and nanocomposites.* Chemical Society Reviews, 2011. **40**(7): p. 3941-3994.

12. Azizi Samir, M.A.S., F. Alloin, and A. Dufresne, *Review of recent research into cellulosic whiskers, their properties and their application in nanocomposite field.* Biomacromolecules, 2005. **6**(2): p. 612-626.

13. Lee, K.-Y., et al., *On the use of nanocellulose as reinforcement in polymer matrix composites.* Composites Science and Technology, 2014. **105**: p. 15-27.

14. Pecoraro, E., et al., *Bacterial cellulose from Glucanacetobacter xylinus: preparation, properties and applications*. Monomers, polymers and composites from renewable resources, ed. M.B.A. Gandini. 2008: Elsevier Science. 369.

15. Shinoda, R., et al., *Relationship between length and degree of polymerization of TEMPO-oxidized cellulose nanofibrils.* Biomacromolecules, 2012. **13**(3): p. 842-849.

16. Qing, Y., et al., *A comparative study of cellulose nanofibrils disintegrated via multiple processing approaches.* Carbohydrate polymers, 2013. **97**(1): p. 226-234.

17. Cheng, Q., S. Wang, and D.P. Harper, *Effects of process and source on elastic modulus of single cellulose fibrils evaluated by atomic force microscopy.* Composites Part A: Applied Science and Manufacturing, 2009. **40**(5): p. 583-588.

18. Cheng, Q. and S. Wang, *A method for testing the elastic modulus of single cellulose fibrils via atomic force microscopy.* Composites Part A: Applied Science and Manufacturing, 2008. **39**(12): p. 1838-1843.

19. Saito, T., et al., *An ultrastrong nanofibrillar biomaterial: the strength of single cellulose nanofibrils revealed via sonication-induced fragmentation.* Biomacromolecules, 2012. **14**(1): p. 248-253.

20. Chang, H., et al., *Individually Dispersed Wood-Based Cellulose Nanocrystals.* ACS applied materials & interfaces, 2016. **8**(9): p. 5768-5771.

21. Beck, S., J. Bouchard, and R. Berry, *Dispersibility in water of dried nanocrystalline cellulose.* Biomacromolecules, 2012. **13**(5): p. 1486-1494.

22. Mittal, V., *Nanocomposites with Biodegradable Polymers: Synthesis, Properties, and Future Perspectives*. 2011, Oxford: Oxford University Press.

23. Saito, T., et al., *Cellulose nanofibers prepared by TEMPO-mediated oxidation of native cellulose.* Biomacromolecules, 2007. **8**(8): p. 2485-2491.

24. Henriksson, M., et al., *Cellulose nanopaper structures of high toughness.* Biomacromolecules, 2008. **9**(6): p. 1579-1585.

25. Chun, S.-J., et al., *Preparation of ultrastrength nanopapers using cellulose nanofibrils.* Journal of Industrial and Engineering Chemistry, 2011. **17**(3): p. 521-526.

26. Sehaqui, H., et al., *Cellulose nanofiber orientation in nanopaper and nanocomposites by cold drawing.* ACS applied materials & interfaces, 2012. **4**(2): p. 1043-1049.

27. Iwamoto, S., A. Isogai, and T. Iwata, *Structure and mechanical properties of wet-spun fibers made from natural cellulose nanofibers.* Biomacromolecules, 2011. **12**(3): p. 831-836.

28. Walther, A., et al., *Multifunctional high-performance biofibers based on wet-extrusion of renewable native cellulose nanofibrils.* Advanced Materials, 2011. **23**(26): p. 2924-2928.

29. Torres-Rendon, J.G., et al., *Mechanical performance of macrofibers of cellulose and chitin nanofibrils aligned by wet-stretching: a critical comparison.* Biomacromolecules, 2014. **15**(7): p. 2709-2717.

30. Håkansson, K.M., et al., *Hydrodynamic alignment and assembly of nanofibrils resulting in strong cellulose filaments.* Nature communications, 2014. **5**.

31. Mittal, N., et al., *Ultrastrong and Bioactive Nanostructured Bio-Based Composites.* ACS nano, 2017. **11**(5): p. 5148-5159.

32. Hooshmand, S., et al., *Dry-Spun Single-Filament Fibers Comprising Solely Cellulose Nanofibers from Bioresidue.* ACS applied materials & interfaces, 2015. **7**(23): p. 13022-13028.

33. Reising, A.B., R.J. Moon, and J.P. Youngblood, *Effect of particle alignment on mechanical properties of neat cellulose nanocrystal films.* Journal of Science & Technology for Forest Products and Processes, 2012. **2**(6): p. 32-41.

34. Siqueira, G., J. Bras, and A. Dufresne, *Cellulosic bionanocomposites: a review of preparation, properties and applications.* Polymers, 2010. **2**(4): p. 728-765.

35. Derakhshandeh, B., et al., *Ageing, yielding, and rheology of nanocrystalline cellulose suspensions.* Journal of Rheology, 2013. **57**(1): p. 131-148.

36. Majoinen, J., et al., *SEM imaging of chiral nematic films cast from cellulose nanocrystal suspensions.* Cellulose, 2012. **19**(5): p. 1599-1605.

37. Ureña-Benavides, E.E., et al., *Rheology and phase behavior of lyotropic cellulose nanocrystal suspensions.* Macromolecules, 2011. **44**(22): p. 8990-8998.

38. Sreekumar, T.V., et al., *Polyacrylonitrile single-walled carbon nanotube composite fibers.* Advanced Materials, 2004. **16**(1): p. 58-61.

39. Guo, H., et al., *Structure and properties of polyacrylonitrile/single wall carbon nanotube composite films.* Polymer, 2005. **46**(9): p. 3001-3005.

40. Chien, A.-T., et al., *Electrical conductivity and Joule heating of polyacrylonitrile/carbon nanotube composite fibers.* Polymer, 2014. **55**(26): p. 6896-6905.

41. Chang, H., et al., *Gel spinning of polyacrylonitrile/cellulose nanocrystal composite fibers.* ACS Biomaterials Science & Engineering, 2015. **1**(7): p. 610-616.

42. Liang, B., et al., *High performance graphene oxide/polyacrylonitrile composite pervaporation membranes for desalination applications.* Journal of Materials Chemistry A, 2015. **3**(9): p. 5140-5147.

43. Chien, A.-T., et al., *High-strength superparamagnetic composite fibers.* Polymer, 2014. **55**(16): p. 4116-4124.

44. Lin, Y., et al., *Polyacrylonitrile/ferrous chloride composite porous nanofibers and their strong Cr-removal performance.* Journal of Materials Chemistry, 2011. **21**(4): p. 991-997.

45. Madakbaş, S., E. Çakmakçı, and M.V. Kahraman, *Preparation and thermal properties of polyacrylonitrile/hexagonal boron nitride composites.* Thermochimica acta, 2013. **552**: p. 1-4.

46. Kiziltas, E.E., et al., *Preparation and characterization of transparent PMMA–cellulose-based nanocomposites.* Carbohyd Polym, 2015. **127**: p. 381-389.

47. Roohani, M., et al., *Cellulose whiskers reinforced polyvinyl alcohol copolymers nanocomposites.* Eur. Polym. J., 2008. **44**(8): p. 2489-2498.

48. Fortunati, E., et al., *Cellulose nanocrystals extracted from okra fibers in PVA nanocomposites.* J. Appl. Polym. Sci., 2013. **128**(5): p. 3220-3230.

49. Rescignano, N., et al., *PVA bio-nanocomposites: A new take-off using cellulose nanocrystals and PLGA nanoparticles.* Carbohyd Polym, 2014. **99**: p. 47-58.

50. Xu, X., et al., *Properties of novel polyvinyl alcohol/cellulose nanocrystals/silver nanoparticles blend membranes.* Carbohyd Polym, 2013. **98**(2): p. 1573-1577.

51. Kamal, M.R. and V. Khoshkava, *Effect of cellulose nanocrystals (CNC) on rheological and mechanical properties and crystallization behavior of PLA/CNC nanocomposites.* Carbohydrate Polymers, 2015. **123**: p. 105-114.

52. Lin, N., et al., *Surface acetylation of cellulose nanocrystal and its reinforcing function in poly (lactic acid).* Carbohydrate Polymers, 2011. **83**(4): p. 1834-1842.

53. Bai, H., et al., *Preparation and characterization of poly (vinylidene fluoride) composite membranes blended with nano-crystalline cellulose.* Progress in Natural Science: Materials International, 2012. **22**(3): p. 250-257.

54. Chazeau, L., J. Cavaille, and J. Perez, *Plasticized PVC reinforced with cellulose whiskers. II. Plastic behavior.* J Polym Sci Pol Phys, 2000. **38**(3): p. 383-392.

55. Ljungberg, N., J.-Y. Cavaillé, and L. Heux, *Nanocomposites of isotactic polypropylene reinforced with rod-like cellulose whiskers.* Polymer, 2006. **47**(18): p. 6285-6292.

56. Yu, H.-Y., et al., *Simultaneous improvement of mechanical properties and thermal stability of bacterial polyester by cellulose nanocrystals.* Carbohyd Polym, 2012. **89**(3): p. 971-978.

57. Jiang, L., et al., *Study of the poly (3-hydroxybutyrate-co-3-hydroxyvalerate)/cellulose nanowhisker composites prepared by solution casting and melt processing.* J. Compos. Mater., 2008. **42**(24): p. 2629-2645.

58. Yu, H.-y., Z.-y. Qin, and Z. Zhe, *Cellulose nanocrystals as green fillers to improve crystallization and hydrophilic property of poly (3-hydroxybutyrate-co-3-hydroxyvalerate).* Progress in Natural Science: Materials International, 2011. **21**(6): p. 478-484.

59. Ma, L., et al., *Preparing cellulose nanocrystal/acrylonitrile-butadiene-styrene nanocomposites using the master-batch method.* Carbohyd Polym, 2015. **125**: p. 352-359.

60. Marcovich, N., et al., *Cellulose micro/nanocrystals reinforced polyurethane.* J. Mater. Res., 2006. **21**(4): p. 870-881.

61. Girouard, N., et al., *Exploiting colloidal interfaces to increase dispersion, performance, and pot-life in cellulose nanocrystal/waterborne epoxy composites.* Polymer, 2015. **68**: p. 111-121.

62. Xu, S., et al., *Mechanical and thermal properties of waterborne epoxy composites containing cellulose nanocrystals.* Polymer, 2013. **54**(24): p. 6589-6598.

63. Agustin, M.B., et al., *Starch-based biocomposite films reinforced with cellulose nanocrystals from garlic stalks.* Polym. Composite, 2013. **34**(8): p. 1325-1332.

64. Khan, A., et al., *Mechanical and barrier properties of nanocrystalline cellulose reinforced chitosan based nanocomposite films.* Carbohydrate Polymers, 2012. **90**(4): p. 1601-1608.

65. Moberg, T., et al., *Rheological properties of nanocellulose suspensions: effects of fibril/particle dimensions and surface characteristics.* Cellulose, 2017. **24**(6): p. 2499-2510.

66. Xu, X., et al., *Cellulose nanocrystals vs. cellulose nanofibrils: a comparative study on their microstructures and effects as polymer reinforcing agents.* ACS applied materials & interfaces, 2013. **5**(8): p. 2999-3009.

67. Lee, W.J., et al., *Strong and stiff: high-performance cellulose nanocrystal/poly (vinyl alcohol) composite fibers.* ACS applied materials & interfaces, 2016. **8**(46): p. 31500-31504.

68. Endo, R., T. Saito, and A. Isogai, *TEMPO-oxidized cellulose nanofibril/poly (vinyl alcohol) composite drawn fibers.* Polymer, 2013. **54**(2): p. 935-941.

69. Medeiros, E.S., et al., *Electrospun nanofibers of poly (vinyl alcohol) reinforced with cellulose nanofibrils.* Journal of Biobased Materials and Bioenergy, 2008. **2**(3): p. 231-242.

70. Jiang, E., et al., *Cellulose Nanofibers as Rheology Modifiers and Enhancers of Carbonization Efficiency in Polyacrylonitrile.* ACS Sustainable Chemistry & Engineering, 2017. **5**(4): p. 3296-3304.

71. Xu, X., et al., *Comparison between cellulose nanocrystal and cellulose nanofibril reinforced poly (ethylene oxide) nanofibers and their novel shish-kebab-like crystalline structures.* Macromolecules, 2014. **47**(10): p. 3409-3416.

72. Dai, L., et al., *Electrospun polyvinyl alcohol/waterborne polyurethane composite nanofibers involving cellulose nanofibers.* Journal of Applied Polymer Science, 2014. **131**(22).

73. Pujari, S.P., et al., *Covalent surface modification of oxide surfaces.* Angewandte Chemie International Edition, 2014. **53**(25): p. 6322-6356.

74. Georgakilas, V., et al., *Functionalization of graphene: covalent and non-covalent approaches, derivatives and applications.* Chemical reviews, 2012. **112**(11): p. 6156-6214.

75. Yu, H., et al., *Facile extraction of thermally stable cellulose nanocrystals with a high yield of 93% through hydrochloric acid hydrolysis under hydrothermal conditions.* Journal of Materials Chemistry A, 2013. **1**(12): p. 3938-3944.

76. Eyley, S. and W. Thielemans, *Surface modification of cellulose nanocrystals.* Nanoscale, 2014. **6**(14): p. 7764-7779.

77. Habibi, Y., H. Chanzy, and M.R. Vignon, *TEMPO-mediated surface oxidation of cellulose whiskers.* Cellulose, 2006. **13**(6): p. 679-687.

78. Isogai, A., T. Saito, and H. Fukuzumi, *TEMPO-oxidized cellulose nanofibers.* nanoscale, 2011. **3**(1): p. 71-85.

79. Kim, U.-J., et al., *Periodate oxidation of crystalline cellulose.* Biomacromolecules, 2000. **1**(3): p. 488-492.

80. Liimatainen, H., et al., *Sulfonated cellulose nanofibrils obtained from wood pulp through regioselective oxidative bisulfite pre-treatment.* Cellulose, 2013. **20**(2): p. 741-749.

81. Sirviö, J.A., et al., *Strong, self-standing oxygen barrier films from nanocelluloses modified with regioselective oxidative treatments.* ACS applied materials & interfaces, 2014. **6**(16): p. 14384-14390.

82. Saito, T., et al., *Homogeneous suspensions of individualized microfibrils from TEMPO-catalyzed oxidation of native cellulose.* Biomacromolecules, 2006. **7**(6): p. 1687-1691.

83. Chang, H., et al., *Structural and Functional Fibers.* Annual Review of Materials Research, 2017. **47**(1): p. 331-359.

84. Liu, Y., H.G. Chae, and S. Kumar, *Gel-spun carbon nanotubes/polyacrylonitrile composite fibers. Part I: Effect of carbon nanotubes on stabilization.* Carbon, 2011. **49**(13): p. 4466-4476.

85. Liu, Y., H.G. Chae, and S. Kumar, *Gel-spun carbon nanotubes/polyacrylonitrile composite fibers. Part II: Stabilization reaction kinetics and effect of gas environment.* Carbon, 2011. **49**(13): p. 4477-4486.

86. Ouyang, Q., et al., *Mechanism and kinetics of the stabilization reactions of itaconic acid-modified polyacrylonitrile.* Polymer Degradation and Stability, 2008. **93**(8): p. 1415-1421.

87. Liu, H.C., et al., *Stabilization kinetics of gel spun polyacrylonitrile/lignin blend fiber.* Carbon, 2016. **101**: p. 382-389.

88. Dalton, S., F. Heatley, and P.M. Budd, *Thermal stabilization of polyacrylonitrile fibres.* Polymer, 1999. **40**(20): p. 5531-5543.

89. Ko, T.H., H.Y. Ting, and C.H. Lin, *Thermal stabilization of polyacrylonitrile fibers.* Journal of applied polymer science, 1988. **35**(3): p. 631-640.

90. Houtz, R., *" Orlon" Acrylic Fiber: Chemistry and Properties.* Textile Research Journal, 1950. **20**(11): p. 786-801.

91. Grassie, N. and J. Hay, *Thermal coloration and insolubilization in polyacrylonitrile.* Journal of Polymer Science Part A: Polymer Chemistry, 1962. **56**(163): p. 189-202.

92. Standage, A. and R. Matkowsky, *Thermal oxidation of polyacrylonitrile.* European Polymer Journal, 1971. **7**(7): p. 775-783.

93. Henrici-Olive, G. and S. Olive, *Inter-versus intramolecular oligomerization of nitrile groups in polyacrylonitrile.* Polymer Bulletin, 1981. **5**(8): p. 457-461.

94. Chung, T.C., et al., *Optical studies of pyrolyzed polyacrylonitrile.* Journal of Polymer Science Part B: Polymer Physics, 1984. **22**(7): p. 1239-1246.

95. Dumanlı, A.G. and A.H. Windle, *Carbon fibres from cellulosic precursors: a review.* Journal of Materials Science, 2012. **47**(10): p. 4236-4250.

96. Tang, M.M. and R. Bacon, *Carbonization of cellulose fibers—I. Low temperature pyrolysis.* Carbon, 1964. **2**(3): p. 211-220.

97. Li, S., et al., *Real-time evolved gas analysis by FTIR method: an experimental study of cellulose pyrolysis.* Fuel, 2001. **80**(12): p. 1809-1817.

98. Morgan, P., *Carbon fibers and their composites*. Materials Engineering. 2005, Boca Raton: CRC press.

99. Bashir, Z., *A critical review of the stabilisation of polyacrylonitrile.* Carbon, 1991. **29**(8): p. 1081-1090.

100. Samir, M.A.S.A., et al., *Cellulose nanocrystals reinforced poly (oxyethylene).* Polymer, 2004. **45**(12): p. 4149-4157.

101. Aggour, Y. and M. Aziz, *Degradation of polyacrylonitrile by low energy ion beam and UV radiation.* Polym. Test., 2000. **19**(3): p. 261-267.

102. Karpushkin, E., et al., *Rheological properties of polyacrylonitrile solutions containing highly dispersed carbon nanotubes.* Polym Sci Ser A+, 2014. **56**(5): p. 681-686.

103. Chen, H., Y. Ding, and A. Lapkin, *Rheological behaviour of nanofluids containing tube/rod-like nanoparticles.* Powder Technol., 2009. **194**(1): p. 132-141.

104. Huang, S., et al., *Enhancement effect of filler network on isotactic polypropylene/carbon black composite melts.* Colloid Polym. Sci., 2011. **289**(15-16): p. 1673-1681.

105. Anderson, B.J. and C.F. Zukoski, *Rheology and microstructure of entangled polymer nanocomposite melts.* Macromolecules, 2009. **42**(21): p. 8370-8384.

106. Loginova, E.V., et al., *Quantification of copolymer composition (methyl acrylate and itaconic acid) in polyacrylonitrile carbon-fiber precursors by FTIR-spectroscopy.* Analytical Methods, 2016. **8**(2): p. 371-380.

107. Kumar, A., et al., *Characterization of cellulose nanocrystals produced by acid-hydrolysis from sugarcane bagasse as agro-waste.* Journal of Materials Physics and Chemistry, 2014. **2**(1): p. 1-8.

108. Schuster, P., *LCAO–MO studies on hydrogen bonding: The interaction between carbonyl and hydroxyl groups.* Int. J. Quantum Chem., 1969. **3**(6): p. 851-871.

109. Eichhorn, S.J., *Cellulose nanowhiskers: promising materials for advanced applications.* Soft Matter, 2011. **7**(2): p. 303-315.

110. Zafeiropoulos, N.E., *Interface engineering of natural fibre composites for maximum performance*. 2011: Woodhead Publishing. 428.

111. Swentek, I. and J. Wood. *Using the lap-shear test to measure polymer composite interfacial strength*. in *The 19th International Conference on Composite Materials, proceedings*. 2013.

112. Cho, D., S.B. Yoon, and T. Drzal, *Cellulose-based natural fiber topography and the interfacial shear strength of henequen/unsaturated polyester composites: influence of water and alkali treatments.* Composite Interfaces, 2009. **16**(7-9): p. 769-779.

113. Newcomb, B.A., et al., *Stress transfer in polyacrylonitrile/carbon nanotube composite fibers.* Polymer, 2014. **55**(11): p. 2734-2743.

114. Haspel, B., et al., *Characterization of the interfacial shear strength of glass-fiber reinforced polymers made from novel RTM processes.* International Journal of Plastics Technology, 2015. **19**(2): p. 333-346.

115. Thomason, J., et al., *Influence of fibre length and concentration on the properties of glass fibre-reinforced polypropylene: Part 3. Strength and strain at failure.* Compos Part A-Appl S, 1996. **27**(11): p. 1075-1084.

116. Kelly, A. and a.W. Tyson, *Tensile properties of fibre-reinforced metals: copper/tungsten and copper/molybdenum.* J. Mech. Phys. Solids, 1965. **13**(6): p. 329-350.

117. Dumanli, A.G. and T. Savin, *Recent advances in the biomimicry of structural colours.* Chemical Society Reviews, 2016. **45**(24): p. 6698-6724.

118. Lee, K.-Y., et al., *On the use of nanocellulose as reinforcement in polymer matrix composites.* Compos. Sci. Technol., 2014. **105**: p. 15-27.

119. Cox, H., *The elasticity and strength of paper and other fibrous materials.* Brit J Appl Phys, 1952. **3**(3): p. 72-79.

120. Krenchel, H., *Fibre reinforcement; theoretical and practical investigations of the elasticity and strength of fibre-reinforced materials*. 1964, Technical University of Denmark: Copenhagen.

121. Visakh, P., et al., *Crosslinked natural rubber nanocomposites reinforced with cellulose whiskers isolated from bamboo waste: processing and mechanical/thermal properties.* Compos Part A-Appl S, 2012. **43**(4): p. 735-741.

122. Maqsood, H.S., et al., *Reinforcement of enzyme hydrolyzed longer jute micro crystals in polylactic acid.* Polym. Composite, 2016. **39**(4): p. 1089-1097.

123. Battegazzore, D., S. Bocchini, and A. Frache, *Thermomechanical improvement of glycerol plasticized maize starch with high loading of cellulose, flax and talc fillers.* Polym. Int., 2016. **65**(8): p. 955-962.

124. Ozkul, M., J. Mark, and J. Aubert, *The elastic and plastic mechanical responses of microcellular foams.* J. Appl. Polym. Sci., 1993. **48**(5): p. 767-774.

125. Lai, C., et al., *Investigation of post-spinning stretching process on morphological, structural, and mechanical properties of electrospun polyacrylonitrile copolymer nanofibers.* Polymer, 2011. **52**(2): p. 519-528.

126. Chen, S., et al., *Effects of crystal orientation on cellulose nanocrystals–cellulose acetate nanocomposite fibers prepared by dry spinning.* Biomacromolecules, 2014. **15**(10): p. 3827-3835.

127. Allen, S., et al., *The barrier properties of polyacrylonitrile.* Journal of Membrane Science, 1977. **2**: p. 153-163.

128. Strupinsky, G. and A.L. Brody. *A twenty-year retrospective on plastics: oxygen barrier packaging materials*. in *Polymers, Laminations & Coatings Conference Proceedings*. 1998.

129. Liu, Y. and S. Kumar, *Recent progress in fabrication, structure, and properties of carbon fibers.* Polymer Reviews, 2012. **52**(3): p. 234-258.

130. Lv, M.-y., H.-y. Ge, and J. Chen, *Study on the chemical structure and skin-core structure of polyacrylonitrile-based fibers during stabilization.* Journal of polymer research, 2009. **16**(5): p. 513-517.

131. Belbekhouche, S., et al., *Water sorption behavior and gas barrier properties of cellulose whiskers and microfibrils films.* Carbohydrate Polymers, 2011. **83**(4): p. 1740-1748.

132. Li, F., et al., *Multi-functional coating of cellulose nanocrystals for flexible packaging applications.* Cellulose, 2013. **20**(5): p. 2491-2504.

133. Arseneau, D.F., *Competitive reactions in the thermal decomposition of cellulose.* Canadian Journal of Chemistry, 1971. **49**(4): p. 632-638.

134. Peng, Y., et al., *Influence of drying method on the material properties of nanocellulose I: thermostability and crystallinity.* Cellulose, 2013. **20**(5): p. 2379-2392.

135. Quiévy, N., et al., *Influence of homogenization and drying on the thermal stability of microfibrillated cellulose.* Polymer Degradation and Stability, 2010. **95**(3): p. 306-314.

136. Mathur, R., O. Bahl, and J. Mittal, *A new approach to thermal stabilisation of PAN fibres.* Carbon, 1992. **30**(4): p. 657-663.

137. Klemm, D., et al., *Comprehensive Cellulose Chemistry Volume 1: Fundamentals and Analytical Methods*. Comprehensive Cellulose Chemistry Vol. 1. 1998, Weinheim: Wiley-VCH

138. Fan, M., D. Dai, and B. Huang, *Fourier transform infrared spectroscopy for natural fibres*, in *Fourier transform*, S. Salih, Editor. 2012, IntechOpen.

139. French, A.D., *Idealized powder diffraction patterns for cellulose polymorphs.* Cellulose, 2014. **21**(2): p. 885-896.

140. Gupta, A. and R. Singhal, *Effect of copolymerization and heat treatment on the structure and x-ray diffraction of polyacrylonitrile.* J Polym Sci Pol Phys, 1983. **21**(11): p. 2243-2262.

141. Kissinger, H.E., *Reaction kinetics in differential thermal analysis.* Analytical chemistry, 1957. **29**(11): p. 1702-1706.

142. Nair, C.R., K. Krishnan, and K. Ninan, *Differential scanning calorimetric study on the Claisen rearrangement and thermal polymerisation of diallyl ether of bisphenols.* Thermochimica acta, 2000. **359**(1): p. 61-67.

143. Newcomb, B.A., *Processing, structure, and properties of carbon fibers.* Composites Part A: Applied Science and Manufacturing, 2016. **91**: p. 262-282.

144. Yang, H., et al., *Characteristics of hemicellulose, cellulose and lignin pyrolysis.* Fuel, 2007. **86**(12): p. 1781-1788.

145. Park, S., et al., *Cellulose crystallinity index: measurement techniques and their impact on interpreting cellulase performance.* Biotechnology for biofuels, 2010. **3**(10).

146. Segal, L., et al., *An empirical method for estimating the degree of crystallinity of native cellulose using the X-ray diffractometer.* Textile Research Journal, 1959. **29**(10): p. 786-794.

147. Zhang, K., et al., *Synthesis and characterisation of cellulose sulfates regarding the degrees of substitution, degrees of polymerisation and morphology.* Carbohydrate polymers, 2011. **83**(4): p. 1659-1664.

148. Svensson, A., et al., *Bacterial cellulose as a potential scaffold for tissue engineering of cartilage.* Biomaterials, 2005. **26**(4): p. 419-431.

149. Schweiger, R.G., *Polysaccharide sulfates. I. Cellulose sulfate with a high degree of substitution.* Carbohydrate Research, 1972. **21**(2): p. 219-228.

150. Nourani, M., et al., *Production of a biodegradable flocculant from cotton and evaluation of its performance in coagulation-flocculation of kaolin clay suspension: Optimization through response surface methodology (RSM).* Journal of Environmental Chemical Engineering, 2016. **4**(2): p. 1996-2003.

151. Fujisawa, S., et al., *Preparation and characterization of TEMPO-oxidized cellulose nanofibril films with free carboxyl groups.* Carbohydrate Polymers, 2011. **84**(1): p. 579-583.

152. Gu, J., et al., *Quantification of cellulose nanowhiskers sulfate esterification levels.* Carbohydrate polymers, 2013. **92**(2): p. 1809-1816.

153. Lin, N. and A. Dufresne, *Surface chemistry, morphological analysis and properties of cellulose nanocrystals with gradiented sulfation degrees.* Nanoscale, 2014. **6**(10): p. 5384-5393.

154. Wang, Z.-M., et al., *Homogeneous sulfation of bagasse cellulose in an ionic liquid and anticoagulation activity.* Bioresource Technology, 2009. **100**(4): p. 1687-1690.

155. Hunter, R.J., *Zeta potential in colloid science: principles and applications*. Vol. 2. 1988, San Diego: Academic press.

156. Okita, Y., et al., *TEMPO-oxidized cellulose nanofibrils dispersed in organic solvents.* Biomacromolecules, 2010. **12**(2): p. 518-522.

157. Tonoli, G., et al., *Cellulose micro/nanofibres from Eucalyptus kraft pulp: preparation and properties.* Carbohydrate polymers, 2012. **89**(1): p. 80-88.

158. Reischl, M., K. Stana-Kleinschek, and V. Ribitsch. *Electrokinetic investigations of oriented cellulose polymers*. in *Macromolecular Symposia*. 2006. Wiley Online Library.

159. Hantgan, R.R. and J. Hermans, *Assembly of fibrin. A light scattering study.* Journal of Biological Chemistry, 1979. **254**(22): p. 11272-11281.

160. Carr Jr, M.E. and J. Hermans, *Size and density of fibrin fibers from turbidity.* Macromolecules, 1978. **11**(1): p. 46-50.

161. Sirviö, J.A., et al., *Sustainable packaging materials based on wood cellulose.* RSC Advances, 2013. **3**(37): p. 16590-16596.

162. Lewis, L., et al., *Hydrothermal Gelation of Aqueous Cellulose Nanocrystal Suspensions.* Biomacromolecules, 2016. **17**(8): p. 2747-2754.

163. Beck, S. and J. Bouchard, *Auto-catalyzed acidic desulfation of cellulose nanocrystals.* Nordic Pulp & Paper Research Journal, 2014. **29**(1): p. 6-14.

164. Dong, X.M. and D.G. Gray, *Effect of counterions on ordered phase formation in suspensions of charged rodlike cellulose crystallites.* Langmuir, 1997. **13**(8): p. 2404-2409.

165. Juillard, J., *Dimethylformamide: purification, tests for purity and physical properties.* Pure and Applied Chemistry, 1977. **49**(16): p. 885-892.

166. Heinze, T. and T. Liebert, *Unconventional methods in cellulose functionalization.* Progress in polymer science, 2001. **26**(9): p. 1689-1762.

167. Klemm, D., et al., *Comprehensive Cellulose Chemistry Volume 2: Funtionalization of Cellulose*. Comprehensive Cellulose Chemistry. Vol. 2. 1998, Weinheim: Wiley-VCH. 164-197.

168. Shimizu, M., et al., *Preparation and characterization of TEMPO-oxidized cellulose nanofibrils with ammonium carboxylate groups.* International journal of biological macromolecules, 2013. **59**: p. 99-104.

169. Jin, L., et al., *Amino-functionalized nanocrystalline cellulose as an adsorbent for anionic dyes.* Cellulose, 2015. **22**(4): p. 2443-2456.

170. Chang, H., et al., *Ductile polyacrylonitrile fibers with high cellulose nanocrystals loading.* Polymer, 2017. **122**: p. 332-339.

171. Josefsson, G., F. Berthold, and E.K. Gamstedt, *Stiffness contribution of cellulose nanofibrils to composite materials.* International Journal of Solids and Structures, 2014. **51**(5): p. 945-953.

172. Northolt, M. and J. Van Aartsen. *Chain orientation distribution and elastic properties of poly (p-phenylene terephthalamide), a "rigid rod" polymer*. in *Journal of Polymer Science: Polymer Symposia*. 1977. Wiley Online Library.

173. Chipera, S.J. and D.L. Bish, *Fitting full X-ray diffraction patterns for quantitative analysis: a method for readily quantifying crystalline and disordered phases.* Advances in Materials Physics and Chemistry, 2013. **3**(1A): p. 47-53.

174. Batchelder, M. and G. Cressey, *Rapid, accurate phase quantification of clay-bearing samples using a position-sensitive X-ray detector.* Clay Clay Miner, 1998. **46**(2): p. 183-194.

175. Hinrichsen, G., *Structural changes of drawn polyacrylonitrile during annealing.* J. Polym. Sci., Part C: Polym. Symp., 1972. **38**(1): p. 303-314.

176. Moskalenko, V., et al., *Effect of a filler on the crystallization of polysiloxane elastomers.* Polymer Science U.S.S.R., 1971. **13**(12): p. 3017-3024.

177. Kuo, M., J. Huang, and M. Chen, *Non-isothermal crystallization kinetic behavior of alumina nanoparticle filled poly (ether ether ketone).* Mater. Chem. Phys., 2006. **99**(2): p. 258-268.

178. Rufino, E. and E. Monteiro, *Infrared study on methyl methacrylate–methacrylic acid copolymers and their sodium salts.* Polymer, 2003. **44**(23): p. 7189-7198.

179. Liang, C. and S. Krimm, *Infrared spectra of high polymers. VII. Polyacrylonitrile.* Journal of Polymer Science, 1958. **31**(123): p. 513-522.

180. Farsani, R.E., et al., *FT-IR study of stabilized PAN fibers for fabrication of carbon fibers.* International Journal of Mechanical, Aerospace, Industrial, Mechatronic and Manufacturing Engineering, 2009. **3**(2): p. 161-164.

181. Lee, S., et al., *Structural evolution of polyacrylonitrile fibers in stabilization and carbonization.* Advances in chemical engineering and science, 2012. **2**(2): p. 275.